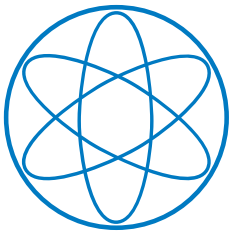

Physik-Department

Reducing Attenuation and Motion Artefacts in Hybrid PET/MR Imaging

Dissertation
von
Sebastian Fürst

Technische Universität München

Fakultät für Physik der Technischen Universität München
IMETUM Zentralinstitut für Medizintechnik

Klinikum rechts der Isar der Technischen Universität München
Nuklearmedizinische Klinik und Poliklinik

Reducing Attenuation and Motion Artefacts in Hybrid PET/MR Imaging

Sebastian Fürst

Vollständiger Abdruck der von der Fakultät für Physik der Technischen Universität München zur Erlangung des akademischen Grades eines

Doktors der Naturwissenschaften (Dr. rer. nat.)

genehmigten Dissertation.

Vorsitzende(r): Univ.-Prof. Dr. J. L. van Hemmen
Prüfer der Dissertation:

1. Univ.-Prof. Dr. A. Haase
2. Univ.-Prof. Dr. F. Pfeiffer
3. apl. Prof. Dr. S. Ziegler

Die Dissertation wurde am 05.02.2015 bei der Technischen Universität München eingereicht und durch die Fakultät für Physik am 13.07.2015 angenommen.

Im Gedenken an Heinrich Lendermann

Abstract

The huge success and fast clinical adoption of PET/CT since its introduction in the early 2000s are proof of the strong interest in multimodal imaging in nuclear medicine. The integration of PET and MR potentially provides additional advantages, including higher soft-tissue contrast of MR images, lower radiation dose for the patient and shorter examination times, if both a PET and an MR scan are required. The integration, however, is not straightforward. Conventional photodetectors cannot be operated in the high static magnetic field of the MR, whereas the rapid switching of gradient fields and RF signals interfere with PET front-end electronics and vice versa.

The physical performance of the novel Biograph mMR integrated PET/MR system, based on APD PET technology and a 3-T magnet, was therefore evaluated according to the NEMA protocol for the PET component, whereas the MR subsystem was investigated following the steps outlined in the ACR quality control manual. With regard to quantitative accuracy and specifically attenuation correction, integrated PET/MR poses new challenges. Attenuation maps are generated on the Biograph mMR by threshold-based segmentation of MR images into four tissue classes. This method was tested for reproducibility and adverse effects of MR contrast agents on attenuation maps and thus cardiac PET quantification. Moreover, for proper MR imaging dedicated coils are employed to receive MR signals. Although they mean more attenuating material in the field of view of the PET detectors, flexible surface coils are not accounted for during attenuation correction in the current implementation of the Biograph mMR. Their impact was studied in a phantom as well as with clinical data. Other factors reducing quantitative accuracy of PET include respiratory motion of the patient. Integrated PET/MR allows for the first time the combination of various PET- and MR-based correction techniques. Several methods for the generation of respiratory signals using an external sensor or PET or MR data were assessed, including a proposed variation of methods for increased reliability, as well motion-corrected PET reconstruction employing motion vector fields derived from MR images or PET data.

With a spatial resolution of 4.3 mm near the centre of the FOV, the Biograph mMR is comparable to state-of-the-art PET/CT systems. The higher sensitivity of 15.0 $\frac{\text{kcps}}{\text{MBq}}$ is a consequence of the longer axial field of view and the smaller detector ring diameter. The administration of contrast agents led to an apparent increase of the amount of soft tissue in attenuation maps of (17 $\pm$ 8)%, whereas the amount of fat decreased by (-39 $\pm$ 15)%. Apparent changes of standardised uptake values in the left ventricle ranged between

−2% and +27%. The patient table of the Biograph mMR led to a decrease of the true count rate of 19%, whereas the same count rate was (+6 ± 1)% higher in patient scans without surface coils. The resulting effect on the apparent standardised uptake value exceeded 10% in more than half of the evaluated tumour lesions. For gating, mean tracer uptake in lesions was found to be (17 ± 19)% higher, (13 ± 19)% for MR-based motion correction and (18 ± 15)% for PET-based motion correction, if the best PET-based respiratory signal was used. Its correlation with signal derived from MR data was 0.80 ± 0.13.

Kurzfassung

Der große Erfolg und die schnelle klinische Annahme von PET/CT seit der Einführung in den frühen 2000er Jahren sind Beweis für das starke Interesse an multimodaler Bildgebung in der Nuklearmedizin. Die Integration von PET und MR liefert möglicherweise zusätzliche Vorteile, darunter den höheren Weichgewebekontrast der MR-Bilder, die niedrigere Strahlendosis für den Patienten und kürzere Untersuchungszeiten, wenn sowohl ein PET- als auch ein MR-Scan indiziert sind. Die Integration ist jedoch nicht einfach. Konventionelle Photodetektoren können im hohen statischen Magnetfeld des MR nicht betrieben werden, während das schnelle Schalten von Gradientenfeldern und die RF-Signale mit der PET-Eingangselektronik interferieren und umgekehrt.

Die physikalische Leistungsfähigkeit des neuartigen Biograph mMR integrierten PET/MR-Systems, das auf APD-PET-Technologie und einem 3-T-Magneten basiert, wurde daher gemäß des NEMA-Protokolls für die PET-Komponente evaluiert, während das MR-Teilsystem den im ACR Quality Control Manual beschriebenen Schritten folgend untersucht wurde. In Bezug auf quantitative Genauigkeit und speziell Schwächungskorrektur stellt die integrierte PET/MR neue Herausforderungen dar. Schwächungskarten werden auf dem Biograph mMR durch schwellenwertbasierte Segmentierung von MR-Bildern in vier Gewebeklassen erzeugt. Diese Methode wurde auf Reproduzierbarkeit und nachteilige Effekte von MR-Kontrastmitteln auf Schwächungskarten und damit kardiale PET-Quantifizierung getestet. Darüberhinaus werden für korrekte MR-Bildgebung dezidierte Spulen zum Empfang der MR-Signale verwendet. Obwohl sie zusätzliches schwächendes Material im Gesichtsfeld der PET-Detektoren bedeuten, werden flexible Oberflächenspulen in der aktuellen Implementierung des Biograph mMR nicht während der Schwächungskorrektur berücksichtigt. Die Auswirkungen wurden in einem Phantom und mit klinischen Daten studiert. Andere Faktoren, die die quantitative Genauigkeit von PET beeinträchtigen, umfassen die Atembewegung des Patienten. Die integrierte PET/MR erlaubt zum ersten Mal die Kombination verschiedener PET- und MR-basierter Korrekturtechniken. Mehrere Methoden zur Erzeugung von Atemsignalen unter Benutzung externer Sensoren oder PET- oder MR-Daten wurden beurteilt, darunter eine vorgeschlagene Variation von Methoden für erhöhte Zuverlässigkeit, sowie bewegungskorrigierte PET-Rekonstruktion mit aus MR-Bildern oder PET-Daten gewonnenen Bewegungsfeldern.

Mit einer Ortsauflösung von 4.3 mm in der Nähe des Gesichtsfeldzentrums ist der Biograph mMR vergleichbar mit dem Stand der Technik von PET/CT-

Systemen. Die höhere Sensitivät von 15.0 $\frac{\text{kcps}}{\text{MBq}}$ ist eine Folge des längeren axialen Gesichtsfeldes und des kleineren Detektorringdurchmessers. Die Verabreichung von Kontrastmitteln führte zu einem in den Schwächungskarten sichtbaren Anstiegs der Menge des Weichgewebes von (17 ± 8)%, während die Menge von Fett um (-39 ± 15)% abnahm. Die scheinbaren Änderungen der standardisierten Aufnahmewerte im linken Ventrikel bewegten sich zwischen −2% und +27%. Der Patiententisch des Biograph mMR führte zu einer Verringerung der wahren Zählrate von 19%, während dieselbe Zählrate in Patientenuntersuchungen ohne Oberflächenspule (+6 ± 1)% höher war. Der resultierende Effekt auf die in den Bildern sichtbaren standardisierten Aufnahmewerte übertraf 10% in mehr als der Hälfte der evaluierten Tumorläsionen. Für Gating war die mittlere Tracer-Aufnahme in Läsionen (17 ± 19)% höher, (13 ± 19)% für MR-basierte und (18 ± 15)% für PET-basierte Bewegungskorrektur, falls das beste PET-basierte Atemsignal verwendet wurde. Seine Korrelation mit dem aus den MR-Daten abgeleiteten Signal betrug 0.80 ± 0.13.

Contents

Part I.

Introduction

1. Motivation

Nowadays, a broad range of medical imaging techniques is readily available in hospitals and research institutes worldwide. They all build upon physical principles and phenomena, such as optics, acoustics or ionising radiation, to diagnose, characterise and follow the course of diseases or study the human body.

Tomographic techniques such as computed tomography (CT), magnetic resonance imaging (MRI) and positron emission tomography (PET) play an important role in clinical diagnostics. They offer the possibility of non-invasively generating three-dimensional (3d) images of organs and other inner structures of the human body by taking advantage of the interaction of ionising radiation with biological materials. Both CT and MRI yield anatomical information by measuring the absorption of x-rays along transmission lines passing through the body in the case of CT and employing magnetic fields and radiofrequency (RF) signals to assess the density of magnetic moments of protons in the patient (MRI). In contrast to that, PET generates functional 3d images. This is achieved by visualising the spatial distribution of a positron-emitting radionuclide that is administered to the patient. Whereas the imaging principles of PET and CT are similar as they rely on ionising radiation, MRI is therefore based on a fundamentally different physical imaging concept.

Multimodal images have a high potential for improved tissue characterisation by offering the possibility of localising functional information in the anatomical background of the patient. This potential led to extensive research efforts in the field of software co-registration in the 1990s and the successful introduction of combined PET/CT scanners (Figure 1.1) to the clinical routine in the early 2000s [6]. Replacing CT with MRI in this context might have further advantages due to the higher soft-tissue contrast of MRI and the lower radiation dose absorbed by the patient, possibly beyond anatomical correlation, if functional MRI data acquisition is performed simultaneously.

Challenges of PET/MR

PET can detect single pairs of annihilation photons, thereby measuring the amount of radioactivity within the field of view (FOV). The accuracy of this measurement depends on the properties of the PET detectors. Another requirement, however, is specific knowledge of the composition of the objects within the FOV of the detectors to be able to correct for the attenuation and scattering of gamma rays as they pass through them. Quantification of PET

Figure 1.1.: The Siemens Biograph mCT PET/CT system.

images is in any examination furthermore affected by factors such as physiological motion of the patient. The combination and especially the integration of PET and MRI poses new challenges in terms of hardware and attenuation correction (AC) that were not encountered in the development of PET/CT, but offers additional approaches to correct for motion.

The integration of PET and MRI is not straightforward, as will be discussed in chapter 3. The high static magnetic fields, the quickly switching gradient fields as well as the RF signals of an MRI render conventional PET detectors unoperational and interfere with PET front-end electronics and vice versa. PET detectors in the FOV of an MRI, on the other hand, introduce inhomogeneities in the magnetic field. To overcome these challenges, shielding of critical components, novel detector concepts and modified system architectures are necessary.

In addition to hardware, the integration of PET and MRI calls for novel procedures in the context of PET AC. As outlined in chapter 4, gamma-ray attenuation properties of tissue cannot be directly derived from the MR signal. Due to the lack of a CT component, an approach based on the segmentation of MR images was established with the first clinical PET/MR system for the generation of attenuation maps (μ-maps) [61]. Since the segmentation thresholds are fixed, problems might arise in conjunction with MR contrast agents (CA), for which the thresholds are not optimised. In contrast to CT, where the administered CA affect gamma-ray attenuation, gadolinium-based (Gd) CA enhance the MR signal by shortening T1 and T2 relaxation times of protons in water. This could then lead to a shift of μ-map composition, subsequently resulting in a distorted activity distribution in attenuation-corrected images.

Another consequence of the integration of PET and MRI that affects AC is the presence of MRI hardware in the FOV of the PET detectors. For optimal

Figure 1.2.: The Siemens Biograph mMR PET/MR system.

signal-to-noise ratio (SNR), dedicated RF coils, which transmit and receive the MR signal, have to be placed as close as possible to the body region of interest. As pointed out in chapter 5, not every type of coil can be easily included in the process of AC, because the information of the attenuating properties of its components might not be precise or because knowledge of its position might not be exact.

With scan durations of several minutes per bed position, physiological motion of the patient constitutes a major source of degradation of image quality in PET. Respiratory and other types of motion lead to image blurring and hence less accurate image quantification [66]. Although patient motion concerns all imaging modalities, its compensation and correction is particularly challenging in PET due to the relatively low count rate statistics, as argued in chapter 6.

State of the Art

Previous work on combined PET/MR hardware includes two separate scanners, which share the same patient bed [79], a set-up in which the PET scintillators are located inside the magnet of the MRI and the emitted light is guided outside the fringe field [12, 33, 75, 88], a custom magnet architecture [88] and field-cycled MR image acquisition combined with modified PET front-ends and photodetectors that are insensitive to magnetic fields, allowing for PET data to be acquired in specific intervals [33]. Moreover, preclinical PET/MR scanners based on avalanche photodiodes (APD) [85] and PET inserts utilising the same type of detector were developed [12]. The Philips Ingenuity

TF and the Siemens Biograph mMR (Figure 1.2) are the two commercially available clinical solutions. In the case of the former, the patient is moved consecutively into two separate PET and MR scanners, while resting on the same table [108]. The PET detectors of the latter are integrated into the MR subsystem and located between the gradient and the body coils as detailed in 3.2.1. This is the only approach that allows simultaneous isocentric acquisition of PET and MR data, however at the cost of higher efforts to limit mutual interference.

In terms of segmentation-based AC, studies primarily aimed at other problems than CA, for example, the effect of the number of tissue classes on PET quantification, variability of attenuation coefficients and general tissue misclassification [44, 58]. One publication deals with CA in the context of PET/MR, but focusses on experiments to quantify the extent of the additional attenuation of the PET signal caused by CA and the corresponding attenuation coefficients of MR CA [55]. An extensive study involving real data from a number of patients had not been conducted.

The impact of MR equipment and other additional hardware in the FOV of PET detectors was assessed on PET-only systems [20, 56, 92], PET/CTs [20, 56] and non-simultaneous PET/MR scanners [92, 109]. Only one group worked with the Biograph mMR and additionally provided suggestions for correction for MR surface coils [70]. Since the mentioned groups studied this issue primarily in phantoms, neither general conclusions towards clinical relevance were formulated, nor the implications for patient-scan duration examined.

Several methods to compensate for motion were proposed, encompassing gating [66], the correction of reconstructed images [8, 28, 74] and motion-incorporating reconstruction algorithms [51, 78]. The respiratory signal required for gating of PET or other data can be obtained with external sensors and fiducial markers [54,66,99] or derived from PET data itself [10,36,94]. In MRI, navigator echoes are used to follow the movement of anatomical structures, for example, the liver dome, to determine the respiratory state [26]. Within the field of MRI, tremendous efforts are directed at the research of and development of motion modelling techniques [63], whereas other groups work on the extraction of motion information directly from PET raw data [19]. The integration of PET/MR is promising in this regard, because it allows the combination of various of the aforementioned methods to specific motion correction strategies. However, a direct comparison of MR- and PET-based motion correction methods was not yet made. Instead of real patient data, conclusions were mostly drawn from animal studies [16] and simulated or phantom data [21,22,35,71,76,77]. PET-driven motion correction was tested on data of 14 patients [19] and MR-based motion correction on data of five patients at maximum [72,105].

Goals

The goals of this work on attenuation and motion correction in integrated PET/MR were fourfold. Firstly, the performance of the Biograph mMR integrated PET/MR scanner was evaluated according to the NU 2-2007 protocol of the National Electrical Manufacturers Association (NEMA) [65] for the PET and the quality control manual of the American College of Radiology (ACR) [1] for the MR subsystem (chapter 3), thereby taking into account the possibility of mutual interference. Secondly, reproducibility of μ-maps acquired on the Biograph mMR was assessed as well as the consequences of MRI CA for μ-map generation and PET quantification in patients undergoing cardiothoracic imaging (chapter 4). Thirdly, a phantom study was performed to measure the effect of flexible MRI surface coils and the patient table of the Biograph mMR on PET quantification and count statistics, image quality and scan time. A subsequent patient study was focussed on the clinical relevance of the effect (chapter 5). This work is concluded with the implementation and investigation of different motion-correction strategies, including the proposition of a variation of methods for the extraction of respiratory signals from PET data and a rigorous comparative study of MR- and PET-driven motion-corrected PET image reconstruction (chapter 6).

2. PET and MR Basics

2.1. Positron Emission Tomography

2.1.1. Positron Decay

The imaging principle of PET makes use of unstable isotopes that decay by positron emission. This mode of decay denotes the conversion of a proton p into a neutron n, while ejecting a positron β^+ and a neutrino ν:

$$ {}^{1}_{1}p \rightarrow {}^{1}_{0}\, n + {}^{0}_{1}\, \beta^+ + \nu \tag{2.1} $$

An example of a PET radiotracer is the widely used ^{18}F-fluorodeoxyglucose (^{18}F-FDG), a glucose analogue in which one normal hydroxyl group is substituted by the positron-emitting isotope ^{18}F [30,93]. The decay equation of ^{18}F is given by:

$$ {}^{18}_{9}F \rightarrow {}^{18}_{8}\, O + {}^{0}_{1}\, \beta^+ + \nu_e \tag{2.2} $$

The energy spectrum of emitted positrons is continuous up to a maximum energy, which depends on the isotope. Charge neutrality of the otherwise positively charged atom is maintained through a process called internal conversion. The nucleus transfers a sufficient amount of energy to an orbital electron, which then leaves the atom. The transferred energy exceeds the binding energy of the electron by the required kinetic energy.

The emitted β^+ particle loses kinetic energy on its path through surrounding matter. This occurs primarily in inelastic collisions with atomic electrons, leading to the ionisation of the respective atom. Inelastic scattering events with the nucleus are also possible, causing the emission of Bremsstrahlung. Other types of interaction of positrons with matter, in which no energy is lost, are elastic scattering with atomic electrons and elastic scattering with nuclei. In all of these four forms of interaction, the positron is deflected from its path.

When the positron lost almost all of its kinetic energy, it can combine with an electron that is similarly close to rest. Both particles then annihilate by emitting electromagnetic radiation. In the most probable case, it is two photons or gamma rays, which travel at 180° in opposing directions to satisfy the law of conservation of momentum. The energy of each of the photons is 511 keV, which is equivalent to the masses of electron and positron at rest.

In water or human tissue, this direct annihilation accounts for approximately 67% of all annihilation events [4]. In the other cases, electrons

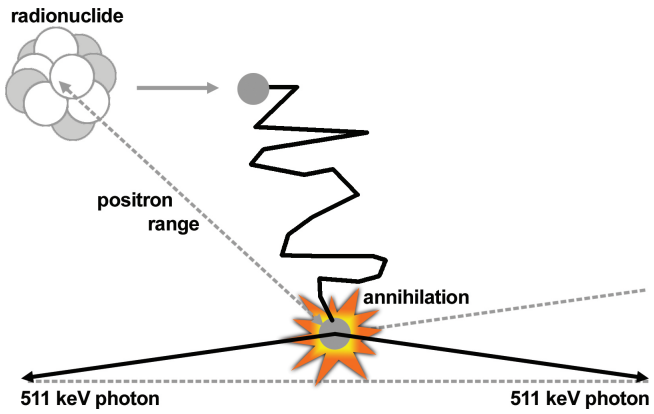

Figure 2.1.: The emitted positron loses energy in inelastic collisions until it combines with an electron. The positron range and non-collinearity of the paths of the two resulting annihilation photons due to residual positron-electron momentum reduce spatial resolution (According to [15], from [29])

and positrons form a metastable bound system before combination, called positronium, in which the positron acts as the nucleus for a mean lifetime of 10^{-10} s [15].

In PET images, it is desirable to determine the position of the nucleus at the time of decay and not to localise the annihilation event (Figure 2.1). In the case of ^{18}F, the positron range between the time point of emission and that of annihilation is in water on average 0.6 mm [4]. Additionally, there is in water a probability of 65% that the momentum of electron and proton does not equal zero [4], resulting in a deviation from 180° of the angle between the flight paths of the two particles, which is known as non-collinearity. Positron range and non-collinearity limit the theoretically achievable spatial resolution in PET.

2.1.2. Interaction of Radiation with Matter

There are two general forms of radiation, particulate and electromagnetic or photon radiation. Particles such as positrons, which were dealt with in detail in 2.1.1, fall into the first category. In PET, the two most relevant types of interaction between electromagnetic radiation and matter are the photoelectric effect and Compton scattering.

The photoelectric effect describes the interaction of photons with orbital electrons, primarily from inner atomic shells (Figure 2.2). The photon is absorbed, thereby transferring all of its energy to an electron, called the photoelectron, which is then released from the atom. The transferred photon energy is the sum of the binding energy of this electron and its kinetic energy outside of the atom. The vacancy left by the photoelectron is filled with an orbital electron from an outer shell, whereas the difference in binding energies

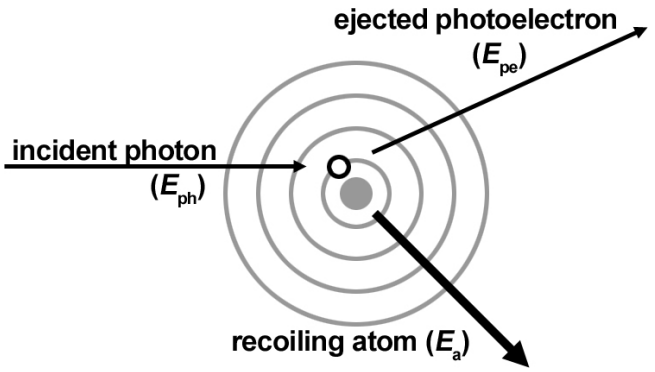

Figure 2.2.: The absorption of photons with subsequent ejection of orbital electrons is known as the photoelectric effect (According to [103], from [29]).

between the two energy levels is emitted as characteristic x rays. It is also possible that this excessive energy is transferred to another orbital electron, which is emitted without additional electromagnetic radiation. This electron is called Auger electron. In human tissue, the photoelectric effect is most important for photon energies below 100 keV and therefore does not have high relevance for 511-keV annihilation photons [4].

Compton scattering dominates the interactions of matter and photons with energies between approximately 100 keV and 2 MeV [4]. It denotes the interaction of a photon with a loosely-bound outer-shell electron, which can be regarded as free. In such a scattering event, the incident photon is deflected from its path and transfers a fraction of its energy to the recoil electron, upon which the electron is ejected from the atom. The energy loss of the photon equals the sum of the low binding energy and the kinetic energy of the electron and can be calculated using the Compton equation [103]

$$E_\mathrm{f} = \frac{E_0}{1 + \frac{E_0}{m_\mathrm{e}c^2}(1 - \cos\theta)} \tag{2.3}$$

where E_0 is the photon energy before and E_f its energy after the scattering event, $m_\mathrm{e}c^2 = 511$ keV the electron energy at rest and θ the scattering angle. It can be deduced that the highest possible energy loss in a Compton scattering event with $E_0 = 511$ keV is 170 keV and occurs in the case of backscattering for $\theta = 180°$. In PET with human tissue, the probability for a scattered photon to undergo another scattering event is less than 20% [4].

2.1.3. Block Detector Principle

The detection of annihilation photons in PET imaging today is primarily performed according to the block detector principle. A block detector is a

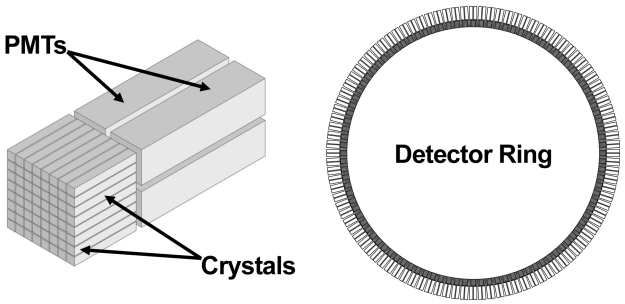

Figure 2.3.: The block detector consists of scintillation crystals that are read-out by photodetectors (left) [29]. Several of these block detectors are arranged in a PET detector ring (right).

member of the group of scintillation detectors and consists of an array of small scintillation crystals, which are read out by a matrix of photodetectors (Figure 2.3). The coupling between the two is achieved through dedicated light guides. The scintillation crystals absorb the incident annihilation photons and emit a fraction of the absorbed energy as photons in the visible range. The photodetectors then convert the scintillation photons into an amplified electrical signal. A PET scanner contains several detector rings, which are formed by a sufficient number of these block detectors.

The specific block detector design depends on the manufacturer. An assembly of 13×13 scintillation crystals with a size of $4 \times 4 \times 20$ mm^3 in combination with four PMTs is common, as well as 6×9 crystals of $4.2 \times 6.3 \times 25$ mm^3 or panels with 23×44 crystals measuring $4 \times 4 \times 22$ mm^3 each [42, 45, 91]. As an alternative to PMTs and after years of pre-clinical research, APDs are introduced to PET systems for human examinations, which is at the centre of this work.

The block detector principle yields a lower number of read-out channels and a lower price point than one-to-one coupling of crystals and detectors, but a higher spatial resolution than Anger cameras, in which one large crystal is attached to an array of photodetectors.

Scintillators

In inorganic scintillators, the only scintillation materials relevant for PET, atoms are organised in a crystal lattice. As the outer electrons can be considered as quasi free, the problem to be solved becomes a one-electron problem in the periodic potential associated with the positive ions in the crystal. In contrast to single atoms, for which the solutions of the Schrödinger equation are discrete electron energy levels, the periodic atomic arrangement therefore results in an energy band structure. It consists of a lower region and an upper region, which are separated by an energy gap, in which electronic states are forbidden. The highest energy band in the lower region is the valence band

Material	Density $\left(\frac{g}{cm^3}\right)$	λ_{max} (nm)	n	Decay Time (μs)	Abs. Light Yield (Photons/MeV)
NaI(Tl)	3.67	415	1.85	0.23	38000
BGO	7.13	480	2.15	0.30	8200
GSO	6.71	440	1.85	0.056 (90 %) 0.4 (10 %)	9000
YAP	5.37	370	1.95	0.027	18000
LSO	7.4	420	1.82	0.047	25000

Table 2.1.: Properties of scintillating materials commonly used for applications in nuclear medicine [49], where λ_{max} is the peak wavelength of the scintillation light and n the index of refraction.

and the highest filled band, whereas the lowest band of the upper region, which is the lowest unoccupied band, is called the conduction band.

The energy of an incident photon that is absorbed by such a scintillation crystal can lift an electron into the conduction band, leaving a hole in the valence band. When the electron falls from this excited state back into the ground state, x rays are emitted. It is possible, however, to disturb the crystal structure by targeted implantation of impurities, the so-called activators, resulting in additional localised energy levels in the forbidden gap between the energy bands. If an electron-hole pair, travelling through the scintillation crystal, is captured by an activator and relaxes back into the ground state, a photon with a wavelength in the visible range is emitted.

The ideal scintillator in PET should combine at least three main properties [4,15]. It should have a good stopping power and therefore a high atomic number to increase the probability for 511-keV annihilation photons to undergo Compton scattering in the crystal and thus the deposited photon energy. A short signal decay time is necessary for detection and analysis of different scintillation light pulses at high count rates. For best energy resolution, the ratio of emitted scintillation photons and absorbed energy must be highest. Properties of scintillating materials commonly used for applications in nuclear medicine are shown in Table 2.1.

Photodetectors

There are two major groups of photodetectors in use in clinical PET today, PMTs and semiconductor-based detectors.

The photomultiplier tube (PMT) is the best-established, most widely available and reliable photodetector used for PET (Figure 2.4). It consists of a vacuum tube with a thin photocathode, where the scintillation light enters the device, and an anode at the opposite end, a focussing grid and a number of metal plates between cathode and anode. These plates are called dynodes and coated with materials facilitating the ejection of secondary electrons, if hit by

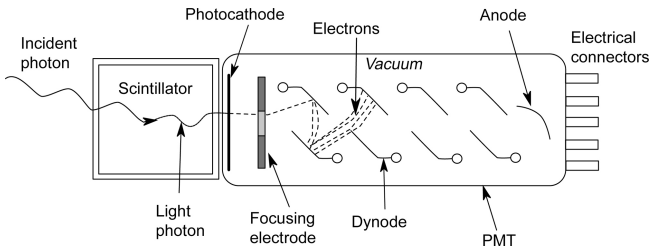

Figure 2.4.: A typical PMT [25]. It is a vacuum tube consisting of a photocathode, an anode and several dynodes in between. A primary electron is multiplied by a factor of approximately 10^6.

accelerated electrons. Each of the dynodes is at a positive potential relative to the cathode, increasing from cathode to anode. First, incident scintillation photons are absorbed and free electrons created in the cathode by the photoelectric effect. These electrons are then focussed by the first electrode, the focussing grid, and further accelerated towards the dynodes. At each dynode stage, striking electrons lead to the emission of several secondary electrons each. Finally, a shower of electrons can be detected at the final anode and measured as an electrical current. Due to an amplification of the original electron released from the photocathode of more than 10^6 at the anode [89], PMTs provide a high SNR. Their major disadvantage with regard to an application in integrated PET/MR is their sensitivity to magnetic fields [75]. The Lorentz force deflects electrons travelling in a magnetic field, thereby rendering the information obtained from PMTs useless for PET. Shielding is not an appropriate solution for several reasons. It is complex and difficult, thus increasing the cost of already expensive imaging systems. Moreover, the metal components required in the FOV of the MR for this purpose, distort the static magnetic field of the MR subsystem.

Despite a lower gain and hence a lower SNR, the group of semiconductor photodetectors is of high interest especially for the use in PET/MR imaging due to their insensitivity to magnetic fields. They are most commonly produced from materials such as silicon or germanium. As described for scintillators, electrons populate energy bands instead of discrete energy levels due to the periodic crystal structure of semiconductors. In the absence of electrons in the conduction band and without holes in the valence band, the material is an isolator. Incident scintillation photons can be absorbed in the semiconductor by means of the photoelectric effect, thereby ionising atoms and creating electron-hole pairs. This in turn allows a measurable current to flow, if an external voltage is applied. The signal resulting from this charge collection is then proportional to the amount of energy absorbed.

The APD is a more complex variant of the concept above. It is basically a double-layered junction consisting of a P-type semiconductor, in which impurities or dopants were implanted that supply additional vacancies, and an

N-type semiconductor with an abundance of electrons. Brought into contact, the charge carriers diffuse across the interface of the two layers, building up a space charge in this region, which is almost completely depleted of majority carriers, and an electric field with it. The application of a reverse-bias voltage increases both the electric field in this depletion region as well as its width. The voltages at which APDs are operated lead to electron energies that are sufficient for further ionisations, if transferred in a collision with an atom. The thus created secondary electrons are in turn accelerated, generating an avalanche of charge carriers. The amplification factor of APDs, which is approximately three orders of magnitude lower than that of PMTs [89], is sensitive to temperature [90] and to variations of the bias voltage [4]. In order to prevent unreliable PET measurements, the temperature of APDs must therefore be actively controlled and their bias voltage set accurately.

2.1.4. Data Acquisition

Coincidence Detection

It is the goal in PET to detect both photons originating from the same annihilation event. Since their emission can occur anywhere between two opposing detectors, the annihilation events will not be registered simultaneously by these detectors. For a PET ring diameter of 0.6 m and the speed of light of $3 \cdot 10^8 \ \frac{\mathrm{m}}{\mathrm{s}}$, the maximum possible time difference could amount to 2 ns, if the origin of the photons is directly near the front of one of the detectors. Therefore, two detection events are considered to be coincident and thus assumed to be from a single annihilation event, if they fall into the same time window. They are recorded as coincident events or simply coincidences, if they furthermore satisfy the requirements that the line of response (LOR) between the two detectors in which the photons were absorbed is of a valid acceptance angle of the detector system and that the energy deposited is within the window of accepted energies [3].

The advantage of the coincidence detection principle in PET is that physical collimators are not required to determine the LOR, the line on which the annihilation is assumed to have occurred. Such electronic collimation yields a higher detector sensitivity compared to physical collimation.

Coincidence Events

Four types of coincidence events can be distinguished, namely true, scattered and random coincidences, which are show in Figure 2.5, as well as multiple coincidences. The number of prompts is the sum of all true, scattered and random coincidences.

Two photons are called true coincidences, if they did not significantly interact with the surrounding matter on their path to the detectors and were

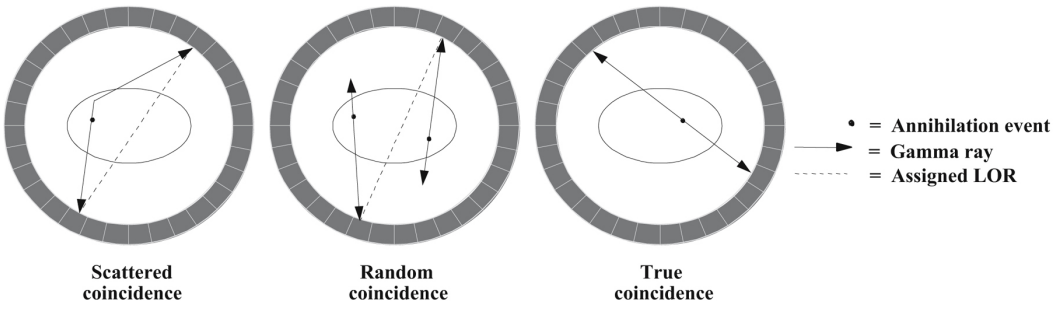

Figure 2.5.: Types of coincidence events that can be registered in PET (With kind permission of Springer Science+Business Media [64]).

recorded in a coincidence window in which no other events were detected. True coincidences are of highest interest for image generation in PET, because they yield the most accurate information.

Scattered coincidences denote pairs of annihilation photons of which at least one photon underwent Compton scattering before absorption in the detector. The corresponding change in direction means that the LOR assigned to this coincidence event most probably does not pass through the location at which the annihilation occurred. Although scattered annihilation photons could be identified according to their lower energies compared to unscattered 511-keV gamma rays, the energy resolution of PET detectors is still insufficient to successfully differentiate between these two in most cases. The consequence of scattered coincidences is added background noise in reconstructed images.

Random coincidences are recorded, if two atoms decay by positron emission almost simultaneously. If two of the four resulting photons are detected within the same coincidence window, but are otherwise unrelated, they are attributed to a single annihilation event and therefore represent a false coincidence event. The number of random coincidences is proportional to the width τ of the coincidence window as well as to the square A^2 of the activity A within the FOV of the PET detectors [15]. Their spatial distribution, however, is independent of the distribution of A, adding approximately uniform statistical background noise.

Multiple coincidences are similar to random coincidences as two annihilation events have to fall into one coincidence window. In contrast to random coincidences, more than two annihilation photons are registered, rendering the correct definition or even only an estimation impossible. Such events are immediately discarded.

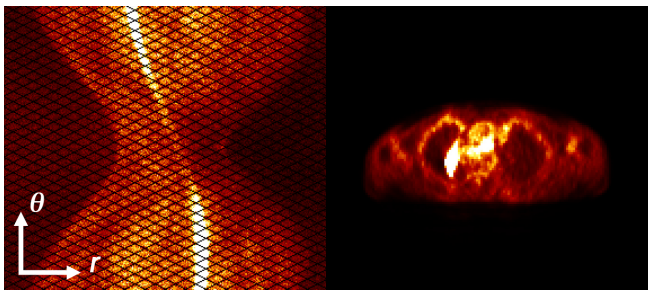

Figure 2.6.: A sinogram of a clinical ^{18}F-FDG PET scan (left) and the corresponding transaxial plane of the reconstructed image volume (right). Each sinogram bin (r, θ) represents the number of LORs detected with orientation θ and distance r from the centre of the detector ring.

2.1.5. PET Raw Data Formats

Sinograms

As was explained in the beginning of 2.1.4, a coincidence event is characterised by the LOR that connects the two detectors in which the annihilation photons were detected. LORs in turn can be defined by the angle of their orientation θ and their perpendicular distance r from the centre of the detector ring. Projection profiles or simply projections of the activity distribution within the FOV are derived by first grouping all measured coincidences according to θ of the corresponding LORs and subsequent histogramming of r. The complete set of projections can be combined to create a graphical representation of the coincidence data acquired during a PET measurement.

The so-called sinogram is a two-dimensional (2d) matrix of pixels with r along the x-axis and θ along the y-axis (Figure 2.6). Since a coincident event is recorded by two detectors and the entire distance between them is travelled by the annihilation photons, the information contained in the projections with $\theta = 180° \ldots 360°$ is the same as in those with $\theta = 0° \ldots 180°$ and therefore redundant. The value of each sinogram pixel (r, θ) is the number of coincidences detected along this LOR. Each line in a sinogram corresponds to a specific set of parallel LORs.

Separate sinograms are created for each detector ring and for each pairing of detector rings, if oblique LORs are allowed as it is the case in 3d acquisition. For a maximum ring difference of 60, the number of resulting sinograms is 4084. Considering sinograms with 344 radial bins and 252 projections and a size of 4 bytes per bin, the size of the uncompressed raw data amounts to 1.4 GB.

List Mode

For applications, such as dynamic PET studies or motion correction, histogramming of coincidence events into sinogram bins without temporal information is not sufficient. To overcome this shortcoming, PET raw data can be stored in list-mode format. As explained by Langner et al. [52], a list-mode file is a stream of 32-bit big-endian words, the event words, in which the coincidence information is encoded. Every millisecond, so-called time words are inserted, which carry the information of how much time has passed since the start of the scan. Gating and other information can be encoded into dedicated tag words as well. Whereas the sinogram size is clearly defined, the size of a list-mode file depends on the number of recorded coincidences and therefore on the scan length and the activity in the FOV of the PET detectors. Several gigabytes are not uncommon.

2.1.6. Quantitative PET

With PET, it is possible to detect single annihilation events and therefore single atomic decays. Consequently, images can be reconstructed, from which the activity concentration in any given region of the FOV can be determined. Apart from a measurement of the crystal efficiency, a prerequisite for such quantitative images is exact knowledge about attenuation and scattering of the gamma rays in the FOV.

Attenuation Correction

For a coincidence event to be recorded, both annihilation photons have to be detected. If only one of them is absorbed by a detector, the coincidence event is not registered and the count is lost. Considering a cylindrical volume that is homogeneously filled with activity, the apparent activity concentration in the reconstructed images would appear lower in the centre of the cylinder due to the higher attenuation than near its outer boundary.

The probability of a photon reaching the detector depends on the linear attenuation coefficient μ of the attenuating material along the LOR between two detectors and its thickness d, but not on the location x of the annihilation event. The probabilities P_1 and P_2 for either the first or the second annihilation photon to reach a detector are given by

$$P_1 = e^{-\mu x} \tag{2.4}$$

$$P_2 = e^{-\mu(d-x)} \tag{2.5}$$

The resulting probability for both annihilation photons to arrive at opposing detectors is the product of P_1 and P_2:

$$P_1 \cdot P_2 = e^{-\mu(x+d-x)} \quad (2.6)$$
$$= e^{-\mu d} \quad (2.7)$$

Thus, the problem of AC is reduced to measuring the attenuation along the LORs.

In the early days of PET, a rotating transmission source was used to determine attenuation coefficients [11, 40, 73]. In combined PET/CT examinations, the low-dose CT scan replaced the transmission scan [47], providing high spatial resolution and high image quality due to the superior count-rate statistics. As the photon energy in a typical CT attenuation scan is 120 keV, attenuation coefficients have to be converted for annihilation photon energies of 511 keV, which is complicated by the non-linear relationship between photon energy and attenuating properties of materials.

Scatter Correction

As outlined in 2.1.4, scattered coincidences hamper quantification of PET images by increasing background noise. Various methods exist to correct for scattered events, among them empirical scatter and simulation-based corrections, which can be further divided into analytical and numerical approaches.

Five distinct steps that all simulation-based methods have in common are explained in detail in [64]. The first is the reconstruction of an μ-map, for example, from measured CT data, followed by the reconstruction of emission data without any scatter correction applied. The crucial step is the estimation of the scatter contribution. A widely-used method by Watson et al. [101] simulates single scatter for an LOR between two detectors to calculate the corresponding count rates. This approach is feasible as the vast majority of scattered coincidences involve only one scatter event [64]. In the fourth step, the scatter estimation is scaled globally to achieve a good consistency with the emission data in regions outside of the patient, in which the measured activity can only be caused by scattered coincidences. Finally, the scatter estimate is subtracted from the original sinograms and scatter-corrected images reconstructed.

2.1.7. Image Reconstruction

Mathematical algorithms have to be applied to reconstruct from the previously acquired emission data images of specific slices through the FOV. The raw data must be a set of projections acquired at discrete angles and sampled at discrete intervals in radial direction. The final images contain a transaxial pixel matrix each.

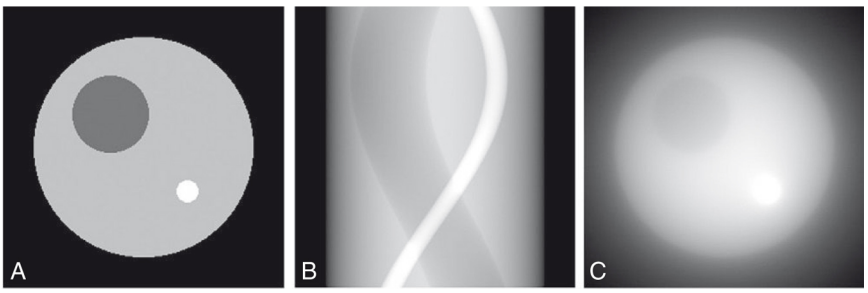

Figure 2.7.: A transaxial slice through a computer phantom (A), the corresponding sinogram for a simulated scan of this phantom (B) and the simple backprojection of this raw data. The $1/r$-blurring artefact caused by this reconstruction method is obvious in (C). (Reprinted from [15], with permission from Elsevier.)

Backprojection

The most straightforward image reconstruction technique is the simple backprojection [15]. Backprojection denotes the distribution over the image matrix of the counts registered for a specific LOR. The appropriate number of counts is attributed to a given image pixel according to the fraction of the LOR that passes through this pixel. This is repeated for each LOR, summing up the counts.

If, for simplification, the counts of an LOR are uniformly distributed over all pixels contributing to it, the reconstructed estimate of the measured activity distribution can be described by [15]

$$f'(x,y) = \frac{1}{N}\sum_{i=1}^{N} p(\underbrace{x\cdot\cos\phi_i + y\cdot\sin\phi_i}_{r}, \phi_i) \tag{2.8}$$

where N is the number of projections and ϕ_i the angle of the ith projection.

With the simple backprojection, counts are projected outside of the activity-containing volume elements, leading to a blurring artefact (Figure 2.7) that is proportional to the reciprocal of the distance from the centre of the volume element [15]. Filtered backprojection (FBP) removes this artefact by additional filtering in k-space. For this purpose, the acquired projections of the activity distribution are Fourier transformed (one-dimensional). A ramp filter is then applied to each k-space profile, amplifying the high-frequency and suppressing the low-frequency components. After inverse Fourier transform of the k-space profiles, the filtered profiles are backprojected. If the data is perfectly-measured and free of noise, the resulting images show the true activity distribution and not an estimate of it as for the simple backprojection.

As explained in [15], a major disadvantage of FBP is that the applied filter also amplifies high-frequency noise. Moreover, artefacts arise, if the emission data is incomplete due to detector failures or objects that are truncated in

some projections. Additionally, poor counting statistics lead to streaks in the reconstructed images.

Iterative Reconstruction Algorithms

With iterative reconstruction algorithms, the true activity distribution is approximated by successively improving an initial images estimate, which can be as simple as a blank or uniform image. This image is then forward-projected into sinogram space by summing up the pixel values along all possible LORs and thus calculating the complete set of projections. In the next step, the estimated sinogram is compared to the acquired sinogram and update factors computed. After backward projection of this information into image space, the image estimate is updated accordingly. This process is repeated until the difference between the forward-projected estimate and the measured emission data is sufficiently small.

Iterative reconstruction algorithms are regarded to perform better than FBP, especially in low-count regions, where they significantly reduce image noise, thus improving SNR [83].

2.2. Magnetic Resonance Imaging

The human body is composed of fat and water, which in turn primarily consist of hydrogen atoms. The only constituent of the hydrogen nucleus is the proton, a particle with a distinct quantum-mechanical property called the spin. The value of the spin is a multiple of $\frac{1}{2}$, and protons in particular have spins of $+\frac{1}{2}$. With this spin, a magnetic moment is associated.

The proton can be in one of two spin states, the spin-up state with the magnetic quantum number $m = +\frac{1}{2}$ and the spin-down state with $m = -\frac{1}{2}$. In the absence of a magnetic field, both states have equal energies. If a proton is placed in an external magnetic field B_0, two different energy levels emerge. The lower level, in which its magnetic moment is aligned with the magnetic field, is associated with $m = +\frac{1}{2}$, and the upper level, if its magnetic moment is aligned against it, with the spin-down state. At room temperature, both spin states are populated, with a slightly higher number of protons in the lower spin state, resulting in a net magnetisation of the corresponding sample. The exact ratio of protons in the upper to protons in the lower spin states is determined by Boltzmann statistics.

The energy of the magnetic moment in a magnetic field can be calculated according to

$$E = -\gamma m \hbar B_0 \tag{2.9}$$

where γ is the gyromagnetic ratio and $\hbar$ the reduced Planck constant. The difference between the two energy states is therefore

$$\Delta E = \gamma \hbar B_0 \tag{2.10}$$

If a photon with that energy is absorbed, the proton spin is lifted into the upper state, changing the net magnetisation of the corresponding sample. The corresponding resonance frequency ν is approximately 128 MHz for a magnetic field strength of 3 T and the gyromagnetic ratio $\frac{\gamma}{2\pi} = 42.58\ \frac{\mathrm{MHz}}{\mathrm{T}}$ of hydrogen.

When the net magnetisation relaxes into the thermal equilibrium state, RF signals are emitted, which form the MR signal to be measured. Two processes are involved in the relaxation of spin populations, T_1 or spin-lattice relaxation and T_2 or spin-spin relaxation. As the relaxation time depends on the surrounding tissue, contrast is created. In clinical examinations, the MR signal is enhanced by the administration of CA, which shorten the T_1 and T_2 relaxation times [5].

In a uniform magnetic field, the origin of the received RF signals cannot be determined. All volumes with spin populations and the same chemical composition contribute to a single peak in the frequency spectrum, which is

obtained by means of Fourier transform of the RF signals. However, spatial information can be encoded by application of linear one-dimensional (1d) gradient fields G_x, G_y and G_z along the x-, y- and z-axis, respectively. Such frequency encoding takes advantage of the magnetic-field dependency of the resonance frequency, leading to more than one peak.

However, it is still not possible to generate 2d images with constant 1d gradient fields. Considering a constant magnetic field and the application of a gradient G_x, all spins in a plane orthogonal to the x-axis are subject to the same magnetic field strength. As the superposition of 1d gradients is also a 1d gradient, the mapping of RF signals to positions remains ambiguous. As explained in [38], the problem can be solved with time-variant magnetic fields, where the variation is unique for each position. The concept of k-space takes this into account as it is the higher dimensional Fourier transform of the MR image space. Complete image data can only be derived from complete k-space data. Therefore, a broad variety of strategies for efficient sampling of k-space were developed [38].

A tomographic imaging system, based on the above principles, comprises three main components, a permanent magnet, gradient coils and RF coils. The permanent magnet is mostly made from superconducting materials and therefore helium-cooled to temperatures close to 0 K. It is also possible to reduce the fringe field outside of the bore of the system with the application of proper shielding.

The gradient coils are located within the superconducting magnet. They are employed to produce G_x, G_y and G_z and operated at room temperature. In the case of G_z, the gradient field parallel to B_0, a Helmholtz coil is used through which currents flow in opposing directions, whereas G_x and G_y can be generated by Golay coils [97].

RF coils are located closest to the patient and transmit the RF pulses for spin excitation and receive the emitted MR signals. Such coils can be receive-only or both transmit and receive.

Part II.

Performance Studies of an Integrated Clinical Whole-body PET/MR System

3. Performance Measurements of the Biograph mMR

Based on the work published in
Journal of Nuclear Medicine
(G. Delso*, S. Fürst* et al.,
J Nucl Med 2011; 52:1914–1922)

3.1. Introduction

The potential of multimodal imaging for improved non-invasive tissue characterisation was recognised in clinical and preclinical applications [96]. This potential is reflected in the extensive research effort dedicated to software coregistration in the 1990s and the immediate success of combined PET/CT scanners after their introduction in the early 2000s [6].

Combining the high soft-tissue contrast of MR and molecular signals from PET may provide further multimodal assessment, reaching beyond the anatomic correlation by introducing functional MR as well. There are considerable advantages to integrating these modalities in a single scanner [107]. The possibility of truly simultaneous operation allows the acquisition of several MR sequences during the PET scan, without increasing the examination time. Additionally, the radiation exposure is reduced if CT is not necessary.

The combination of MR and PET scanners is highly challenging. The high static magnetic field, quickly changing gradient fields, and RF signals from the MR scanner prevent the normal operation of PMTs and may induce interference in the front-end electronics of PET detectors. Furthermore, the presence of the PET detector causes inhomogeneities in the magnetic field, eddy currents and electromagnetic interference, potentially degrading MR image quality. These issues lead to a trade-off in the design of shielding elements to isolate both scanners.

Several approaches have been reported to overcome these problems: using two separate scanners sharing the same patient bed [79], integrating the PET scintillators in the MR scanner and guiding the scintillation light to a shielded enclosure outside the fringe field [12, 33, 75, 88], using a custom magnet

*Contributed equally to this work.

architecture [88], using field-cycled MR image acquisition to create intervals in which PET acquisition is possible [33] and redesigning the PET front-end using photodetectors that are insensitive to the magnetic field. The feasibility of using APDs for PET detectors up to a high field strength was demonstrated by researchers at the Department of Nuclear Medicine at Klinikum rechts der Isar of Technische Universität München [75]. Systems based on APD detectors coupled with lutetium oxyorthosilicate (LSO) crystals for simultaneous PET/MR were developed for preclinical research [12]. Also, following the concept of a PET insert in an MR scanner, a preclinical device was recently presented, based on Geiger APDs [85].

Two of these approaches led to commercially available clinical scanners: the Philips Ingenuity TF, based on two separate scanners sharing a rotating bed [108], and the Siemens Biograph mMR, which uses APD-LSO PET detectors integrated between the MR body coil and the gradient coils. The main advantage of using separate scanners is to keep mutual interference to a minimum, thereby reducing the need for PET detector redesign. The main advantage of the integrated approach is the possibility of truly simultaneous isocentric acquisition.

The goal of this study was to determine the performance characteristics of the Biograph mMR system, focusing on the use of morphologic MR measurements simultaneous to PET acquisitions. Two widely accepted measurement protocols were used: the NEMA NU 2-2007 protocol [65] for the PET and the ACR quality control manual [1] for the MR subsystem. The performance degradation due to the integrated architecture can be quantified by comparing these measurements with those reported for other state-of-the-art scanners.

3.2. Materials and Methods

A set of performance measurements was obtained on an integrated PET/MR scanner. The PET subsystem was evaluated following the NEMA NU 2-2007 protocol [65]. Before any measurements were taken, a detector set-up was performed, including photodetector gain equalisation, crystal region map generation and crystal energy peak adjustments, followed by time alignment and a normalisation scan.

The MR subsystem was evaluated following the ACR quality control manual [1]. In addition, RF field homogeneity and RF interference measurements were performed.

These measurements were repeated under identical conditions in a state-of-the-art MR scanner (Magnetom Verio, Siemens Healthcare, Erlangen, Germany). The Verio has essentially the same specifications as the PET/MR, except for a larger bore of 70 cm.

A detailed description of the PET/MR can be found in 3.2.1.

3.2.1. Biograph mMR PET/MR System

The scanner under investigation (Biograph mMR, Siemens Healthcare, Erlangen, Germany) is the first fully integrated clinical whole-body PET/MR system. Its MRI subsystem is based on a 3-T niobium-titanium superconducting magnet with a length of 163 cm and a bore diameter of 60 cm. It further contains an actively shielded whole-body gradient coil system and a RF body coil. The gradient coil system has a length of 159 cm, an amplitude of 45 mT/m and a slew rate of 200 T/m/s, whereas the RF body coil has a transmitter bandwidth of 800 kHz and a peak power of 35 kW. The MRI is capable of acquiring FOVs between 0.5 cm and 50 cm with a 2d slice thickness between 0.1 mm and 200 mm and a 3d slab thickness between 5 mm and 500 mm. The maximum matrix size amounts to 1,024 elements, leading to a maximum resolution of 9 μm.

The PET component of this system is located between the gradient and RF body coils (Figure 3.1). It comprises 8 rings with 56 detector blocks each, which in turn consist of an assembly of 8 $\times$ 8 LSO crystals with an individual element size of 4 $\times$ 4 $\times$ 20 mm^3. This assembly is then read out by an array of 3 $\times$ 3 APDs. Front-end electronics and water-cooling channels are integrated into the detector blocks as well. In total, the tomograph contains 448 detector blocks, 4,032 APDs and 28,672 crystals. It has a transaxial FOV of 59.4 cm and an axial FOV of 25.8 cm. The energy resolution was measured to be 14.5% (with ^{68}Ge in air) and the time resolution 3.6 ns. The window of accepted energies is set to between 430 keV and 610 keV, whereas the coincidence window has a width of 5.86 ns. Due to the APD timing properties, this system is not equipped with time-of-flight capabilities. It can perform static multibed and list-mode data acquisitions in 3d. Random events

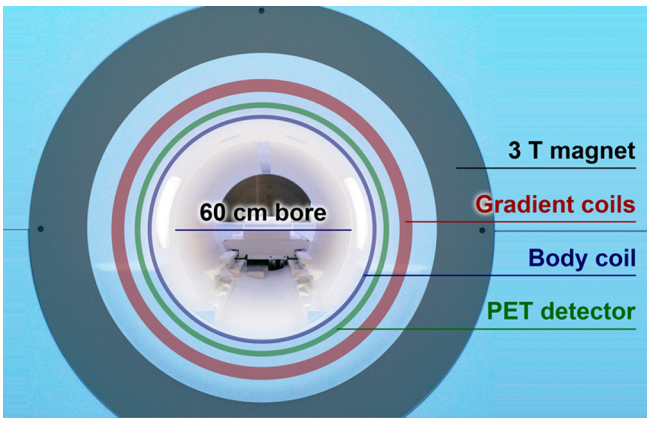

Figure 3.1.: Diagram of the Biograph mMR. The PET detectors are located between the different MR coils.

are estimated by means of the delayed-window technique.

The acquisition workflow allows for defining protocols of PET acquisition while simultaneously running standard MR clinical pulse sequences.

3.2.2. PET Spatial Resolution

A glass capillary with an inside diameter of 1.1 mm, a wall thickness of 0.2 mm and length of 75 mm was filled with ^{18}F solution. The axial extent of the activity within the capillary was limited to 1 mm by an absorbing resin. The total activity in the capillary was 9.6 MBq.

The capillary was positioned parallel to the scanner axis using a frame that was provided by the manufacturer and fixed to the calibration phantom holder situated at the head of the patient bed. The position of the source was adjusted by means of short sinogram acquisitions. Data were successively acquired at the (x, y) locations of $(0\text{ cm}, 1\text{ cm})$, $(10\text{ cm}, 0\text{ cm})$, and $(0\text{ cm}, 10\text{ cm})$ in the transaxial plane. These measurements were each taken at two axial positions, at the centre of the FOV and at 65 mm, that is, one-quarter of the FOV, off the centre. The bed stayed outside the FOV during these measurements.

Each configuration was scanned until $2 \cdot 10^6$ counts were acquired. All data was taken within 20 min of the initial activity measurement. The scans were reconstructed using Fourier rebinning and FBP with a ramp filter. The image matrix contained $344 \times 344 \times 127$ voxels with a size of $1.04 \times 1.04 \times 2.03$ mm^3 each. The full width at half maximum (FWHM) and full width at tenth maximum (FWTM) of the source response function were computed by linear interpolation in the axial, radial and tangential directions.

To evaluate the impact of simultaneous operation of both subsystems, each measurement was repeated while running a volumetric interpolated breath-hold examination (VIBE) sequence with a repetition time (TR) of 20 ms, a echo time (TE) of 1.17 ms and a flip angle of 10°.

3.2.3. PET Scatter Fraction, Count Losses and Randoms

A 700-mm portion of a polyethylene tube with an inside diameter of 3 mm and an outside diameter of 4.8 mm was filled with 1.3 GBq of ^{18}F-FDG solution. The tube was then inserted into a 6.5-mm hole drilled parallel to the axis of a solid polyethylene cylinder with an diameter of 202 mm and a length of 695 mm. The cylinder was supported by a pair of polystyrene holders to keep it centred in the FOV.

This set-up was then scanned in 10-min frames for 450 min, starting when the activity reached 675 MBq. Uncorrected prompt and random sinograms were generated and rebinned using single-slice rebinning (SSRB). The original sinograms had 344 bins with a size of 2.0445 mm each and 252 views. They were stored with an axial compression of 1 and maximum ring difference of 60. The randoms estimation of the Biograph mMR was obtained using the delayed coincidence window method and smoothing.

The sinograms were then processed following the NEMA protocol to calculate for each slice the system scatter fraction as well as the true, random, scatter and total count rates, as well as the noise-equivalent count rate (NEC rate).

Additionally, a 5-min list-mode acquisition was performed in the absence of any activity to evaluate the dark count rates.

3.2.4. PET Sensitivity

A 700-mm portion of a polyethylene tube was filled with 2.4 mL of an ^{18}F-FDG solution with a total activity of 4.8 MBq. The tube was inserted into a concentric arrangement of five aluminum sleeves. The sleeves had a length of 700 mm, inside and outside diameters of 3.9 mm and 6.4 mm, 7.0 mm and 9.5 mm, 10.2 mm and 12.7 mm, 13.4 mm and 15.9 mm, and 16.6 mm and 19.1 mm. The whole set-up was aligned with the scanner axis and fixed to the bed rails using a pair of polystyrene holders. The bed stayed outside the FOV during these measurements.

A set of 5-min acquisitions was automatically performed, starting 16 min after the initial measurement of activity. One acquisition was performed with the activity centred in the FOV and a second with the source placed 10 cm off-axis. This was repeated five times, each time removing one of the aluminum sleeves.

Each of the previous measurements was immediately repeated while running a VIBE sequence with the same parameters as in 3.2.2.

For each acquisition, an uncorrected sinogram was created and rebinned using SSRB. Estimated random coincidences were subtracted. The total number of acquired counts was recorded for each slice of the sinogram, corrected for isotope decay and then summed. The five count rates for each source position were fit with an exponential model to extrapolate to the count rate in

the absence of attenuating material. The system sensitivity is defined as the count rate without attenuation divided by the activity in the tube. The axial sensitivity profile of the system was generated using the data collected for the smallest sleeve at a radial offset of 0 cm.

3.2.5. PET Accuracy

PET accuracy was measured using the data acquired as described in 3.2.3. Each dataset was rebinned using Fourier rebinning, and 2d reconstruction was performed using FBP. Randoms subtraction, decay correction, arc correction, scatter correction and AC were applied. The required μ-map was calculated.

After reconstruction, a centred, 180-mm circular region of interest was defined on each transaxial slice of each acquisition and the true count rate in the region calculated. The true count rate in the absence of randoms and dead-time losses was estimated by averaging the three acquisitions with the lowest activity. From these values, the relative count-rate error was computed for each slice of each acquisition.

3.2.6. PET Image Quality

For the measurement of PET image quality, a body phantom with an interior length of 175 mm, an interior width of 293 mm and an interior height of 224 mm was used. A cylindric insert with an outside diameter of 50 mm and a length of 175 mm, filled with low-density foam, was fixed along the centre of the body phantom. Six spheres with internal diameters of 10 mm, 13 mm, 17 mm, 22 mm, 28 mm and 37 mm were placed in the body phantom, aligned in a transaxial plane 68 mm from the phantom endplate and distributed around the phantom axis at a distance of 5.72 cm. The two largest spheres were filled with water and the others with an aqueous solution of ^{18}F-FDG. The activity concentration of this solution amounted to 17 kBq/mL. The body phantom was then filled with 42 MBq of ^{18}F-FDG solution to provide a background uptake of 4.27 kBq/mL, placed in the scanner and centred in its FOV. The solid cylinder used as described in 3.2.3 was fitted with a line source filled with 81 MBq of ^{18}F-FDG solution and placed along the patient bed, abutted to the body phantom. All activity values provided above are corrected for decay with the start of the measurement as reference.

The phantom was scanned for 10 min. The axial extent covered by the acquisition was 258 mm. The acquired sinogram was reconstructed using the 3d ordinary Poisson ordered-subset expectation maximisation (OSEM) algorithm with 4 iterations and 21 subsets, $172 \times 172 \times 127$ voxels and a voxel size of $4.2 \times 4.2 \times 2.0$ mm. Normalisation, correction for dead-time, decay and 3d scatter were applied as well as randoms smoothing and a 4-mm axial and transaxial postreconstruction Gaussian smoothing filter. This acquisition

was repeated three times, whereas the scan time was adjusted to account for decay.

Since the current implementation of the MR-based μ-map is specifically designed for patients (4.2.3), the μ-maps obtained for the image quality phantom were not usable due to inadequate relaxation times and resonance effects. Instead, a calculated μ-map was manually registered to the acquired data and used for reconstruction. The water-filled regions in this map were assigned an attenuation coefficient of 0.096 cm^{-1} and the lung insert an attenuation coefficient of 0.034 cm^{-1}.

On each of the acquired images, the percentage contrast and the percentage background variability were calculated for each sphere following the NEMA protocol. This processing was repeated with different numbers of reconstruction iterations, ranging from one to five iterations, to evaluate the convergence properties of the reconstruction algorithm. Additionally, the residual error in the scatter and attenuation corrections was calculated for each slice.

The image quality measurement was repeated while running the same VIBE sequence as described in 3.2.2.

3.2.7. PET System Stability

Stability of response with fluctuations in temperature is a concern with APD-based systems [90]. During the daily quality control procedure using a homogeneous cylindric ^{68}Ge phantom, a quantification factor is automatically computed to determine the ratio between the activity in the scanner and the detected counts. The calibration factor and decay-corrected true counts were monitored for a period of two months.

3.2.8. MR Image Quality

For these measurements, the ACR MR accreditation phantom was used [1]. It is a sealed cylinder of acrylic plastic, filled with a solution of 10 mM $NiCl_2$ and 75 mM NaCl. The interior of the phantom is 148 mm in length, with a diameter of 190 mm, and contains a set of plastic structures that can be used for a variety of performance measurements. The phantom was inserted into the head coil and centred in the FOV.

One sagittal slice with a thickness of 20 mm was acquired using a spin-echo localiser sequence with a TR of 200 ms and a TE of 20 ms. It had a FOV of 25 cm, providing a 256×256 matrix. The scan time was 56 s. The localiser facilitated the positioning of a T1-weighted spin-echo sequence with a TR of 500 ms and a TE of 20 ms. This sequence covered a FOV of 25 cm with a 256×256 matrix, generating 11 slices with a thickness of 5 mm and a gap of 5 mm between the slices. The accuracy of slice positioning was evaluated by measuring the length difference of two crossed 45°wedge structures.

The geometric accuracy was evaluated by measuring the phantom's length in the sagittal localiser image and its x and y diameters in the images from the T1 sequence.

For the high-contrast spatial resolution evaluation, the number of element rows and columns that could be individually discerned in a resolution insert was determined. The insert is a plastic structure containing three pairs of 4×4 arrays of water-filled holes. The spacings between the holes in each pair are 1.1 mm, 1.0 mm and 0.9 mm, respectively.

Slice thickness accuracy was determined by comparing the distances between two signal ramps. The slice position accuracy was evaluated by measuring the length difference between the wedge structures used to position the slices.

The uniformity of the image intensities was measured in a uniform section of the phantom, by comparing the average intensities of two ROIs with a size of 1 cm^2 each, placed in the regions of highest and lowest intensity.

Percentage signal ghosting was estimated in the same slice by means of four ROIs with a size of 10 cm^2, placed next to the phantom. The average intensity of the ROIs in the frequency encode direction was subtracted from the average in the phase encode direction and then normalised to the average intensity in the phantom.

Low-contrast detectability was evaluated on low-contrast disk structures. The number of complete disk spokes was registered for each axial slice.

3.2.9. MR Magnetic Field Homogeneity

With this measurement, the uniformity of the static B_0 field was evaluated over a spherical volume with a diameter of 24 cm, centred in the FOV. Of the two possible methods listed in the ACR quality control manual, the phase difference map method was selected.

A spherical non-conducting phantom (D240, Siemens Healthcare, Erlangen, Germany) was used for these measurements and placed inside the body loader using the provided phantom holder. It had an outer diameter of 240 mm and was filled with 7,300 mL of Marcol oil.

Two consecutive single-slice gradient-recalled echo sequences were acquired, with TEs of 17 ms and 20 ms, respectively. The phase maps of the images were recorded. This procedure was executed three times, acquiring three orthogonal planes centred in the phantom.

Each pair of phase images was unwrapped and subtracted to obtain a phase difference image. Phase images were, in turn, converted to B_0 field differences with respect to the center of the FOV, as described in the ACR quality control manual.

3.2.10. MR Radiofrequency Field Homogeneity

To estimate the uniformity of the RF B_1 field, the uniformity of the flip angle induced on a homogeneous phantom is measured. The measurement set-up is the same as described in 3.2.9.

The novel non-equilibrium B_1 mapping method [32] makes use of a recently observed linear relation between the frequency of oscillations in the transient phase of unbalanced steady-state free precession sequences and the actual flip angle [31]. For sufficient repetitive deviation from the steady state in the dynamic 3d acquisitions, software triggering was applied with a period of 500 ms to alternate trains of steady-state free precession blocks of 57 Cine phases with idle periods. The 3d acquisitions had a matrix of $64 \times 52 \times 4$ and an isotropic resolution of 5 mm. Steady-state free precession parameters were a flip angle of 24°and a TR/TE of 3.46 ms/1.71 ms. Data were exported for offline frequency analysis, performed with a singular value decomposition technique.

3.2.11. MR Radiofrequency Interference

To determine whether the PET detector electronics interferes with the acquired MR signals, RF noise measurements were performed with the PET detectors powered off, the detectors powered on and with the detectors on and an active ^{68}Ge calibration phantom in the scanner. To ensure a proper loading of the coils, the 24-cm spherical phantom and the phantom loader were placed in the FOV. The germanium phantom was placed axially adjacent to this set-up.

The RF noise sequence sets the MR scanner in receive-only mode, scanning a 500-kHz range around the scanner's center frequency of 123.2 MHz in steps of 39.1 Hz per pixel. The measurement of each frequency step was repeated 256 times. These measurements were then averaged to yield the power spectrum of the received noise.

The SNR from gradient echo (GRE) (TR, 100 ms; TE, 10 ms; slice thickness, 5 mm; bandwidth, 260 Hz/Px) and spin echo (TR, 600 ms; TE, 12 ms; slice thickness, 5 mm; bandwidth, 130 Hz/px) sequences was evaluated. Images from the same patient, scanned both on the Biograph mMR and the Verio, were analysed using the difference method described in the work by Firbank et al. [27].

3.2.12. In-vivo Studies

Two in-vivo studies were included to illustrate the performance of the Biograph mMR with clinical images.

The first is an ^{18}F-Fluoride study, indicated to localise possible bone metastases of prostate cancer. The same patient was scanned with a PET/CT

(Biograph TrueV, Siemens Healthcare, Erlangen, Germany) 41 min post injection (p. i.) and 158 min p. i. with the Biograph mMR. The injected activity was 331 MBq. Eight bed positions were acquired with a scan duration of 3 min per bed position in both cases. The data were reconstructed using Fourier rebinning and an OSEM algorithm with 4 iterations and 8 subsets on the Biograph TrueV and a 3d OSEM with 3 iterations and 21 subsets on the Biograph mMR.

The second case was a scan of a healthy volunteer employing a 3d T2-weighted TIRM turbo spin-echo sequence with fat saturation through inversion recovery. The acquisition parameters were as follows: TE, 34 ms; TR, 3,000 ms; inversion time, 220 ms; echo train length, 73; slice thickness, 4 mm; pixel spacing, 1.19 mm. The patient was scanned with identical parameters in the Verio and the Biograph mMR.

At...	FWHM (mm)	FWTM (mm)
10-mm radius		
Transverse	4.3 (4.3)	7.9 (7.9)
Axial	4.3 (4.3)	8.4 (8.4)
100-mm radius		
Transverse radial	5.2 (5.2)	9.7 (9.8)
Transverse tangential	4.8 (4.8)	11.9 (11.9)
Axial	6.6 (6.6)	13.1 (13.1)

Table 3.1.: Axial, radial and tangential resolutions. For each radius, resolution values of both axial positions were averaged. Values in parentheses are those obtained when the MR sequence was running.

3.3. Results

3.3.1. PET Spatial Resolution

The axial, radial and tangential resolutions for each radius, averaged for both axial positions, can be found in Table 3.1.

3.3.2. PET Scatter Fraction, Count Losses and Randoms

The measured true, scatter, random, NEC and total event rates are plotted in Figure 3.2 as a function of the average effective activity concentration, that is, the average activity for a given acquisition divided by the volume of the phantom, as described in the NEMA protocol.

The peak true count rate had a value of 692 kcps and was reached for an activity concentration of 23.1 kBq/mL. The peak NEC rate was reached for the same activity concentration and had a value of 184 kcps.

The scatter fraction is plotted in Figure 3.2C as a function of the average effective activity concentration. The scatter fraction value at the peak NEC rate was 37.9%.

The dark count rate had a prompts average of 820 cps and a standard deviation of 26 cps.

3.3.3. PET Sensitivity

The axial sensitivity profile for an axial offset of 0 cm is plotted in Figure 3.3.

The measured system sensitivity was 15.0 kcps/MBq along the centre of the scanner and 13.8 kcps/MBq at a radial offset of 10 cm. With a MR sequence running, the sensitivity values were 15.0 kcps/MBq and 13.8 kcps/MBq, respectively. These results correspond to a system sensitivity of 1.5% both with and without the MR running.

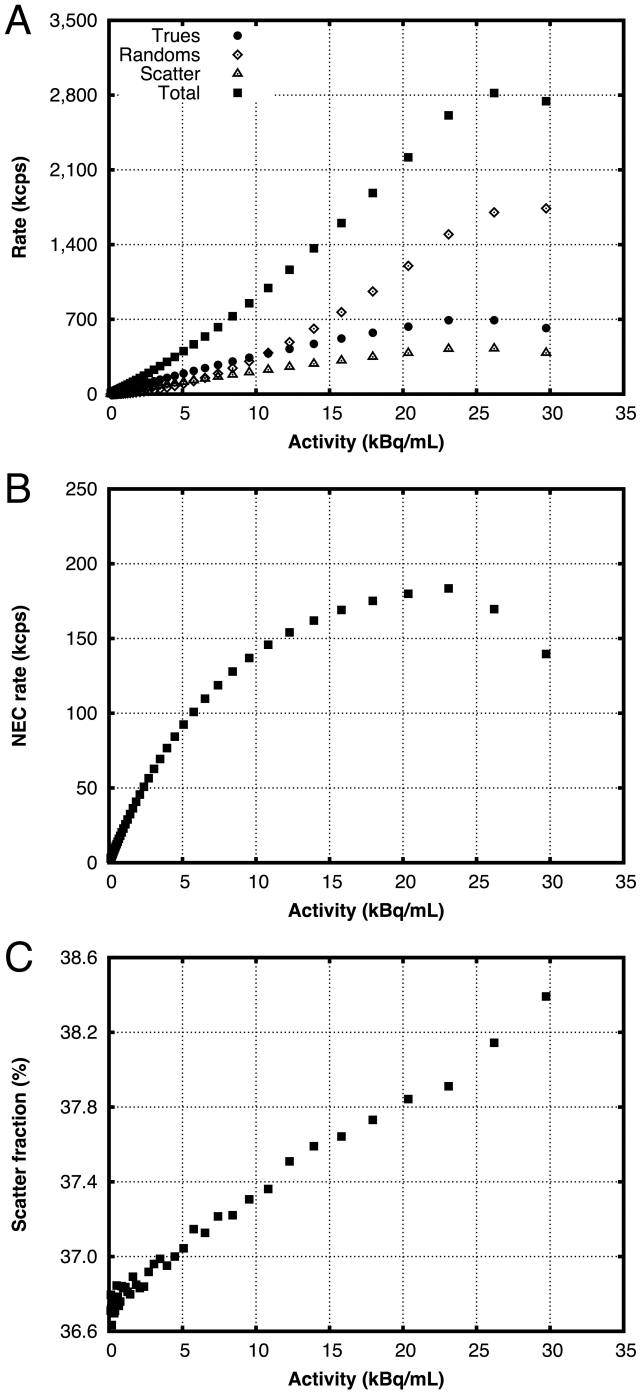

Figure 3.2.: Event rates (A), NEC rate (B) and scatter fraction (C) as function of average effective activity concentration.

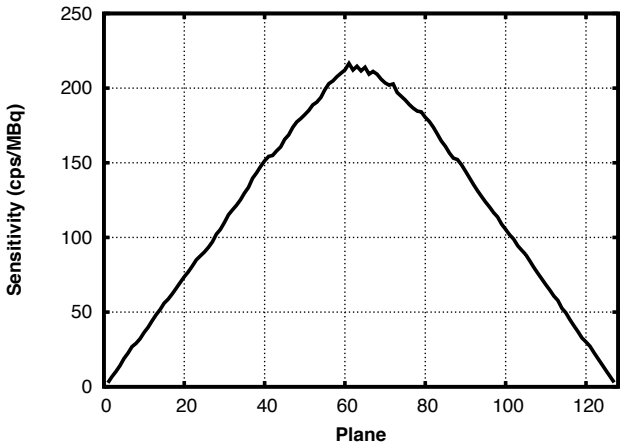

Figure 3.3.: Axial sensitivity profile for a radial offset of 0 cm.

3.3.4. PET Accuracy

Figure 3.4 shows the maximum and minimum values of the relative count rate error among the slices of each acquisition, plotted against the average effective activity concentration. The first and last two planes of the reconstructed volume were excluded because of their significantly lower sensitivity. If these slices are included, the maximum values of the relative count rate error remain unchanged, but the minimum values can reach -12%.

The maximum absolute value of the relative count-rate error at activities below that yielding the peak NEC rate (23.1 kBq/mL, according to 3.3.2) was 5.5%.

3.3.5. PET Image Quality

Table 3.2 shows the percentage contrast and background variability of each sphere. The average residual error in the lung insert due to scatter and attenuation was 12.1% $\pm$ 0.3%.

Transverse and coronal images of the reconstructed image volume are shown in Figure 3.5. No artefacts related to the simultaneous MR were found.

The impact of the number of reconstruction iterations on the contrast and background variability of the reconstructed hot spheres is shown in Figure 3.6.

3.3.6. PET System Stability

No time-dependent drift could be noticed in the calibration factor (Figure 3.7). The standard deviation of the calibration factor was 0.4%.

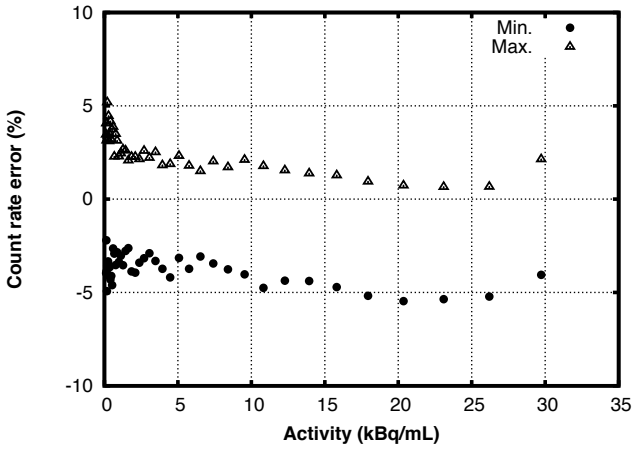

Figure 3.4.: Maximum and minimum values of relative count rate error as function of average effective activity concentration.

Diameter (mm)	Contrast (%)	Background variance (%)
10	32.5 ± 5.1	5.3 ± 1.0
13	50.0 ± 9.2	4.8 ± 0.8
17	62.9 ± 7.2	4.2 ± 0.5
22	70.8 ± 6.0	3.7 ± 0.3
28	65.1 ± 1.2	3.3 ± 0.2
37	72.3 ± 1.1	3.0 ± 0.1

Table 3.2.: Percentage contrast and percentage background variability of spheres

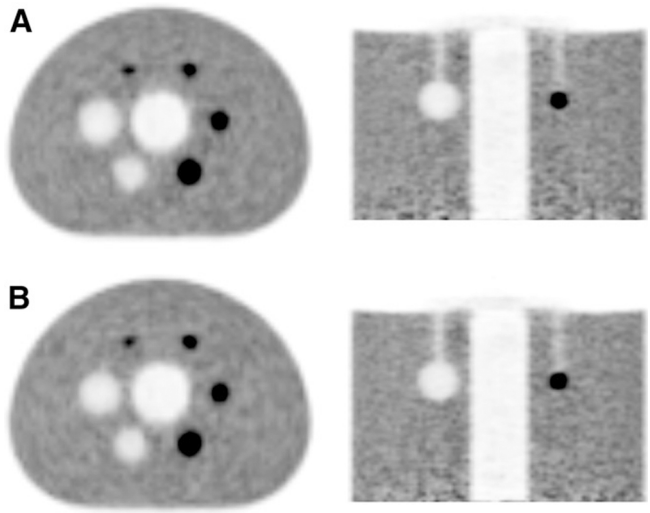

Figure 3.5.: (A) Axial and coronal views of the reconstructed image-quality phantom. (B) Corresponding views of the measurement with simultaneous MR image acquisition.

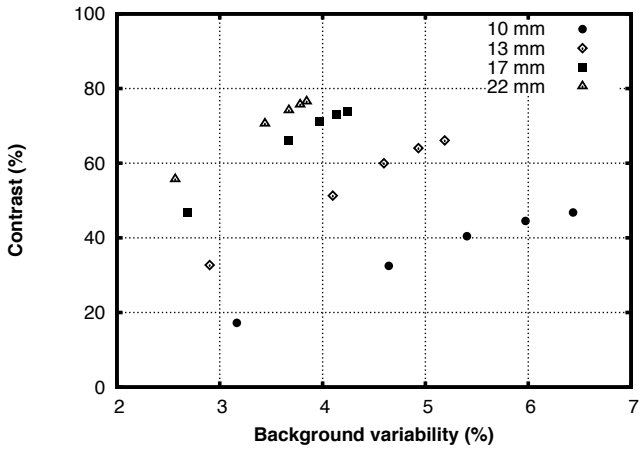

Figure 3.6.: Effect of the number of reconstruction iterations (1 to 5 iterations) on the contrast and background of the reconstructed spheres.

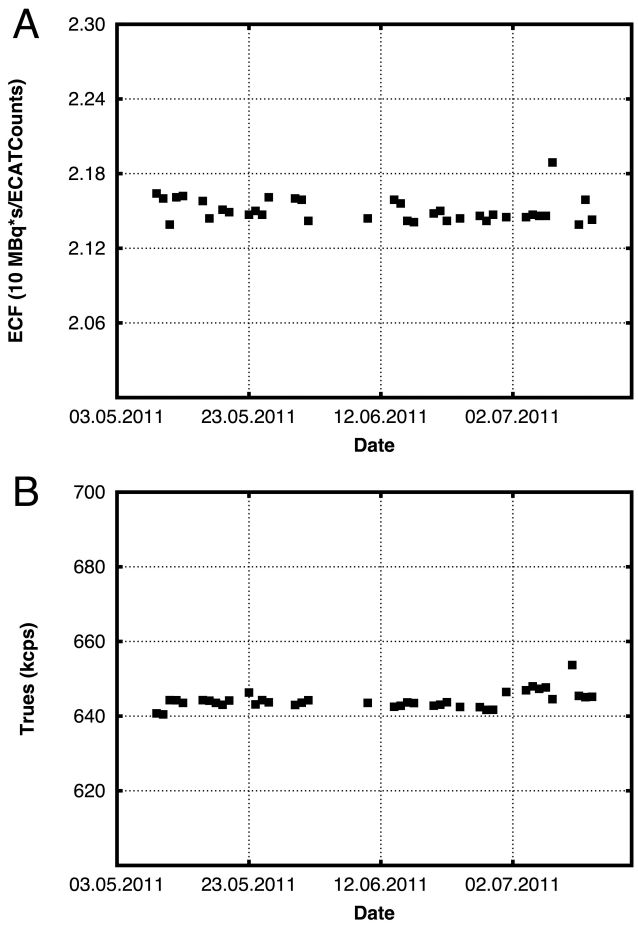

Figure 3.7.: Temporal evolution of (A) the calibration factor of the scanner and (B) decay-corrected true counts during calibration.

Parameter	mMR	Verio	Reference
Geometric accuracy			
Length (mm)	147.9	147.2	148.0 ± 2
Diameter (mm)	189.6 ± 1	189.9 ± 0.5	190.0 ± 2
High-contrast spatial resolution (mm)	0.9	0.9	< 1.1
Slice thickness accuracy (mm)	5.2	5.2	5.0 ± 0.7
Slice position accuracy (mm)			$\lvert\Delta d\rvert < 4$ mm
Slice 1	$+0.5$	-2.4	
Slice 11	-2.8	-2.9	
Image intensity uniformity (%)	89.6	87.3	> 82
Percentage signal ghosting	$0.4 \cdot 10^3$	$0.9 \cdot 10^3$	$< 25 \cdot 10^3$
Low-contrast object detectability	38	39	> 37

Table 3.3.: Results obtained following MR image quality tests described in the ACR Quality Control Manual. Recommended action criteria are included as reference.

3.3.7. MR Image Quality

The results of the image quality tests are summarised in Table 3.3. The Biograph mMR and the Verio passed all tests.

3.3.8. MR Magnetic Field Homogeneity

Figure 3.8 shows the maximum static field inhomogeneities in a centred sphere as a function of sphere radius. The results obtained with both the Verio and the Biograph mMR are included.

Notice how the sharp increase of inhomogeneity shown by both curves for the largest radii is likely to be caused by local effects at the phantom edges, rather than by an intrinsic inhomogeneity of the static field.

3.3.9. MR Radiofrequency Field Homogeneity

Figure 3.9 shows the measured flip angles in an axial slice through the centre of the phantom, for the Verio and Biograph mMR. The deviations from the target flip angle of 24° reflect the inhomogeneities of the RF excitation field. The observed differences are negligible and may be caused by the reduced bore diameter of the Biograph mMR.

3.3.10. MR Radiofrequency Interference

The RF noise spectra measured on the Biograph mMR are shown in Figure 3.10. No interference could be noticed in the noise spectra.

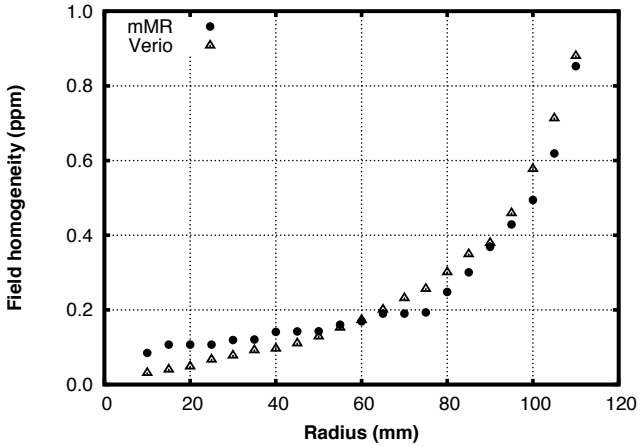

Figure 3.8.: Maximum static field inhomogeneity (in parts per million) in centred sphere, as function of sphere radius.

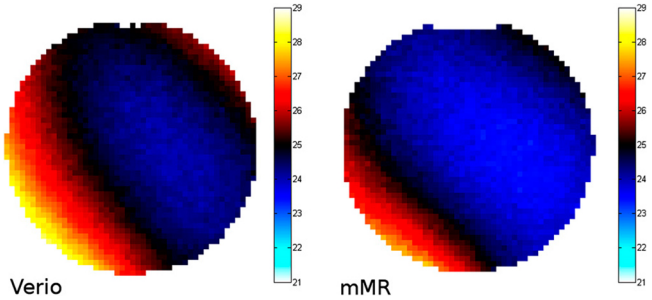

Figure 3.9.: Flip angle maps of an axial slice through the centre of the phantom, reflecting inhomogeneities of the B_1 field of the Verio and the Biograph mMR.

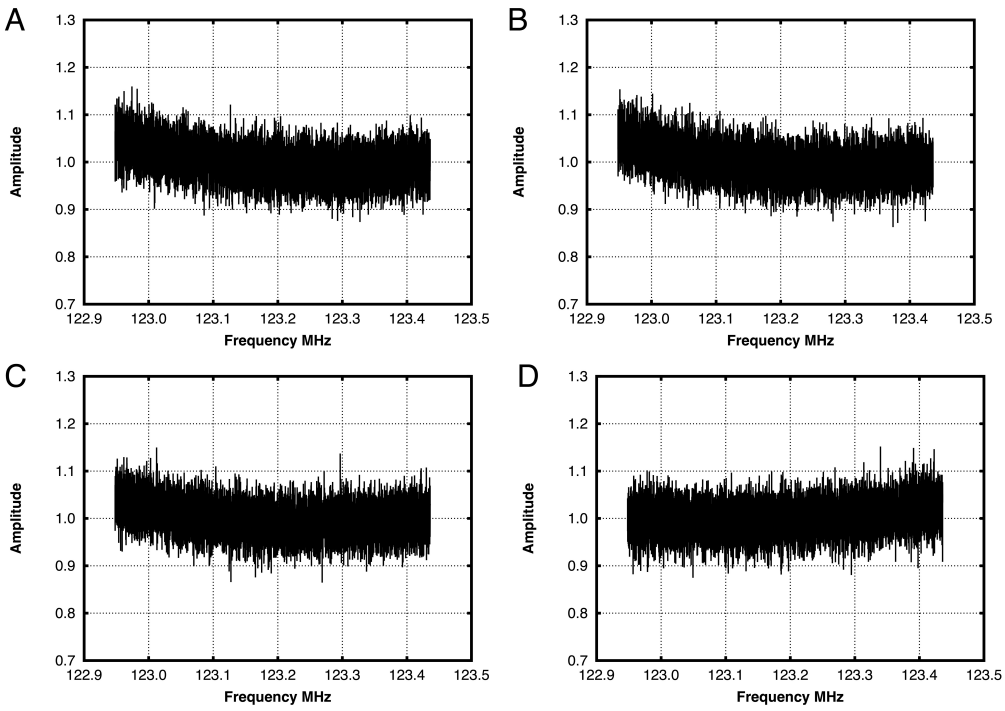

Figure 3.10.: Normalised RF noise spectra: (A) Biograph mMR with the PET electronics powered off. (B) Biograph mMR with the PET electronics powered on. (C) Idem, in the presence of activity. (D) Verio.

The SNRs for the Biograph mMR and the Verio were 50.5 and 53.1, respectively, for the case of gradient-echo sequences and 43.9 and 34.6, respectively, for spin-echo sequences.

3.3.11. In-vivo Studies

The qualitative performance of the Biograph mMR compared with state-of-the art scanners can be appreciated in Figure 3.11.

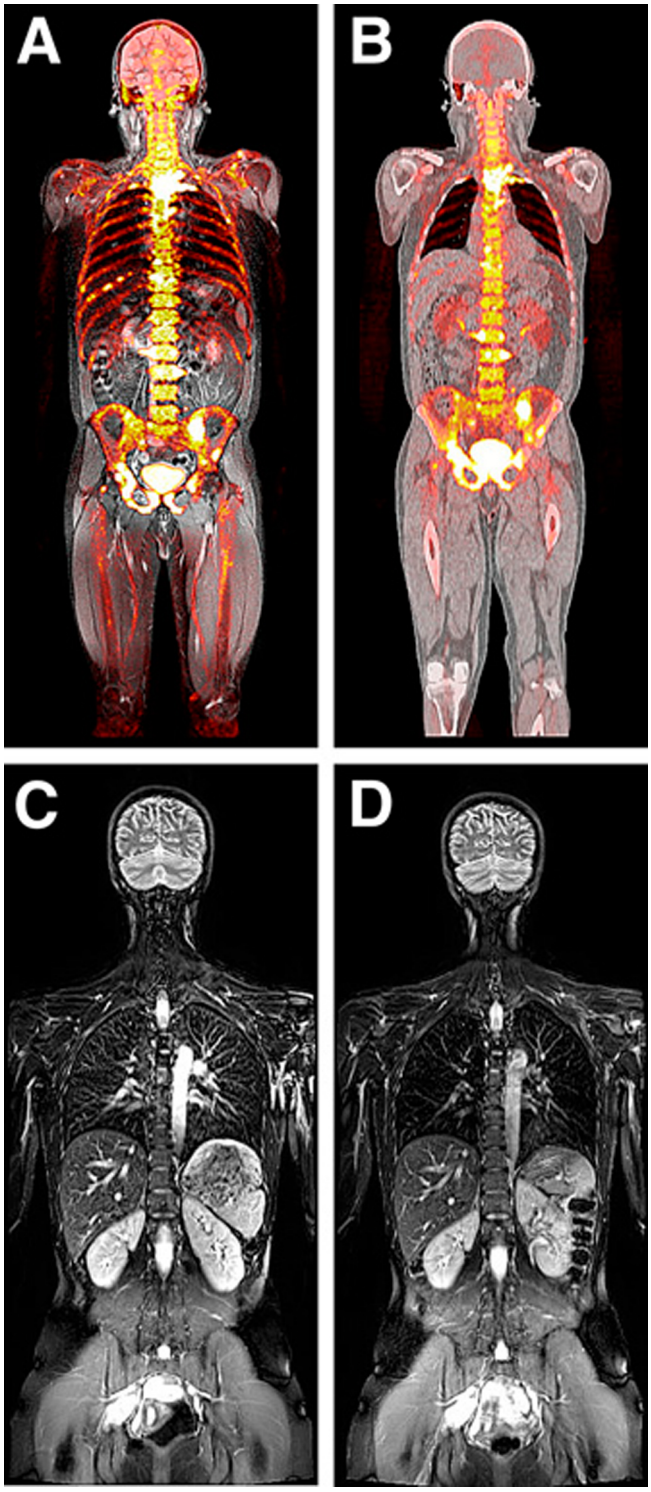

Figure 3.11.: Fused views of a whole-body ^{18}F-fluoride scan of the same patient, acquired with the Biograph mMR PET/MR (A) and the Biograph PET/CT (B). Biograph mMR (C) and Verio (D) T2-weighted coronal views of a healthy volunteer.

Parameter	Distance*	mMR	mCT
Specification			
Axial FOV (cm)		25.8	21.8
Ring diameter (cm)		65.6	84.2
Energy window (keV)		430–610	435–650
Coincidence window (ns)		5.9	4.1
Spatial resolution (mm)			
Transverse, FWHM	1	4.3 (4.3)	4.4 ± 0.1
Transverse, FWTM	1	7.9 (7.9)	8.6 ± 0.1
Axial, FWHM	1	4.3 (4.3)	4.4 ± 0.1
Axial, FWTM	1	8.4 (8.4)	8.7 ± 0.2
Transverse radial, FWHM	10	5.2 (5.2)	5.2 ± 0.0
Transverse radial, FWTM	10	9.7 (9.8)	9.4 ± 0.1
Transverse tangential, FWHM	10	4.8 (4.8)	4.7 ± 0.1
Transverse tangential, FWTM	10	11.9 (11.9)	9.2 ± 0.1
Axial, FWHM	10	6.6 (6.6)	5.9 ± 0.1
Axial, FWTM	10	13.1 (13.1)	10.9 ± 0.3
Sensitivity (kcps/MBq)	0	15.0 (15.0)	9.7 ± 0.2
	10	13.8 (13.8)	9.5 ± 0.1
Peak NEC rate		183.5 kcps;	(180.3 ± 7.8) kcps;
without direct random subtraction		23.1 kBq/mL	(28.3 ± 0.6) kBq/mL
Scatter fraction at clinical activities (%)		36.7	33.2 ± 0.7

Table 3.4.: Comparison of Biograph mMR with Biograph mCT. Values in parentheses refer to measurements with MR influence.
*Radial distance in centimeters from FOV centre.

3.4. Discussion

No significant impact due to the integrated architecture of the Biograph mMR on the performance of either the PET or the MR subsystems was detected with these measurements. Although the MR system offers a wide range of imaging sequences, we focused on morphological MR in the context of whole-body oncologic studies. The performance values obtained in this study compare favourably with PET/CT scanners [59,106]. Table 3.4 summarises these findings, taking as a reference the Siemens Biograph mCT [41], the state-of-the-art PET/CT scanner most closely resembling the mMR.

Concerning the PET subsystem, the measured spatial resolution is typical for scanners with this system geometry and crystal dimensions. The positron range reduction effect of the magnetic field is not significant for ^{18}F at 3 T [80] and would not be perceived unless the point sources were embedded in a dense material. This situation may be different for other isotopes with longer

positron ranges, such as ^{82}Rb or ^{15}O, for which the static field may improve the resolution.

The longer axial FOV and reduced detector ring diameter lead to higher count rates and an increased sensitivity, both in stand-alone operation and with simultaneous MR image acquisition. This also means that the scanner reaches its saturation and dead-time points with lower activities. Work is under way to recalculate the optimal activity doses for each clinical protocol.

An increase in random and scattered counts was expected, because of the higher sensitivity, caused by the reduced ring diameter and the increased axial FOV, and the larger coincidence timing window, required due to the poorer time resolution of APDs with respect to conventional photomultipliers. However, this increase seems to have been compensated by the narrower energy-window settings, which, in combination with a comparable energy resolution, lead to a NEC rate that is better than those of most PET/CT systems and a good scatter fraction.

The image quality and accuracy tests yielded results within the expected range for state-of-the-art scanners. Both procedures had to be performed using calculated μ-maps, because the method to obtain MR-based μ-maps (4.2.3) is optimised for human imaging and not well-suited for phantom studies. The system includes a 2-compartment mode, but this is a solution only for phantoms in which the Dixon sequence yields appropriate images, such as the solid germanium phantom used for the daily quality control procedure. In the case of the NEMA image-quality phantom, dielectric resonance artefacts prevented the use of this method. Future developments will need to include more flexible methods of using various MR sequences or predefined maps for AC.

In summary, the overall performance of the PET sub-system is competitive with state-of-the-art PMT-based systems, showing for the, as to the author's knowledge, first time the great potential of semiconductor-based detectors in clinical whole-body PET. Further work is under way to evaluate those aspects not covered by the NEMA protocol, such as the impact of μ-map truncation.

Concerning the MR subsystem, no significant inhomogeneities were detected in either the static or the RF fields. The operation of the PET detectors inside the MR bore and the transmission of data to the external processing units introduce no visible interferences in the MR operating band. The ACR quality control measurements showed a performance practically identical to that of the Verio.

Further work is required to test the performance of the scanner in a larger area of the FOV. Of particular interest will be the study of inhomogeneities and distortion toward the edges of the FOV and their possible impact on the calculation of MR-based μ-maps.

3.5. Conclusions

The performance of the Biograph mMR whole-body PET/MR scanner was evaluated following the NEMA NU 2-2007 protocol and the ACR quality control manual. The results compare favourably with state-of-the-art PET/CT scanners. This study indicates the successful integration of new detector technology in PET/MR for whole-body imaging. However, further work is necessary to evaluate the more advanced MR applications, such as functional imaging and spectroscopy.

Part III.

Evaluation of Attenuation Correction

4. Attenuation Map Generation in PET/MR: Reproducibility, Effects of MR Contrast Agents and Consequences for Cardiac PET Quantification

4.1. Introduction

PET and MRI are based on fundamentally different physical imaging concepts. Whereas the imaging principle of PET is similar to the one of CT, as it is based on the detection of gamma rays, MRI relies on magnetic fields and the interaction of magnetic moments of typically water protons [53, 57]. This difference and the challenges arising from it are exemplified by the fact that the first clinical PET/CT systems were released in the early 2000s [6], before the arrival of the first combined PET and MR machines, although the development of the latter had been started earlier [87]. However, a paradigm shift is not only required for hardware design in the context of PET/MR, but also for AC.

Owing to the respective imaging modalities, X-ray and MRI CA work differently. Members of the former group, independent of the path of administration (intravascular or gastro-intestinal), alter the attenuation of gamma rays in the patient. Commonly used X-ray CA are iodine-based or barium-containing compounds and have attenuation coefficients substantially higher than that of water. They can influence PET quantification indirectly through CT-based AC [2]. Although both X-rays and the gamma rays detected in PET are affected, the attenuation coefficients of these substances are significantly higher for electromagnetic radiation of up to 140 keV (CT) than for radiation of 511 keV (PET). In MRI, the most widely administered CA are based on Gd. These substances shorten the T1 and T2 relaxation time of protons in water and thus enhance the MR signal, but do not cause significant additional gamma ray attenuation [55]. Instead, they might adversely influence the generation of μ-maps that are used during the reconstruction of quantitative PET images.

Due to the lack of direct physical correlation between the MR signal and

gamma ray attenuation properties of tissue, unprocessed MR information cannot be fed into the PET reconstruction. This makes AC in integrated PET/MR challenging, because there is neither a CT component as in PET/CT nor an external radioactive source as in stand-alone PET. In the case of commercially available PET/MR systems a segmentation-based approach was implemented in which appropriate thresholds and filters facilitate the generation of μ-maps for PET 4.2.3.

A possibly problematic aspect of this approach is fixed segmentation thresholds, which were not optimised for the use with CA. In cardiothoracic imaging, an extended object, the myocardium, is analysed rather than focal points, for example, tumour lesions. The diagnosis is based on the homogeneity of the activity uptake in the myocardium with the uptake in the left ventricle (LV) usually normalised to the maximum voxel value. If fixed segmentation thresholds combined with a tissue-specific MR signal enhancement due to Gd-based CA led to a shift of the relative proportion of tissue classes in the μ-maps, the resulting error of the AC might be different for two different pairs of annihilation photons in absolute values depending on their path (Figure 4.1A). This would lead to a distortion of the activity distribution in the myocardium in the reconstructed PET images and add up to a significant effect on the diagnosis (Figure 4.1B).

In the context of segmentation-based PET/MR AC, other groups have so far concentrated their efforts on other effects on μ-map generation and hence PET quantification, for example, number of tissues classes, variability of attenuation coefficients and general tissue misclassification [44, 58]. The author is aware of only one publication that deals with the effect of CA on PET/MR imaging. However, Lois et al. focussed on the measurement of attenuation coefficients of MR CA and the additional attenuation of the PET signal caused by their application, instead of the consequences of CA-induced artefacts in μ-maps on the quantification of patient PET AC images [55].

The aim of this study was to evaluate the tissue classification reproducibility in μ-maps on the Biograph mMR integrated PET/MR, to assess the effect of MR CA on μ-map generation as well as the impact on PET quantification in patients undergoing cardiothoracic imaging.

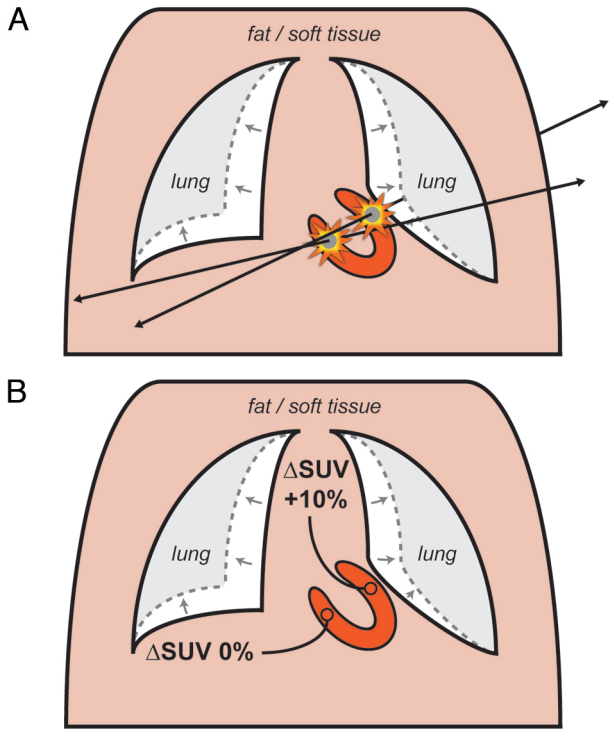

Figure 4.1.: Schematic of a human torso. Due to the administration of CA, structures in the lungs might yield an increased MR signal and could therefore wrongly appear in the segmented μ-map as soft tissue (arrows, dashed lines). (A) Considering two annihilation events: In the first case, the path on which the gamma rays are assumed to travel in opposing directions would go through a region of the μ-map that is incorrectly labelled as soft tissue, whereas the other LOR would not be strongly affected. The attenuation of the former would be overestimated, but the one of the latter might be constant. (B) The apparent growth in the μ-map of tissue with higher attenuation properties might therefore lead to a distortion of the activity distribution in the myocardium in the reconstructed PET images (red) and add up to a significant effect on the diagnosis.

4.2. Materials and Methods

4.2.1. Patient population

All 53 study participants had been referred to the Department of Nuclear Medicine at Klinikum rechts der Isar of Technische Universität München for diagnosis and evaluation of disorders in the thorax with clinical PET/MR. Thirteen of these patients underwent cardiac viability examinations using ^{18}F-FDG. Thirty-five study participants were male and 18 female. Their average age and weight were (60 ± 16) years and (83 ± 16) kg, respectively. Participants were divided into four subgroups. Data of seven out of 53 patients were assessed in terms of classification reproducibility. In 28 of the 53 patients, the effect of CA on classification was studied and in five the response to CA over time. Images of the thirteen cardiac patients were analysed in terms of PET quantification.

Apart from the radiotracer injection, a Gd-based MRI CA (Magnograf 0.5 mmol/mL, Marotrast GmbH, Jena, Germany) was intravenously administered (0.2 mmol/kg). In the case of cardiac patients, this was done for identification of scar tissue using the late Gd enhancement technique [48]. All patients had given informed consent to participate in the study, whereas the study was approved by the institutional review board and the radiation protection authorities.

4.2.2. Acquisition

Instrumentation

All data in this study were acquired on the integrated PET/MR system described in 3.2.1.

Imaging Protocol

For assessment of classification reproducibility, two μ-maps were generated consecutively without CA (μ-map$_{\mathrm{pre}}$) for each patient of that subgroup. To evaluate the effect of CA on classification, a μ-map was acquired (3 ± 1) minutes after CA injection (μ-map$_{\mathrm{post}}$) in addition to a μ-map$_{\mathrm{pre}}$. In the group of patients in which the response to CA was studied over time, a total of 25 μ-maps$_{\mathrm{post}}$ was acquired. In this third group, the time lag between the μ-map scans amounted to (5 ± 3) minutes. All cardiac ^{18}F-FDG patients were administered (348 ± 56) MBq of activity and examined on the PET/MR system on average (128 ± 34) minutes after injection. PET data were then recorded for 15 minutes after μ-map acquisition. Prior to all examinations, the patient's thorax was centred in the FOV of the tomograph. Contrast media was injected using an electronically controlled pump (Spectris Solaris

EP, Medrad Inc., Warrendale, USA). All patients were scanned in the arms-down position.

4.2.3. Processing

Attenuation Correction

For the generation of μ-maps on the Biograph mMR, a dedicated MR scan is performed at each bed position at which PET data are acquired using a 2-point Dixon 3d volumetric interpolated breath-hold T1-weighted sequence. The sequence has a TR of 3.6 ms, a TE_1 of 1.23 ms and its acquisition duration amounts to approximately 19 s. It produces 128 coronal slices with an in-plane resolution of 4.1 $\times$ 2.6 mm^2 and a slice thickness of 3.1 mm. The resulting FOV measures 500 $\times$ 399 mm^2, whereas the flip angle is set to 10.0°. The clinical protocol can either be set up such that the Dixon scan is started at the same time as the PET acquisition or that it is started and finished before the PET start. The Dixon sequence generates two separate sets of images, one with water and fat signals in phase and one with water and fat signals out of phase [23]. As outlined in [17], the signal for any image pixel is given by

$$S_k = W + Fe^{ik\pi}(k = 0, 1), \tag{4.1}$$

where W denotes the water signal and F the fat signal. By adding or subtracting the two complex signals, images containing only the water or the fat signals can be obtained:

$$2W = S_0 + S_1 \tag{4.2}$$

$$2F = S_0 - S_1 \tag{4.3}$$

μ-maps are created by segmenting these images into four tissue classes, that is, air, lung, fat and soft tissue, and assigning predefined attenuation coefficients to the corresponding voxels, that is, 0.0000 cm^{-1}, 0.0224 cm^{-1}, 0.0854 cm^{-1} and 0.1000 cm^{-1}, respectively [61]. Hardware μ-maps of the static head, neck and spine coils as well as the patient table had been created by the manufacturer by means of CT acquisition and are automatically added prior to the PET image reconstruction, because they do not yield signals detectable with the Dixon sequence. Flexible MR surface coils are neglected [20,24]. The resulting μ-maps are furthermore employed for 3d scatter correction by single-scatter simulation [101].

PET Image Reconstruction

For each of the thirteen cardiac patients, two sets of images were reconstructed from PET raw data using the μ-map_{pre} and the μ-map_{post}. Prior to reconstruction, the μ-maps were registered to each other using clinical analysis

software (TrueD, Siemens Healthcare, Erlangen, Germany) in order to guarantee optimal consistency of emission and attenuation data. Then, an OSEM 3d algorithm was applied with 3 iterations and 21 subsets, following the clinical standard in the Department of Nuclear Medicine at Klinikum rechts der Isar of Technische Universität München [24]. The chosen matrix was set to a size of 344 × 344, and the post-reconstruction filter was a Gaussian with a kernel of 5.0 mm. Data were also normalised and corrected for dead time, attenuation, scatter, decay, frame length and randoms.

4.2.4. Analysis

Attenuation Maps

All μ-maps were visually checked for wrong assignment of lung tissue as air, misclassifications and erroneous segmentation. Then, a pixel-based analysis was performed by histogramming the image data of the μ-maps. Thus, their composition could be determined regarding the volumes of lung, fat and soft tissue. The seven pairs of $\mu\text{-maps}_{\text{pre}}$ were analysed to test the classification reproducibility. The effect of CA on classification was assessed in the 28 patients with both $\mu\text{-map}_{\text{pre}}$ and $\mu\text{-map}_{\text{post}}$. A two-sided paired t-test was performed to assess the statistical significance of the change in apparent tissue volume. In the 25 consecutively acquired $\mu\text{-maps}_{\text{post}}$, the response to CA was studied over time.

PET Image Quantification

The effect of CA-induced μ-map artefacts on cardiac PET quantification was assessed in terms of apparent uptake differences between the reference, that is, images reconstructed with the $\mu\text{-map}_{\text{pre}}$, and the images reconstructed with the $\mu\text{-map}_{\text{post}}$. Global and local myocardial uptake in the LV was volumetrically quantified according to the 17-segment model of the American Heart Association [13], using software developed in-house [67]. As measure, the mean standardised uptake value (SUV_{mean}) was chosen. Since only uptake variations between different sets of images reconstructed from the same raw data were compared, the SUV_{mean} is equivalent in this context to the activity concentration.

Figure 4.2.: Example μ-maps of the same patient, acquired before (A) and after (B) administration of CA.

4.3. Results

4.3.1. Attenuation Maps

Classification Reproducibility

The apparent volumes in the two consecutive μ-maps$_{\text{pre}}$ differed by (-5 ± 9)%, (0 ± 1)% and (0 ± 2)% on average for lung, fat and soft tissue.

Effect of Contrast Agents on Classification

Due to the injection of CA, morphological structures appear in the μ-maps in the vicinity of the location of the trachea and the primary bronchi (Figure 4.2). Before CA administration, (10 ± 3)% of the non-background voxels were classified as lung tissue, (26 ± 8)% as fat and (56 ± 8)% as soft tissue. A proportion of (9 ± 1)% of the voxels was ambiguous. Therefore, the mean of the fat and soft tissue attenuation coefficients, that is, 0.0927 cm^{-1}, was assigned to them by the algorithm. After CA administration, these proportions had changed to (8 ± 3)% for lung tissue, to (17 ± 9)% for fat and to

	Lung	Fat	Fat/Water	Soft Tissue
μ (cm^{-1})	0.0224	0.0854	0.0927	0.1000
μ-map tissue ratio (pre-CA)	(10 ± 3)%	(26 ± 8)%	(9 ± 1)%	(56 ± 8)%
μ-map tissue ratio (post-CA)	(8 ± 3)%	(17 ± 9)%	(9 ± 2)%	(66 ± 8)%
Volume Change	(-12 ± 23)%	(-39 ± 15)%	(+6 ± 18)%	(17 ± 8)%
p-value	0.005	0.000	0.042	0.000

Table 4.1.: The μ-map compositions before and after administration of CA and the volume changes of the respective tissue classes. The linear attenuation coefficients (μ) at 511 keV are given as well. Pre-CA denotes the situation before and post-CA the one after the administration of CA.

(66 ± 8)% for soft tissue. The ratio of ambiguous voxels changed to (9 ± 2)%. This means that the apparent volume of lung tissue in the μ-maps decreased by on average (-12 ± 23)% (p = 0.01). The apparent volume of fat decreased as well, that is, by (-39 ± 15)% (p = 0.00), whereas the amount of soft tissue grew by (+17 ± 8)% (p = 0.00). The volume of the above mentioned ambiguous voxels was (+6 ± 18)% larger (p = 0.08) with CA (Table 4.1).

Response to Contrast Agents over Time

Less than 10 minutes after the injection of CA, the apparent volume of, for example, soft tissue in the μ-maps was on average (+17 ± 6)% higher than in the last μ-map$_{\text{pre}}$ and remained almost constant at this level for the investigated range of delays (Figure 4.3).

4.3.2. PET Image Quantification

Global SUV Changes due to Contrast Agents

By replacing in the image reconstruction the μ-map$_{\text{pre}}$ with the μ-map$_{\text{post}}$, the global SUV_{mean} in the LV increased on average (+7.1 ± 7.4)% for all patients. The individual SUV_{mean} changes ranged between -1.7% and +26.7% (Figure 4.4A).

Local SUV Changes due to Contrast Agents

As examples the following segments were chosen:

- **basal-inferior** – with one of the lowest average SUV_{mean} changes and the lowest standard deviation
- **basal-anterolateral** – with the highest average SUV_{mean} change and the highest standard deviation

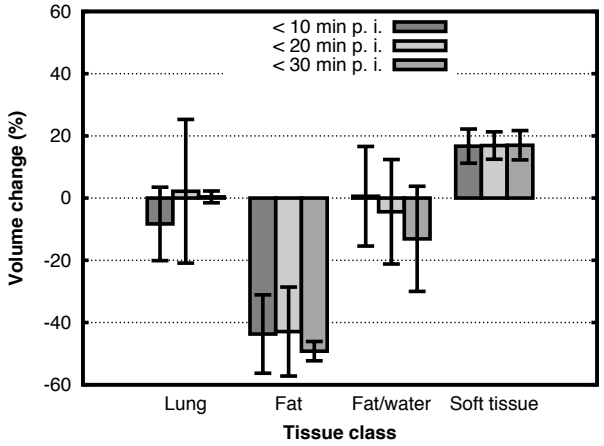

Figure 4.3.: Tissue volume changes in μ-maps in three time frames after administration of CA relative to the corresponding μ-map$_{\mathrm{pre}}$ (number of included μ-maps: <10 min, 9; <20 min, 11; <30 min, 5). For the investigated range of delays, the tissue proportions before were not recovered after the administration of CA.

- **apical-septal** – with the lowest average $\mathrm{SUV}_{\mathrm{mean}}$ change and one of the largest differences between maximum and minimum $\mathrm{SUV}_{\mathrm{mean}}$ change

More detailed information and quantitative information on other segments can be obtained from Table Table 4.2.

The local $\mathrm{SUV}_{\mathrm{mean}}$ changes due to the μ-map affected by the injection of CA were between -1.4% and +8.6% in the basal-inferior segment, between -12.1% and +58.5% in the basal-anterolateral segment and between -17.9% and +32.9% in the apical-septal segment (Figure 4.4B). The average $\mathrm{SUV}_{\mathrm{mean}}$ changes in these three segments were (+4.4 ± 3.6)%, (+15.6 ± 21.1)% and (+2.8 ± 11.2)%, respectively. Overall, an effect of more than 10% due to artefact-exhibiting μ-maps could be observed in 25.3% of the investigated voxels in the polar maps, that is, in 56 out of 221 voxels.

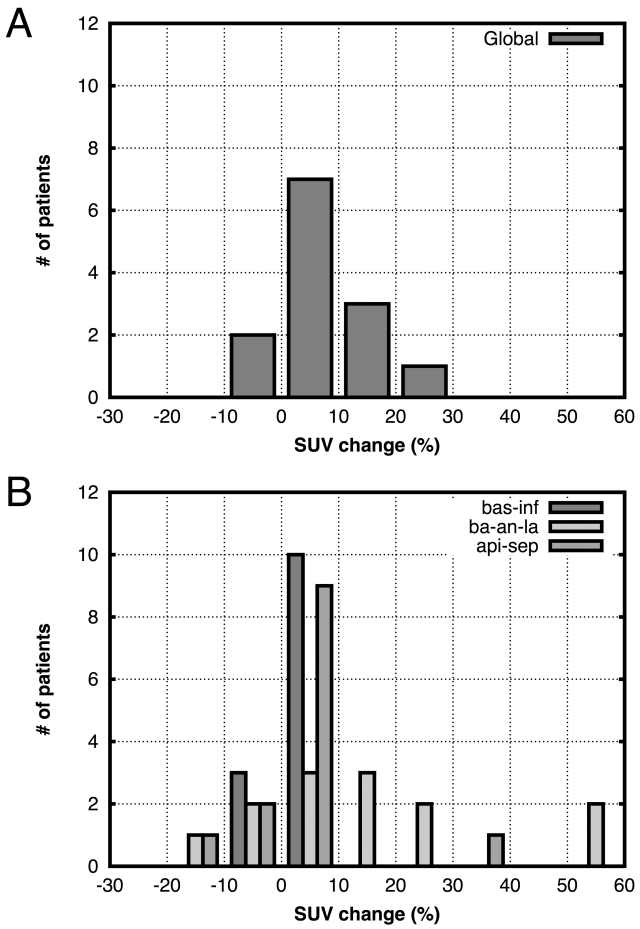

Figure 4.4.: The distribution of the global (A) and local (B) SUV_{mean} changes in the LV. For visualisation of the local effect, the basal-inferior (bas-inf), basal-anterolateral (bas-an-la) and the apical-septal (api-sep) segments were chosen.

Segment	ΔSUV_{mean} (%)				# of Patients with	
	Avg.	Min.	Max.	Max. – Min.	Effect > 10%	ΔSUV_{mean} > Global Ø
Basal anterior	12.3 ± 14.1	-9.2	39.5	48.7	5	9
Basal anteroseptal	6.1 ± 7.6	-9.5	24.3	33.9	2	5
Basal inferoseptal	4.9 ± 7.3	-9.6	23.3	32.9	1	4
Basal inferior	4.4 ± 3.6	-1.4	8.6	10.1	0	4
Basal inferolateral	8.2 ± 10.1	-14.0	22.7	36.6	6	8
Basal anterolateral	15.6 ± 21.1	-12.1	58.5	70.7	8	9
Mid anterior	8.4 ± 11.8	-7.5	36.5	44.0	3	6
Mid anteroseptal	4.0 ± 10.4	-17.5	31.1	48.7	2	2
Mid inferoseptal	4.5 ± 8.2	-10.3	26.8	37.1	2	2
Mid inferior	4.9 ± 6.3	-3.1	21.2	24.2	2	4
Mid inferolateral	6.2 ± 9.2	-14.1	21.1	35.2	5	4
Mid anterolateral	13.2 ± 15.6	-6.8	45.0	51.8	6	7
Apical anterior	4.5 ± 11.2	-18.3	32.2	50.4	2	4
Apical septal	2.8 ± 11.2	-17.9	32.9	50.7	2	3
Apical inferior	5.6 ± 10.1	-6.7	28.9	35.5	2	4
Apical lateral	7.7 ± 9.0	-8.6	25.0	33.6	5	7
Apex	5.1 ± 10.7	-6.8	34.4	41.1	3	4

Table 4.2.: The local SUV_{mean} changes in the 17 segments of the LV.

4.4. Discussion

The differences between μ-maps obtained in two consecutive scans of the same patients are small and the composition of μ-maps without CA injected before acquisition is very similar over all patients. These two findings highlight the general stability of the segmentation-based approach to generate μ-maps. The higher variability in the apparent volume of lung tissue without CA could be attributed to the respective respiratory states. According to the clinical protocol in the Department of Nuclear Medicine at Klinikum rechts der Isar of Technische Universität München, μ-maps are acquired in expiration and patients given breathing commands. However, the exact level of expiration is never identical. Deviation from the mean proportions of lung, fat and soft tissue is higher for fat and soft tissue, where patients naturally differ from each other most.

Administration of CA prior to the μ-map acquisition has obvious visual and also quantifiable effects. Both the number of voxels classified as lung tissue as well as the number of those classified as fat decreased significantly in favour of soft-tissue voxels, which is a direct result of the CA properties. Gd-based CA shorten the T1 and T2 relaxation times of protons in water for the used MR sequences, thus enhancing the water, but not the fat signal. Moreover, higher standard deviations point to a more patient-dependent response. It could be shown that the delay between CA injection and μ-map acquisition does not play a role for the extent and characteristic of this effect during a routine cardiac PET/MR study.

Lois et al. concluded from their data, that is, one patient μ-map, that μ-maps would not be biased after administration of Gd-based MR CA, if segmentation-based algorithms were used [55]. However, the results of a quantitative analysis of the μ-map composition were not reported. Although the shown μ-map slices before and after administration of CA are inconsistent, slight differences in the segmentation, for example, in terms of fat and soft-tissue proportions are visible. Without information about, for example, the weight of the patient investigated by Lois et al., it is not possible to explain the apparent contradictory findings, which could potentially be due to differing CA concentrations in the patients.

Soft tissue is the tissue class with the highest attenuation coefficient in the μ-map of the Biograph mMR. The increase of the number of corresponding voxels in the μ-map of approximately +17% might lead to the assumption that its effect on PET quantification is similarly drastic. In this light, the global SUV_{mean} change in the LV of less than 10% on average appears to be rather small. With only this information, one might even argue over the significance of the effect. However, the reported minimum and maximum SUV_{mean} changes mirror the variability found in the μ-maps.

A closer look at the individual segments of the myocardium revealed that the effect does not manifest itself in a homogeneous fashion, as shown in

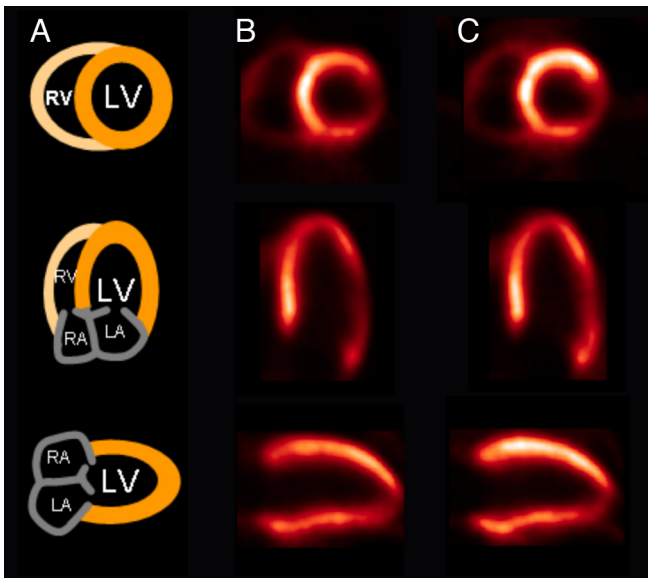

Figure 4.5.: (A) Schematic representations of the short-axis, horizontal- and vertical-long-axis slices of the LV, (B) the respective slices of the LV of patient 5 before and (C) after the administration of CA. The inhomogeneity of the effect can be seen in each of the slices.

Figure 4.5. In five out of 17 segments, the absolute values of the average SUV_{mean} changes were found to be above 10%. In 12 out of the same 17 segments, the average SUV_{mean} changes were higher than the global average of +7.1%. Local standard deviations were larger as well. In only three out of the 17 segments, they were smaller than the global standard deviation of 7.4%.

The following examples demonstrate that the effect of CA on μ-maps can make a difference for the diagnosis, if these μ-maps are used for the reconstruction of PET images (Figure 4.6 and Figure 4.7). According to the clinical infarct protocol in effect at the Department of Nuclear Medicine at Klinikum rechts der Isar of Technische Universität München, cardiac tissue with an ^{18}F-FDG uptake of less than 50% of the maximum is considered affected by an infarct [84]. As shown by the polar maps of patient 4, this applies to 42% of the image segments, if reconstructed with a μ-map_{pre} (Figure 4.7A). In the images reconstructed using the corresponding μ-map_{post} (Figure 4.7B), the proportion of such voxels is at 67%, which amounts to an increase of approximately +60%.

In contrast to iodine-based CA, which accumulate in the vascular system, Gd-containing CA are distributed more evenly in the human body. Therefore, artefacts as discussed by Antoch et al. [2] are found more locally in or near the vessels, whereas errors due to MR CA can arise more globally and to a greater extent in regions, where the proportion of water in the tissue is higher. This means that the manifestation of the effect of CA in PET/CT is focal

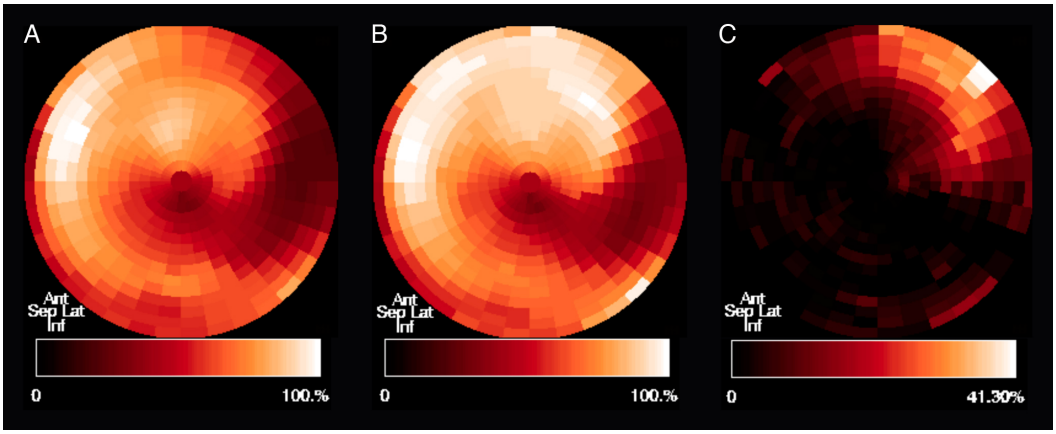

Figure 4.6.: Polar maps of the activity uptake in the LV of patient 5 before (A) and after (B) administration of CA. The subtraction of both is shown as well (C).

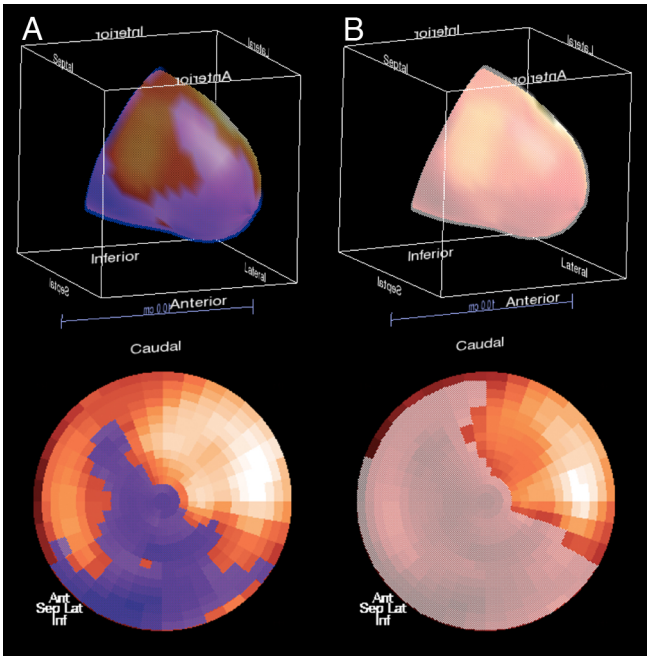

Figure 4.7.: 3d representations and polar maps of the activity uptake in the LV of patient 4 before (A) and after (B) administration of CA. Based on a 50% threshold, 42% (A) and 67% (B) of the image segments are affected by an infarct.

and lower, but in PET/MR tissue-selective and potentially substantial.

The main limitation encountered in this study was the complexity of the clinical protocol, which imposes strict constraints and does not allow the acquisition of μ-maps at an arbitrary time point. In addition, the variability of the exact respiratory state was found to be higher than expected despite breathing commands.

4.5. Conclusions

The current method of μ-map generation in integrated PET/MR was found to be reproducible and stable in the absence of CA. CA lead to significant over-weighting in the μ-maps of tissues with higher attenuation coefficients, artificially increasing the SUV in PET images. Tissue misclassification is independent of the investigated range of delays after CA injection. The global effect on the myocardial uptake was mostly in the order of statistical fluctuations, but its extent varied considerably among the patients studied. It is more substantial and variable locally in the myocardial segments, not only complicating inter-patient comparability, but also possibly resulting in inaccurate readings and wrong diagnoses. Therefore, μ-maps should either be acquired before the administration of CA or CA-optimised segmentation parameters be implemented.

5. Impact of Flexible Body Surface Coil and Patient Table on PET Quantification and Image Quality in Integrated PET/MR

Based on the work published in Nuklearmedizin (S. Fürst et al., Nuklearmedizin 2014; 53: 79–87)

5.1. Introduction

PET and MRI are based on fundamentally different imaging principles. In PET, the spatial distribution of a positron-emitting radiopharmaceutical administered to the patient is measured by detecting the coincidence of the two annihilation photons. MRI, on the other hand, relies on magnetic fields and RF pulses for image generation. The RF transmission and reception is performed with dedicated coils, which were optimised over the last decades. The coils required for proper imaging of the spine and the posterior region of the body and other electronics are typically embedded into the patient table, which is in general more solid than those of scanners combining PET and CT.

In integrated PET/MR, this hardware results in additional attenuating and scattering material in the FOV of the PET detectors. Including the coils in the process of AC is not always straightforward, because it requires precise information about the attenuating properties of their components and exact knowledge about their positioning. Previous work on this subject focussed on the assessment of the effect of a head coil, optimisation of its design and the creation of a CT-based μ-map [20]. In the case of the current Biograph mMR (3.2.1), the positioning of the whole-body surface coils on the patient is rather unrestricted, that is, their exact location remains unknown to the system, which is why they are not included in AC. In contrast, CT-based μ-map templates of the patient table and the spine coils, the location of which is known at any time in the scan, are stored on the system and automatically

added to the patient μ-map prior to PET image reconstruction.

Previous studies on the interaction between MR equipment and PET can be divided into two groups, evaluating the effects of MR equipment on PET data on the one hand [20,56,92] and focusing on correction schemes and the assessment of their outcomes on the other hand [70, 109]. The measurements were performed on PET-only [20, 56, 92], PET/CT [20, 56] and different types of PET/MR scanners [70, 92, 109]. The equipment under investigation included a patient table [109], head coils [20,56,92,109] and surface coils [56,70,92,109], manufactured by the three major companies in the field. The effects were studied using phantoms, that is, cylindrical and NEMA image quality phantoms. Only Paulus et al. [70] used the Biograph mMR and also scanned a single patient with PET-optimised surface coils.

The goal of this study was to assess the effect of flexible MRI surface coils used in thoracic and abdominal imaging and the patient table of an integrated PET/MR scanner on PET quantification and count statistics, image quality and scan time. This was done with phantoms in a controlled environment. A patient study was conducted to further investigate the clinical relevance of the effect.

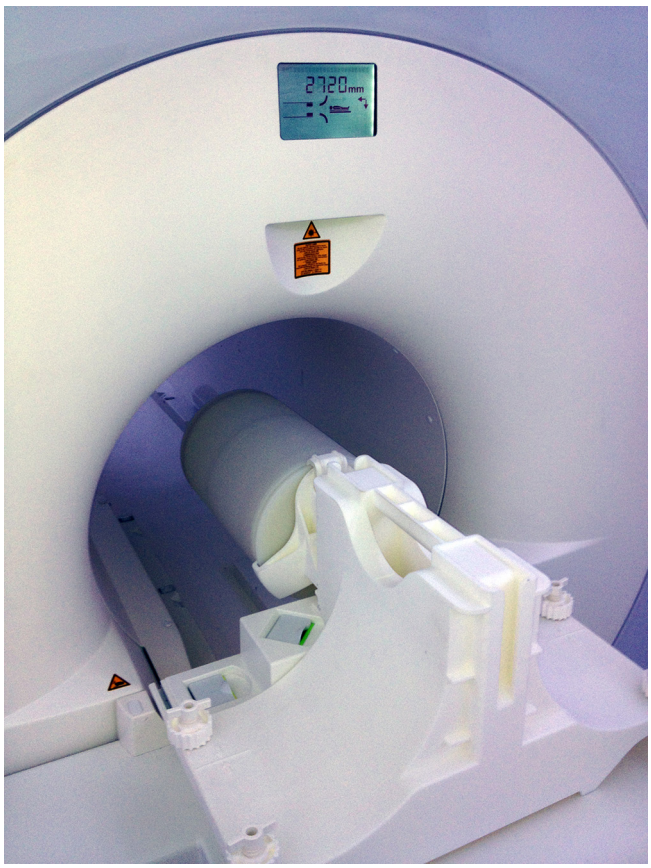

Figure 5.1.: The cylindrical fillable phantom used for the assessment of the patient table, shown here in the bore of the Biograph mMR.

5.2. Materials and Methods – Phantom Study

The effects of surface coils and patient table were first evaluated using phantoms.

5.2.1. Phantom Design

For the assessment of the patient table, a cylindrical fillable standard phantom (Figure 5.1) with an outer diameter of 21.27 cm, an inner diameter of 20.00 cm, a wall thickness of 6.35 mm an inner length of 30.08 cm and a volume of 9.451 l) was used. The linear attenuation coefficient of the wall material was specified as 0.120 cm^{-1}.

For the investigation of the surface coil, the phantom was based on a plastic bottle (transverse diameter: 18 cm, conjugate diameter: 14 cm, height: 33 cm) with thin walls, adding negligible gamma-ray attenuation (Figure 5.2A). As a lesion, an Eppendorf tube (0.25 mL) was positioned in the middle section of the bottle and near its wall using a rod structure (Figure 5.2B).

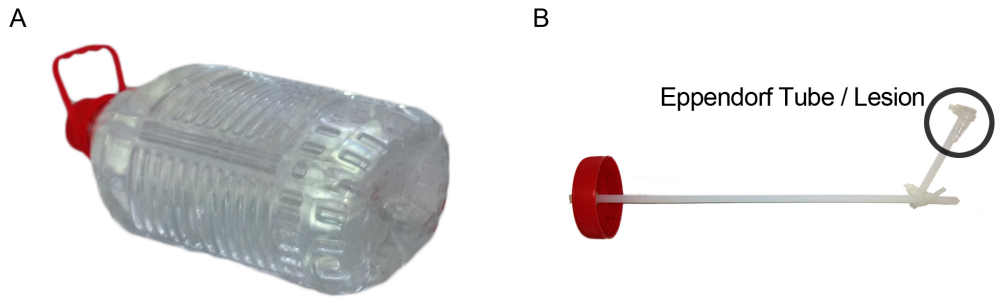

Figure 5.2.: The phantom used in this study for the investigation of the surface coil was based on a thin-walled bottle with a capacity of 5100 mL (A). An Eppendorf tube attached to the bottle cap using a plastic rod served as a lesion (B).

Figure 5.3.: Body matrix coil of the Biograph mMR.

5.2.2. Acquisition

Instrumentation

All data in this study were acquired on the integrated PET/MR system, described in 3.2.1. For comparison of table attenuation and image quality, the cylindrical phantom was additionally scanned on a PET/CT tomograph (Biograph mCT, Siemens Medical Solutions, Knoxville, USA). The PET sensitivity of the latter system was reported to be 9.7 kcps/MBq [41], whereas the sensitivity of the Biograph mMR was 15.0 kcps/MBq as presented in 3.3.1.

The surface coil under investigation was the standard 6-element Body Matrix Coil (Siemens Healthcare, Erlangen, Germany) that is shipped with the Biograph mMR (Figure 5.3). Its elements are arranged in two clusters, with a total of six integrated preamplifiers incorporated into the coil as well. It was optimised for the use with PET and is not only flexible in terms of material,

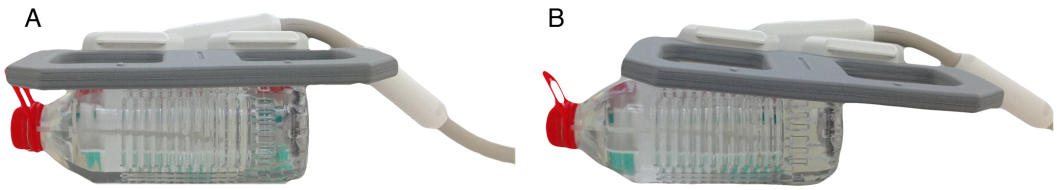

Figure 5.4.: The effect of the surface coil on the phantom was studied for two coil positions, centred on the phantom (A) and shifted by 5 cm towards the foot end of the patient table (B).

but can also be placed at any position along the patient bed.

Imaging Protocol

The cylindrical phantom was filled with an aqueous solution of ^{18}F-FDG, fixed to the head of the patient bed using the quality assurance phantom holder that was shipped with the respective scanner and then centred in the FOV. Depending on the orientation of the holder, the phantom was either located in the FOV together with the table or it extended into the FOV without the table underneath. PET data were acquired for 10 minutes first with and then without the bed. The first scan was started, as soon as the activity inside the phantom had decayed to 50 MBq, and the second scan 15 minutes after the first.

Prior to the scan with surface coil, the bottle phantom was filled with an ^{18}F-FDG solution as well. The filled volume amounted to 5100 mL, containing a total background activity of 40 MBq. The lesion was filled with 9500 Bq or 0.0095 MBq. A volume of 30 mL of a clinical Gd-based CA (Magnograf 0.5 mmol/mL, Marotrast GmbH, Jena, Germany) was added for the reduction of resonance effects associated with MRI, which could lead to artefacts in the μ-map. Four PET scans with a duration of 15 minutes and a delay between the scans of 5 minutes each were performed approximately 100 minutes after activity measurement:

1. Without surface coil,
2. with a coil centred on the phantom (Figure 5.4A),
3. with the same coil moved by 5 cm (Figure 5.4B),
4. without coil.

The fourth measurement was performed to ensure reproducibility of the first. Before the scans, the phantom had been placed on the patient table, aligned with the main axis of the scanner, and then centred in its FOV. When the coil was attached, repositioned or removed, special care was taken that the phantom did not move relative to the patient table.

5.2.3. Processing

Attenuation Correction

For the generation of μ-maps, the method described in 4.2.3 was followed in this study.

PET Image Reconstruction

Images were reconstructed from PET raw data acquired with the Biograph mMR according to the clinical standard in the Department of Nuclear Medicine at Klinikum rechts der Isar of Technische Universität München, that is, using an OSEM 3d algorithm with 3 iterations and 21 subsets, a 172 × 172 image matrix and a 4.0 mm Gaussian post-reconstruction filter [24]. Data were also normalised and corrected for dead time, attenuation, scatter, decay, frame length and randoms.

For the evaluation of the patient table, this was done for ten different frame lengths between 1 and 10 minutes. To ensure consistency with the Biograph mCT, a μ-map of the cylindrical phantom was manually created for the use with the Biograph mMR. Since the user interface of the reconstruction software of the Biograph mCT does not allow the same combination of iterations and subsets, three sets of images with 4 iterations and 8 subsets, 5 iterations and 12 subsets and with 3 iterations and 24 subsets were reconstructed from the raw data acquired with the Biograph mCT.

For the investigation of the surface coil, the best of the acquired μ-maps in terms of consistency with the actual shape of the bottle phantom was used for reconstruction of all raw data in order not to introduce quantification errors due to slight discrepancies in the μ-maps.

5.2.4. Analysis

Image noise was expressed as relative standard deviation in a large cubic volume of interest (VOI), centred in the cylindrical phantom. In the case of the Biograph mCT, 2nd order polynomials defined by the corresponding data points of image noise as a function of the number of effective iterations[1] yielded noise estimates matching the Biograph mMR reconstruction parameters of 3 iterations and 21 subsets. To derive implications of the patient table of the Biograph mMR for scan duration, an exponential function was fitted to the noise function of the Biograph mMR and its intersection with a specific noise level of the Biograph mCT determined.

For the measurements with surface coil, a VOI was created around the lesion in all four image sets. The threshold was set to a level of 75% of the maximum, accounting for the noise level in conjunction with the small size of

[1] The number of effective iterations is defined as the product of the number of iterations and the number of subsets [82].

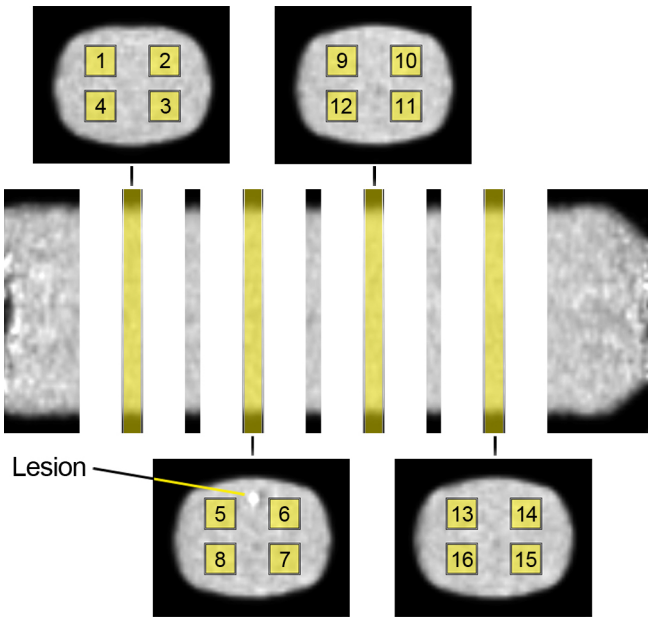

Figure 5.5.: Locations of the analysed VOIs in the phantom.

the lesion. In the background, four sets of four rectangular VOIs were drawn at different positions along the main axis through the phantom as displayed in Figure 5.5. VOIs 1 to 4 were centred on transaxial slice 35 (position 1), VOIs 5 to 8 on slice 50 (position 2), VOIs 9 to 12 on slice 65 (position 3) and VOIs 13 to 16 on slice 80 (position 4). SUV_{mean} in the VOIs and corresponding standard deviations were then compared.

For both series of measurements, the numbers of trues and prompts were derived directly from the sinograms and corrected for radioactive decay. The difference between these numbers in the two settings is a direct global measure for the additional attenuation introduced by the hardware.

Patient	Sex	Age	Diagnosis	Lesion Locations			No. of Lesions
				post.	cent.	ant.	
1	f	47	Melanoma	-	-	-	0
2	f	44	Breast cancer	2	1	1	4
3	m	55	Melanoma	-	-	-	0
4	f	61	Lymphoma	-	2	-	2
5	f	50	Lymphoma	-	-	-	0
6	m	59	Melanoma	1	2	2	5
7	m	64	Bronchial carcinoma	-	4	-	4
8	f	70	Breast cancer	3	-	2	5
9	f	48	Breast cancer	-	1	-	1
10	f	57	Fallopian tube carcinoma	-	4	-	4
11	f	55	Breast cancer	1	3	1	5

Table 5.1.: List of patients included in this study (f, female; m, male). The lesions were divided into three groups, that is, anterior (ant.), central (cent.) and posterior (post.) lesions.

5.3. Materials and Methods – In-vivo Study

Patient studies were conducted on the Biograph mMR to further investigate the clinical relevance of the effect of surface coils.

5.3.1. Patient population

All study participants (Table 5.1) had been referred to the Department of Nuclear Medicine at Klinikum rechts der Isar of Technische Universität München for diagnosis and staging of malignant disorders using ^{18}F-FDG PET/CT. Of the total of 11 patients included in the study, three were male and eight female. Their average age and weight were (55 ± 8) years and (72 ± 14) kg, respectively.

All patients had given informed consent to undergo a second examination on the integrated PET/MR system subsequent to the clinically required PET/CT. For the Biograph mMR scan no additional radiotracer was administered. The institutional review board and the radiation protection authorities had approved the study.

5.3.2. Acquisition

Imaging Protocol

All patients were administered (378 ± 40) MBq of ^{18}F-FDG and examined on the PET/MR system described in 3.2.1 on average (144 ± 20) minutes after injection. PET data were acquired for 4 minutes, first with and then without

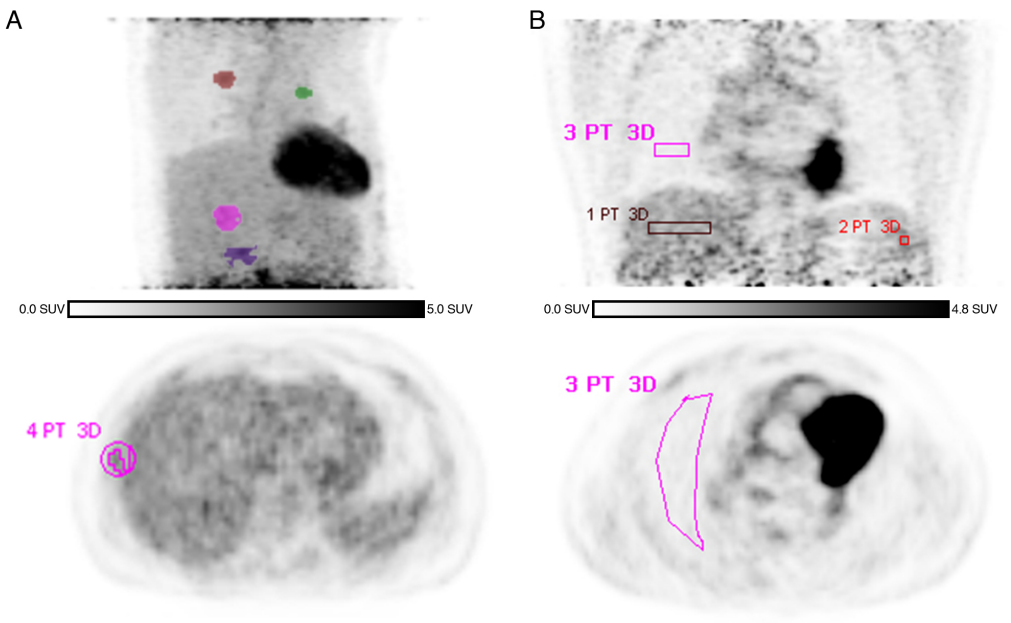

Figure 5.6.: Examples of the analysed VOIs around a lesion (A) and in transaxial slices through the organs (B).

the surface coil placed on the patient's thorax and abdomen, and this region centred in the FOV of the tomograph at the exact same position. The time delay between the starts of the two scans amounted to (6.9 ± 0.6) minutes on average, ranging from 6.4 minutes to 8.4 minutes, while care was taken that patient movement relative to the bed was minimal during coil removal between the two scans. All patients were scanned with their arms up.

5.3.3. Processing

In the patient studies, the μ-map acquired at the beginning of the PET scan was always used for the reconstruction of the respective raw data. Apart from this, AC and image reconstruction were performed as outlined in 5.2.3 for the phantom study.

5.3.4. Analysis

In the patient studies, the effect of surface coils was assessed by SUV determination in suspected tumour lesions and organs, for which the lung, liver and spleen were selected as examples. For this purpose, PET images obtained with and without coil were co-registered using clinical analysis software (TrueD, Siemens Healthcare, Erlangen, Germany), the results of which were visually verified. In a second step, isocontour VOIs (>50% of the maximum) were created for the lesions in both image sets (Figure 5.6A) and SUV_{mean}, standard

deviation and total size calculated. Additionally, SUV_{max} was determined in lesions. In order to obtain transaxial and coronal VOIs in the organs, ROIs were drawn in one transaxial or coronal slice and then copied to three to five subsequent transaxial or coronal slices accordingly, yielding the above-mentioned parameters as well. For this purpose, the shape of the organ was delineated as best as possible under the condition of avoiding edge voxels in any of the four to six consecutive slices (Figure 5.6B). Information on trues and prompts was also gathered from the sinograms and corrected for decay.

Location	VOIs	ΔSUV_{mean}	
		P1	P2
Posterior	3, 4, 7, 8, 11, 12, 15, 16	6%	5%
Anterior	1, 2, 5, 6, 9, 10, 13, 14	9%	6%
Transaxial position 1	1, 2, 3, 4	8%	7%
Transaxial position 2	5, 6, 7, 8	8%	6%
Transaxial position 3	9, 10, 11, 12	7%	5%
Transaxial position 4	13, 14, 15, 16	6%	4%
Lesion	Lesion	16%	12%

Table 5.2.: Average SUV changes due to coil removal at different locations in the phantom for coil position 1 (P1), that is, comparing scans 1 and 2, and for coil position 2 (P2), that is, comparing scans 1 and 3.

5.4. Results – Phantom Study

5.4.1. Image Noise and Scan Time

Image noise of the Biograph mCT with bed for different scan durations and effective numbers of iterations is shown in Figure 5.7A. For a scan duration of 3 minutes, the noise level of the Biograph mCT is at 9.5%, that of the Biograph mMR at 11.1% with bed and at 10.2% without (Figure 5.7B). To achieve the noise level of the Biograph mCT for a scan duration of 3 minutes, the phantom had to be scanned for almost 4 minutes on the Biograph mMR according to the approximation described in 5.2.3 (Figure 5.7C).

5.4.2. SUVs

Coil Position 1 and 2

The results of the phantom study for coil positions 1 and 2 are listed in Table 5.2. Difference images reflecting these results are presented in Figure 5.8.

Repeatability

To ensure reproducibility, the 1^{st} and 4^{th} scan of the phantom study were compared. Between these two measurements without a coil attached to the phantom, the SUV_{mean} did not change in neither of the background VOIs. In the lesion, the SUV_{mean} was 3% higher in the 4^{th} scan relative to the 1^{st} scan.

5.4.3. Counts

The patient table of the Biograph mMR accounts for a loss of 18.7% of true events, compared to a reduction of 11.0% for the table of the Biograph mCT.

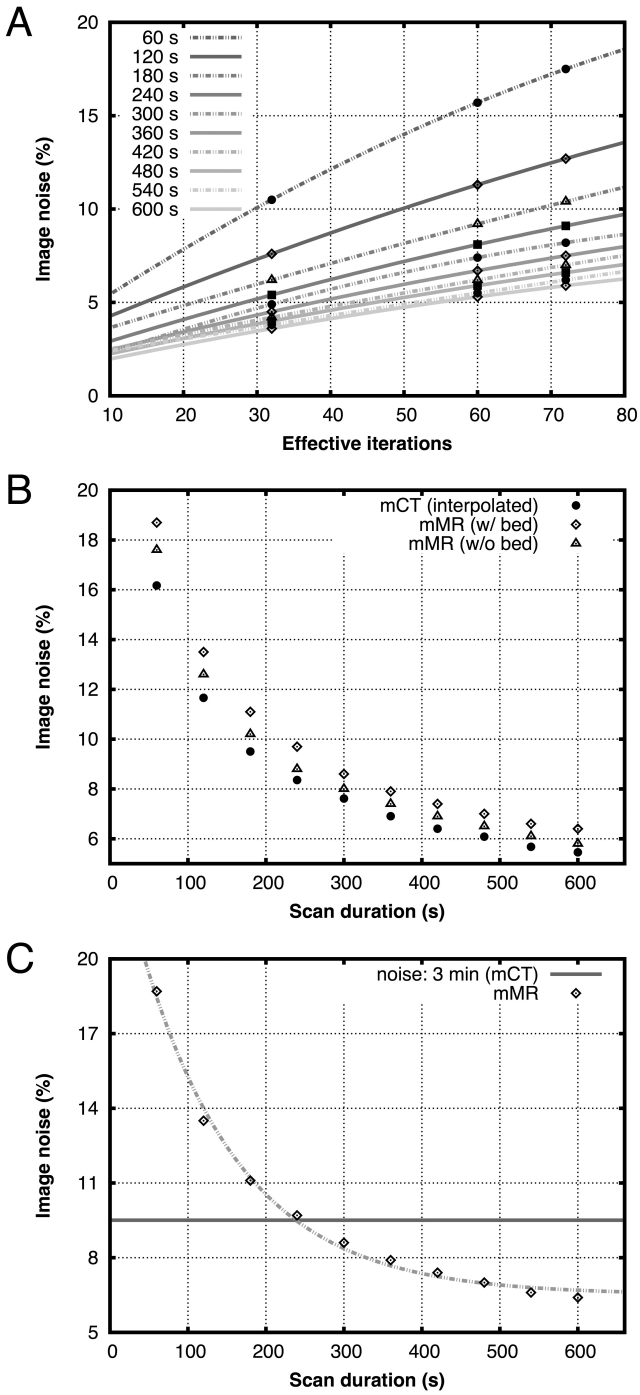

Figure 5.7.: (A) Interpolated image noise of the Biograph mCT for different scan durations as function of the number of effective iterations. The solid lines are the 2^{nd} order polynomials defined by the data points. (B) The image noise levels of the Biograph mCT and the Biograph mMR for 3 iterations and 21 subsets. (C) To derive the implications for scan time, an exponential function was fitted to the image noise of the Biograph mMR and its intersection with the noise level of the Biograph mCT (scan duration, 3 minutes) determined. The scan duration with the same noise level is approximately 30% longer on the Biograph mMR.

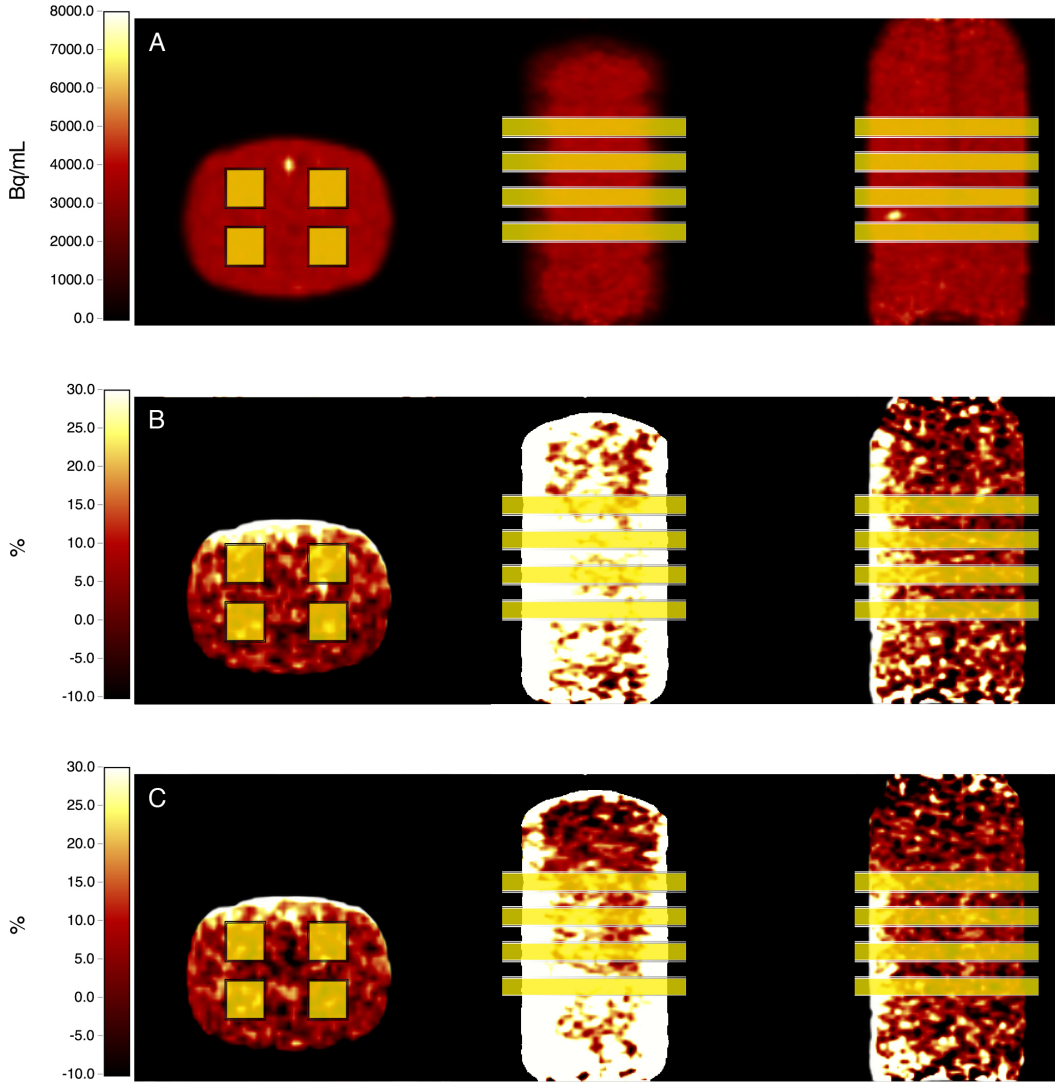

Figure 5.8.: Transaxial, coronal and sagittal slices (from left to right) through the image volume acquired during the 1st phantom measurement (A), the corresponding differences between the 1st and the 2nd phantom measurement (B) and those between the 1st and the 3rd phantom measurement (C) relative to the appropriate measurement with coil. The images are displayed in units of Bq/mL (A) and % (B, C) and were corrected for decay. The positions of the analysed VOIs are schematically overlaid. The spatial distribution of the effect shifts, as the coil is moved from position 1 (B) to position 2 (C).

The number of true events increased by 6.8% when the surface coil was removed from the centre position on the phantom, that is, when the 2nd scan was compared to the 1st scan. Relative to the 3rd scan, that is, with the coil on the second position, the number of true events was 4.6% higher in the 1st scan, that is, without a coil attached. In the 1st scan, 0.6% fewer true events were detected than in the 4th scan, that is, the second scan without coil. The trues-to-prompt ratios were 85.4%, 86.3%, 87.2% and 88.1% in the 1st, 2nd, 3rd and 4th scan, respectively. These numbers reveal increases of the trues-to-prompt ratio of 1.1%, 2.2% and 3.2% compared to the 1st scan.

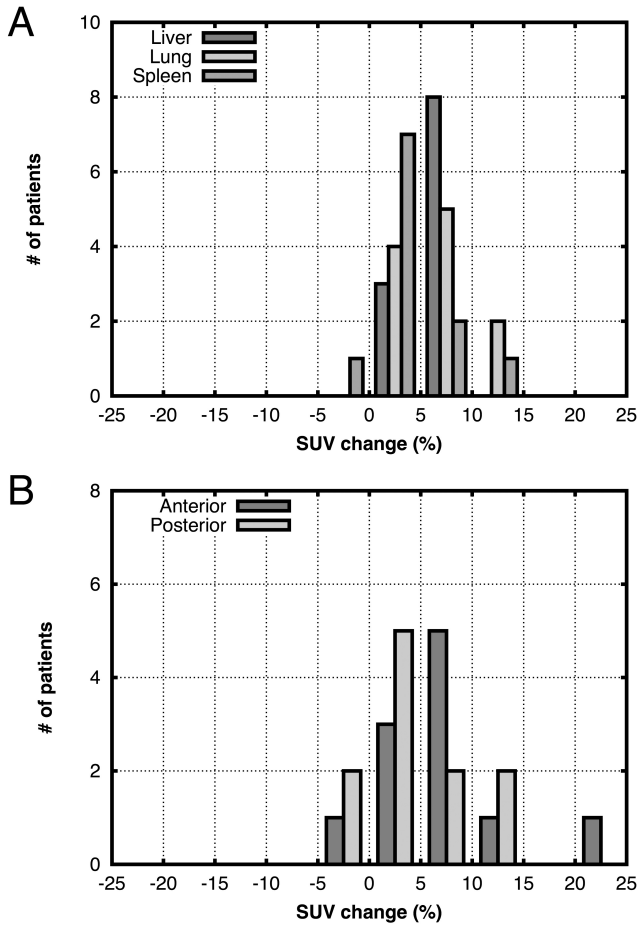

Figure 5.9.: The distribution of the average SUV_{mean} changes ($\Delta SUV = SUV_{withoutCoil} - SUV_{withCoil}$) in the transaxial organ VOIs (A) and in the coronal lung VOIs (B).

5.5. Results – In-vivo Study

5.5.1. SUVs

Organs (Transaxial)

The changes of the SUV_{mean} caused in the transaxial organ VOIs by the removal of the coil are plotted in Figure 5.9A. The effect was above 10% in one patient out of the entire 11 for the spleen and in two patients for the lungs. On average, the measured SUV_{mean} rose by $(2.8 \pm 4.2)\%$, $(6.0 \pm 3.7)\%$ and $(6.3 \pm 2.0)\%$ in spleens, lungs and livers, when the coil was detached.

Organs (Coronal)

As shown in Figure 5.9B, the effect in the lungs measured in the anterior and posterior coronal VOIs was higher than 10% in two of the 11 patients. With (6.6 ± 6.2)%, the average increase of the SUV_{mean} in the anterior lungs was higher than the (4.2 ± 5.7)% in the posterior.

Lesions (Global)

SUV_{mean} in lesions was on average (3.4 ± 14.3)% higher without surface coil. In 57% of the lesions, the effect exceeded 10% (Figure 5.10A). An effect of even more than 20% was observed in 17% of the lesions. If only SUV_{mean} changes of more than -5% are considered, the SUV_{mean} in lesions is on average (10.3 ± 9.3)% higher in the images of the second scan. The SUV_{max} increased on average by (4.2 ± 13.7)%, when the coil was removed. The differences between the SUV_{mean} and SUV_{max} changes in lesions were not found to be statistically significant ($p = 0.4$, paired two-sided t-test). Complete information can be obtained from Table 5.3.

Lesions (Size)

Eight of the lesions considered in this study had a size of less than 1 cm^3, 11 had sizes between 1 cm^3 and 2 cm^3, and 11 were larger than 2 cm^3. Within these subgroups, the SUV_{mean} changed by between -23% and +21%, -19% and +24% and -16% and +25%.

Lesions (Location)

Seventeen lesions were located in central, seven in posterior, and six in anterior regions of the patients' bodies. The average SUV_{mean} changes ranged between -23% and +25% in the central lesions, between -9% and +21% in the anterior lesions and between -19% and +24% in the posterior lesions.

Further grouping of lesions according to their size and location did not reveal additional information on the effect (Figure 5.10B).

5.5.2. Counts

By removing the surface coil from the patient, the number of detected true events increased on average by (6.1 ± 1.4)%. The mean of the trues-to-prompts ratio grew as well, by (2.5 ± 0.6)% from (51.5 ± 3.1)% to (52.8 ± 3.1)%.

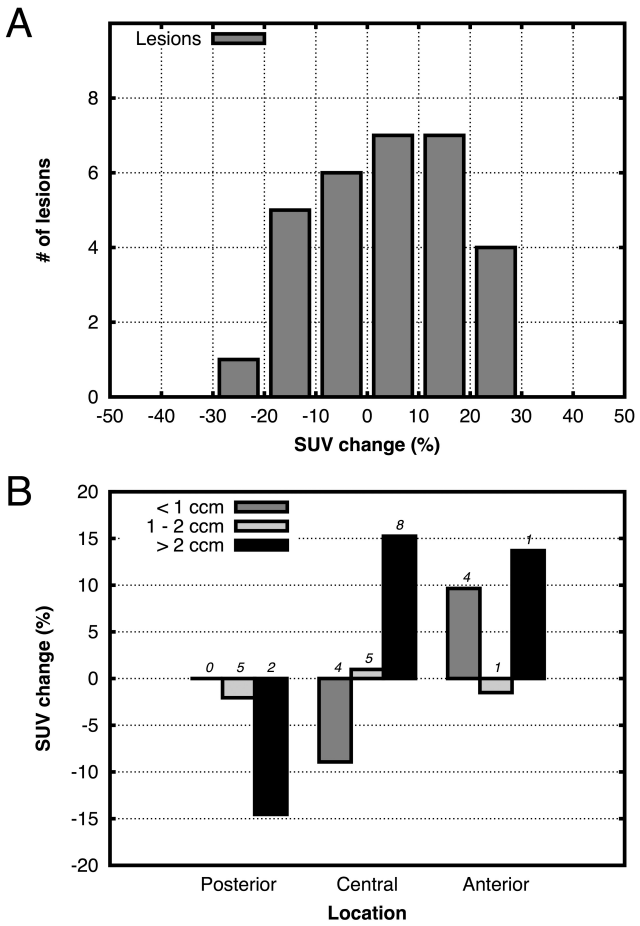

Figure 5.10.: The overall distribution of the average SUV_{mean} changes ($\Delta SUV = SUV_{withoutCoil} - SUV_{withCoil}$) in the lesions (A) and the SUV_{mean} changes according to lesion size and location (B). The number of lesions that fall into each group is written above the respective bar (B).

Patient	Diagnosis	Lesion	SUV_1		SUV_2		ΔSUV	
			mean	max.	mean	max.	mean	max.
2	Breast cancer	1	2.3	3.5	1.9	2.9	-18.7%	-17.9%
		2	3.5	5.7	3.0	4.9	-15.5%	-13.3%
		3	2.2	3.5	2.2	3.6	3.3%	3.4%
		4	1.7	2.4	1.9	2.8	14.9%	17.9%
4	Lymphoma	5	3.7	5.6	3.3	5.0	-9.7%	-10.8%
		6	2.4	3.9	3.0	5.0	24.6%	25.9%
6	Melanoma	7	8.1	12.0	9.2	13.7	13.7%	14.0%
		8	2.8	4.4	3.0	4.7	5.7%	7.3%
		9	6.9	10.1	8.1	12.0	17.5%	18.7%
		10	7.4	9.9	6.1	9.4	-17.8%	-5.6%
		11	3.7	5.6	4.1	6.0	11.6%	8.6%
7	Bronchial	12	9.7	14.9	11.6	17.9	19.7%	20.3%
	carcinoma	13	2.4	3.6	2.4	3.6	-2.9%	-1.9%
		14	4.2	6.6	4.4	6.5	3.3%	-1.7%
		15	3.4	4.9	4.1	6.4	22.1%	30.2%
8	Breast cancer	16	3.0	4.3	2.6	3.7	-13.5%	-14.6%
		17	1.4	2.1	1.3	2.1	-3.6%	-2.4%
		18	3.1	4.2	2.8	4.1	-9.3%	-2.9%
		19	2.7	4.2	2.7	4.1	-1.5%	-4.0%
		20	1.9	2.9	1.6	2.4	-17.5%	-19.0%
9	Breast cancer	21	5.7	8.5	6.7	9.8	18.0%	16.2%
10	Fallopian tube	22	2.7	4.3	2.8	4.3	5.2%	0.5%
	carcinoma	23	11.3	15.8	12.3	17.3	8.6%	9.2%
		24	4.6	5.7	3.6	5.4	-22.9%	-6.6%
		25	7.9	11.4	8.7	11.6	9.1%	1.2%
11	Breast cancer	26	2.9	4.5	3.3	5.2	13.6%	16.0%
		27	3.8	5.8	4.0	5.7	3.7%	-2.1%
		28	3.2	5.4	3.1	5.0	-4.1%	-6.7%
		29	2.2	3.5	2.8	4.3	23.8%	23.6%
		30	2.2	3.2	2.7	3.9	21.4%	22.3%

Table 5.3.: Lesions included in this study. On average, SUV_{mean} was $(3.4 \pm 14.3)\%$ higher without coil, whereas SUV_{max} increased by $(4.2 \pm 13.7)\%$.

5.6. Discussion

In this study, the effects on image quality and count statistics of additional hardware components of a PET/MR system, such as flexible coils and the patient table, were investigated. The findings regarding the patient table were compared to those for a PET/CT.

The patient table of the Biograph mMR results in a 70% higher gamma-ray attenuation compared to the Biograph mCT, which is an indicator of increased scattering. However, the full recovery during image reconstruction of a signal that is more severely affected by attenuation and scattering comes at the cost of image noise. As a result, the image quality of the Biograph mMR is not superior compared to the Biograph mCT despite its higher sensitivity. As expected, the noise level in the Biograph mMR PET images acquired without bed is lower than that of the Biograph mMR with bed and only 7% higher than that of the Biograph mCT with bed. The remaining discrepancy could be attributed to the higher reported scatter fraction of the Biograph mMR, which is a consequence of its reduced ring diameter and increased axial FOV as discussed in 3.4. Taking all these effects into account, the scan duration would have to be increased by approximately 30% for the Biograph mMR, to achieve the same noise level as the Biograph mCT in the case of a scan duration of 3 minutes.

The validity of the phantom measurements regarding the effect of the surface coil was supported by the two baseline measurements without coil. The corresponding difference of the SUV_{mean} in the simulated lesion is similar to the fluctuations reported by Schwartz et al. [86] for repeated measurements. According to their findings, these fluctuations are a result of the small lesion size and the lower count-rate statistics at the later time point of the second measurement. The overall effect of the surface coil as observed with the phantom was consistent with the findings in the patient study, both in terms of SUVs as well as detected counts. The slight discrepancies in the extent of the effect must be attributed to the different sizes and shapes of patients and phantom. As shown with the phantom, even a translation of the coil of roughly 5 cm had noticeable consequences for the extent of the effect. The increase of the trues-to-prompts ratio between the 1^{st} and the 4^{th} phantom measurements is explained with the higher relative change of the randoms compared to the trues rate as a function of activity concentration at the activity concentrations present in the measurement. This observation reflects the behaviour of the event rates as presented in 3.3.2.

The results of the patient studies showed that the effect of a surface coil on PET quantification in organs, as deduced from the average SUV change, is comparably small. Neither its deviation from the mean is substantial, as expressed by the fact that in more than 80% of the spleens, lungs and livers the observed effect was below 10%. Not surprisingly, the analysis of the coronal lung VOIs showed that the surface coil introduces a gradient of the measured

SUV such that its effect is more pronounced in regions closer to the coil. For any given voxel in such regions, the solid angle covered by the coil is larger and hence the number of LORs passing through the coil is higher.

The reason for the stronger and more variable manifestation of the effect in lesions is threefold.

1. Due to its flexible attachment by design, the coil will not be at the same location relative to the bed in two different studies. Thus, the position of any lesion relative to the coil was always different.

2. The naturally inhomogeneous composition of the coil in terms of attenuation properties results in the effect being confined to rather well-defined areas.

3. In contrast to the smaller lesions, the analysed organ VOIs could contain both severely and less severely affected regions, softening the overall effect and reducing deviation.

The statistical analysis of the difference between the change of SUV_{mean} and the change of SUV_{max} does not hint at inaccuracies of the reported results due to inconsistent lesion delineations.

The observation that approximately 6% more true coincidence events were detected on average without the surface coil is in line with the results from the quantitative analysis.

Zhang et al. observed 10% to 20% less counts in PET images acquired with a Philips Gemini TF PET/MR system, if the patient table was removed from the μ-map [109]. Tellmann et al. reported measured activity concentration changes due to the removal of a surface coil that was not optimised for the use with PET of between $\pm 4.1\%$ in the phantom lesions and between 0.8% and 2.7% in the background. The difference between two coil positions amounted to less than 4% [92]. A possible explanation for these lower values compared to the present study could involve the phantom design. The thick acrylic walls of the NEMA image quality phantom that was used by Tellmann et al. are very different from a patient and the thin-walled phantom employed in this study. This could lead to the diminution of the effect, because thick acrylic walls themselves attenuate gamma rays strongly.

Zhang and colleagues observed adverse and non-negligible effects on PET image uniformity and quantification for all coils under investigation in their study [109].

In general, the findings of Paulus et al. [70] on the same hardware, that is, the Biograph mMR, could be confirmed by this study both in terms of true counts as well as measured activity concentration or SUV.

For an earlier acquisition time point after administration of activity, Burger et al. reported a standard deviation of 3.6% for the change of the average SUV in lesions in two consecutive PET scans [9]. In a study of the Department

of Nuclear Medicine at Klinikum rechts der Isar of Technische Universität München, patients were scanned twice within 10 days without receiving treatment. The SUV in lesions did not significantly change, whereas the standard deviation was below 10% [102]. The standard deviation of the SUV change due to coil removal as observed in the present study is almost four times the first and 50% higher than the second value.

Regarding tracer kinetics, Kumar et al. found the change of SUV_{mean} between two scans with a delay of 38 minutes between them and the start of the 2^{nd} scan 101 minutes p. i. to be 12.7% in malignant breast cancer [50]. Matthies et al. observed a change of the SUV_{mean} in malignant pulmonary nodules of 20.5%. The delay between scans amounted to 56 minutes, whereas the 2^{nd} scan was started 122 minutes p. i. [62]. With these results, changes of the SUV_{mean} of between 2% and 3% can be estimated for the scan delay of seven minutes as reported in the present study. Since the second scan was started on average 151 minutes p. i., the contribution of tracer kinetics is likely lower. The decreased SUVs without coil may be attributed to decreased uptake in inflammatory lesions. Taking these aspects into account by only considering lesions with SUV_{mean} changes of more than -5% and by subtracting the contribution of the increased tracer uptake at the later time point, the effect of the surface coil in lesions is found to be approximately 8%. Schwartz et al. performed three sequential PET scans on the livers of each of eight patients [86]. The highest average SUV difference between the scans of a single patient as reported by Schwartz et al. was (1.6 ± 1.0)% and the mean SUV difference over the entire patient collective (0.8 ± 0.4)%, compared to (6.3 ± 2.0)% in the present study. Moreover, Wahl et al. conclude that a SUV change of more than 30% is classified as medically relevant, for example, as the response of a tumour to treatment [100]. However, as stated in 5.5.1, the observed effect of surface coils exceeded 20% in 17% of all lesions and in 18% of the lesions that exhibited an SUV change of more than -5%. All aspects combined, a strong point can be made for the clinical relevance of the local effect of surface coils in certain situations, for example, if different follow-up scans of the same patient are performed on a PET/MR and a PET/CT scanner or if different coil set-ups in terms of positioning and number of attached coils are chosen for two scans of the same patient.

Potential solutions for an improved repeatability of examinations include template μ-maps for the surface coils, similar to the approach implemented for static hardware 4.2.3. Alignment to the human μ-maps could be done with the help of markers that are visible to the system. Some possible correction schemes for MR equipment were evaluated in [20, 43, 70, 109]. Moreover, the coil design could be altered towards a more homogeneous attenuation of gamma rays.

5.7. Conclusions

Due to the additional attenuation caused by the coils and especially the patient table of the Biograph mMR, scan durations would have to be increased compared to current PET/CTs to provide similar image noise levels. The global effect of MRI surface coils could not be clearly distinguished from statistical fluctuations.

The application of surface coils led to a larger SUV decrease in anterior body regions. In lesions, however, the effect was more pronounced than in the background and a larger variability was observed. Depending on the relative position of the lesion to the coil, a considerable quantitative inaccuracy was found, affecting comparability across PET/MR and PET/CT scanners and within patient populations. Therefore, any type of material in the FOV of a PET scanner should be accounted for in AC.

Part IV.

Reducing Motion Artefacts

6. Motion Correction Strategies for Integrated PET/MR

Based on the work published in Journal of Nuclear Medicine (S. Fürst et al., J Nucl Med 2015; 56:261–269)

6.1. Introduction

Physiological motion is a major source of deterioration of image quality in PET, leading to image blurring, rendering tumour uptake quantification less accurate and lesion volume delineation more difficult [66]. Various methods for the reduction of motion artefacts in PET images were proposed, including gating [66], image-based approaches [8,28,74] and the incorporation of motion information into the reconstruction algorithm [51, 78]. Gating constitutes a trade-off of scan duration and image quality, because only a fraction of the acquired PET coincidences is taken into account for the reconstruction of individual gates. This leads to lower sensitivity, worse statistics and higher noise. Prolongation of examinations improves image quality, but adversely affects patient comfort and throughput. Despite this disadvantage, gating is still the most widely used respiratory motion compensation scheme.

For the correction of respiratory motion in PET, two types of information are essential, vector fields describing the motion within the body of the patient and a respiratory signal, which establishes the connection between motion model and PET data. The integration of whole-body PET with MRI and its introduction to the clinical routine facilitate the implementation of a broad variety of motion-correction strategies, taking advantage of the respective strengths of both modalities.

The respiratory signal can be obtained with external sensors, for example, respiratory belts or cameras in combination with fiducial markers mounted to the chest of the patient [54, 66, 99], or extracted from PET data [10, 36, 94]. In MR, navigator echoes are used to track the position and phase shifts of objects of interest in the FOV that are subject to respiratory motion, mostly the liver dome [26].

With regard to the acquisition of motion vector fields, MR-based motion modelling techniques [63] appear to be the logical choice due to their analysis of physical deformation of anatomical structures for the detection of motion.

However, other methods were published in recent years that promise to derive the flow of activity directly from PET data [19]. MR-based PET motion correction is widely assumed to be more robust due to the anatomical information and higher SNR of MR images, but is otherwise invasive and costly. Already demanding PET/MR workflows and scan protocols [60] would have to be extended for motion-modelling scans, whereas the acquisition of respiratory signals would block the subsystem with dedicated MR sequences throughout the entire PET examination. Alternatively, all clinical MR sequences would have to be interleaved with navigators, which might not be possible for any sequence with the sampling frequency required for respiratory gating or without inducing image artefacts. These factors might put further constraints on PET/MR protocols, limiting patient comfort and throughput. In contrast, PET-driven motion correction and its implementation might appear straightforward. However, it is still considered less accurate and reliable due to higher noise of PET data, subject to count rate statistics and tracer kinetics.

None of the published studies of motion correction include a direct comparison of the two types of motion correction. The respective authors derived their results either from animal studies [16] or with simulated or phantom data [21, 22, 35, 71, 76, 77]. PET-driven motion correction was assessed with data of 14 patients [19], whereas MR-based motion correction was so far evaluated with data of 5 patients at maximum [72, 105].

Therefore, the goal of this study was the evaluation of different motion-correction strategies for integrated PET/MR. Within the scope of the present study, a variation of methods is proposed for the extraction of respiratory signals from PET list-mode data, testing the results on clinical data of 20 patients against MR- and sensor-based gating methods. Additionally, a rigorous comparative study of MR- and PET-driven motion-corrected PET image reconstruction was performed in terms of tracer uptake quantification, lesion volume definition and image quality with clinical data of 14 patients.

6.2. Materials and Methods

6.2.1. Motion Correction Strategies

All motion correction strategies comprise three distinct steps that will be described in the following section:

1. Respiratory gating
2. Calculation of motion vector fields
3. Motion-corrected iterative PET reconstruction

Respiratory Gating

As PET and possibly MR data have to be gated retrospectively, exact knowledge on the corresponding respiratory state is required at any time point during the examination. Within the scope of this study, this was achieved by the acquisition of respiratory signals according to five methods:

1. **resp_bellows** – The pressure-sensitive respiratory bellows that is shipped with the scanner by default.
2. **resp_mr** – A prototype implementation of a self-gated T1-weighted radial stack-of-stars spoiled 3d GRE MRI pulse sequence with fat suppression [14, 34].
3. **resp_sens** – The PET-based sensitivity method [10, 36].
4. **resp_pca** , **resp_le** – The application of dimensionality reduction techniques such as principal component analysis (PCA) and Laplacian Eigenmaps (LE) to the sinogram space [81, 94, 95].
5. **resp_pca+sens** , **resp_le+sens** – A proposed method that combines resp_sens and resp_pca or resp_le.

Prior to the execution of the PET-based methods, the list-mode streams were divided into non-overlapping 200 ms time frames. For resp_sens, the corresponding numbers of true and scattered coincidences were determined and decay and subsequently – to account for, for example, uptake variations over time due to tracer kinetics – baseline corrections performed with a window width of 5200 ms. Two iterations of a centred moving average filter with window widths of 600 ms and 800 ms and a median filter with a window width of 600 ms were applied for the removal of noise from the signal.

The processing steps of resp_pca and resp_le are outlined in (Figure 6.1). The number of planes of each of the frame sinograms in the resulting time series was reduced from 4084 to 127 by means of SSRB. Each first and last

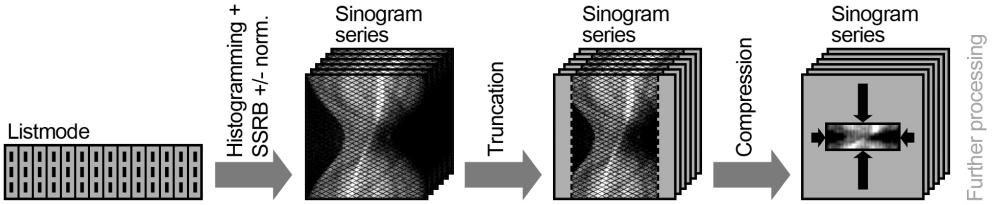

Figure 6.1.: Prior to the application of dimensionality reduction techniques, a series of sinograms is created from the list-mode stream. The sinograms are then truncated and compressed by means of mashing and merging of adjacent radial bins. If the planes of rebinned sinograms are not normalised for the number of contributing LORs, the sensitivity profile of the scanner is preserved.

six planes were further deleted due to the lower number of contributing LORs and the resulting higher noise in these planes. All but the central 176 radial bins of each projection were additionally cropped to restrict the analysis to bins representing radial positions inside of the patients' bodies with tracer uptake and respiratory motion. Seven different levels of radial compression and angular mashing were evaluated, ranging from 44 bins and 9 projections to one bin and one projection. PCA and LE were applied to the sinogram series using the MATLAB Toolbox for Dimensionality Reduction [98]. In the case of LE, the number of nearest neighbours k in the neighbourhood graph was set to $\frac{N}{2}$, with N being the number of sample points, which are in this case the sinograms in the series. Apart from this, the default parameters were adopted. A qualitative analysis found the respiratory signal to be best contained by the first component or dimension of the low-dimensional representation of the sinogram series data, which is also suggested by the literature [94]. As with resp_sens, noise was removed by employing a median filter with a window width of 1400 ms and a centred moving average filter with two iterations and a window width of 600 ms.

A fifth method was proposed and evaluated in this study, which builds on resp_pca and resp_le, but integrates resp_sens (resp_pca+sens, resp_le+sens). This is achieved by omitting the SSRB normalisation of sinogram bin values to the number of LORs contributing to the corresponding plane. Thus, the axial sensitivity profile of the PET detector system (compare 3.3.3) was preserved in sinogram space. Apart from the normalisation, the processing regarding resp_pca+sens and resp_le+sens was identical to that of resp_pca and resp_le.

Calculation of Motion Vectors

Sets of motion vector fields M describing the inter-gate displacement of morphological structures are required for the warping of image volumes and volumes of acquired AC factors from the reference to the other respiratory

states as defined by the gates. For MR-based motion correction (moco_mr), M is calculated by acquisition of MR images at each gate and subsequent non-rigid registration. In the present study, the inverse motion vector fields M^{-1} from gate to reference were generated by estimating for each voxel in the target image volume the corresponding voxel index in the reference after backward transformation to the reference. Special care was taken that spatial mismatch between an original voxel in the reference image and the corresponding voxel after the full warp cycle, that is, a forward transformation from reference to gate followed by the backward transformation from gate to reference, was minimal. Otherwise, such inconsistency would lead to a loss of resolution and adverse effects on image quantification in motion-corrected iterative PET image reconstruction.

In the absence of other imaging modalities, motion information can be derived from PET images employing optical flow algorithms [19]. Dawood et al. explain that classical optical-flow algorithms are based on the assumption that the brightness of an object does not change between two images. Due to partial volume effects, however, this is not true in PET. The PET-driven method in this study (moco_pet) is based on a mass-conserving algorithm with an improved constraint as proposed by Dawood et al., which assumes equal overall activity in each image [19].

According to Dawood et al. [19], the optimal values of the velocity $\mathbf{u} = (u, v, w)^T$ of the moving activity, that is, the optical flow describing the motion between gates, can be calculated by iteratively minimising an optical-flow functional $f_{\mathrm{mc}}(\mathbf{u})$, given as

$$f_{\mathrm{mc}}(\mathbf{u}) = \int_V \underbrace{\left(\mathrm{div}(I\mathbf{u}) + \frac{\partial I}{\partial t}\right)^2}_{\text{mass-conserving constraint}} dV + \\ + \int_V \alpha \overbrace{\left(|\nabla u|^2 + |\nabla v|^2 + |\nabla w|^2\right)}^{\text{smoothness constraint}} dV \qquad (6.1)$$

where $I(x, y, z, t)$ is the voxel intensity, V the image volume and α a weighting factor. The first term of the functional ensures mass conservation and the second smoothness of the transition between gates.

This method works with PET alone and does not need any information from other modalities. The resulting information describes the motion in 3d. Moreover, the number of adjustable parameters is very low. Only α has to be adjusted and, before application, the initial scaling between the images of the gates of interest [39].

Motion-corrected Iterative PET Reconstruction

It is desirable to incorporate the two types of previously described information into the process of image reconstruction instead of manipulating reconstructed

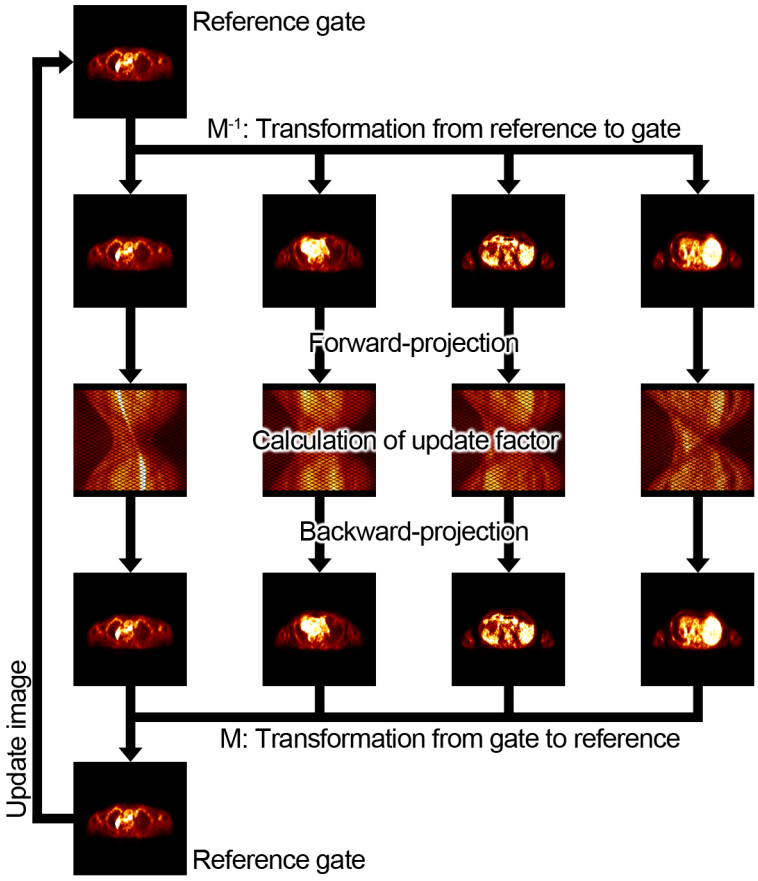

Figure 6.2.: Schematic of the workflow for incorporation of motion information into the OSEM reconstruction algorithm.

images. The most straightforward approach extends the conventional OSEM algorithm by integrating a warp function into the forward and backward projectors (Figure 6.2):

$$I^{i+1}(b) = I^i(b) \cdot \frac{1}{\sum_g M^{-1}\left(B\left(\frac{1}{A(l,g)} \cdot N(l)\right), g\right)} \cdot \cdot \sum_g M^{-1}\left(B\left(\frac{P(l,g)}{F\left(M\left(I^i(b), g\right)\right) + \mathcal{O}(l,g)}\right), g\right) \quad (6.2)$$

where $I^i(b)$ is the image estimate in the reference state for voxel b after the ith iteration. $M(J, g)$ specifies the transformation of an image volume J from the reference to gate g and $M^{-1}(J, g)$ the inverse direction. B denotes the back-projection from sinogram to image space and F the corresponding forward-projection. $A(l, g)$ provides the AC factors for LOR bin l and $N(l)$ the normalisation. $P(l, g)$ is the number of coincidence events, whereas the term $\mathcal{O}(l, g)$ accounts for random and scattered events and attenuation.

By combining the most suitable methods for each of these steps, a motion correction strategy could be optimised for specific clinical requirements.

6.2.2. Patient population

The respiratory gating and motion correction methods presented above were applied to a total number of 20 patients, of whom 11 were female and nine male. The patients had been referred to the Department of Nuclear Medicine at Klinikum rechts der Isar of Technische Universität München for the diagnosis and staging of malignant diseases (abdomen, 11; cardiac, 1; thorax, 8) using ^{18}F-FDG PET/CT or PET/MR or ^{68}Ga-DOTANOC [104] PET/MR (FDG, 18; DOTANOC, 2). They were (64 ± 14) years of age and had a weight of (76 ± 15) kg. The diseases include breast, liver and pancreatic cancer with additional lesions in, for example, lungs, lymph nodes, oesophagus and small intestine. In general, only moving and well-circumscribed lesions were considered in this study.

All patients gave written informed consent to participate in this study and, if only a PET/CT examination was clinically required and scheduled, undergo a second scan on the PET/MR. The approval of the institutional review board and the radiation protection authorities had been obtained. No additional radiotracers were injected after the first scan.

6.2.3. Acquisition

Instrumentation

All data in this study were acquired on the Biograph mMR PET/MR system (3.2.1). Apart from the standard body coil and spine array coils, a flexible

6-element surface coil (Body Matrix Coil, Siemens Healthcare, Germany) was used for the MR measurements.

Imaging Protocol

Patients were injected with (339 ± 63) MBq of ^{18}F-FDG or 93 MBq/122 MBq of ^{68}Ga-DOTANOC and scanned (136 ± 24) min (FDG) or 66 min/52 min (^{68}Ga-DOTANOC) after injection. Prior to a scan, the patient was positioned on the scanner bed with the arms beside the torso and the respiratory bellows attached between costal arch and sternum to improve the signal for abdominal or thoracic breathing. One or two of the aforementioned body array coils were placed on abdomen or thorax, depending on the size of the patient and the body region to be examined as required by the indication. This region was then centred in the FOV of the scanner. A prototypical radial stack-of-stars 3d GRE sequence (sagittal slab orientation; FOV, 400 × 400 × 360 mm^3; spatial resolution, 1.65 × 1.65 × 5 mm^3; matrix, 256 pixels; 72 slices; 61% slice resolution; 5/8 partial Fourier) was employed for the subsequent derivation and calculation of MR-based respiratory signals and motion vectors fields. After μ-map generation with the 2-point Dixon sequence (4.2.3), for which patients were given commands to hold their breath at end-expiration, PET list-mode and radial MR data were simultaneously acquired for 10 minutes.

6.2.4. Processing

Respiratory Signals and PET Gating

All recorded respiratory traces were resampled to 10 Hz using spline interpolation to eliminate other effects on gating. They were then normalised for correlation analysis according to the following equation, where $\mathrm{y}(t)$ is the signal height at a time point t and $\mu(\mathrm{Y})$ and $\sigma(\mathrm{Y})$ the average height and corresponding standard deviation of the entire respiratory trace Y:

$$\mathrm{y}_{norm}(t) = \frac{\mathrm{y}(t) - \mu(\mathrm{Y})}{\sigma(\mathrm{Y})} \tag{6.3}$$

list-mode events were binned into sets of gated sinograms by means of variable-amplitude-based gating [18] according to the produced respiratory signals. The number of gates was set to 5, which constituted a good compromise between captured respiratory motion and noise in the reconstructed PET images and is identified as appropriate in the literature [69]. Sinograms comprised of PET data from the entire scan (static) were also generated for each patient.

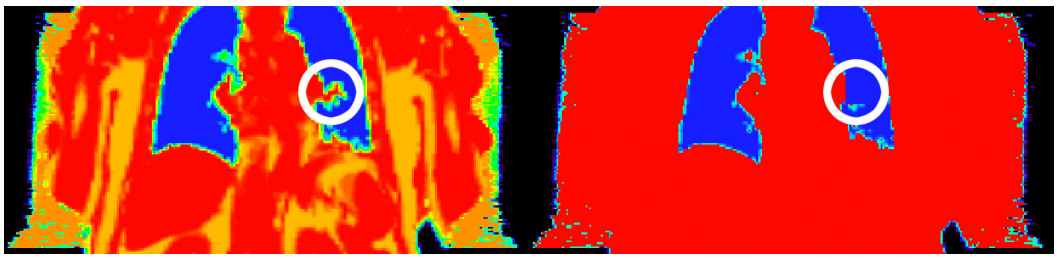

Figure 6.3.: Example of an original μ-map as segmented by the Biograph mMR (left) and the same μ-map modified for the evaluation of motion correction (right). To reduce mismatch of attenuation and emission data, voxels segmented as fat (orange) were assigned the attenuation coefficient of soft tissue (red), whereas morphological structures in the vicinity of lung lesions were erased (encircled).

Motion-field Estimation

Radial MR readouts were partitioned according to resp_mr, following the steps previously outlined for PET gating, and corresponding gated MR images reconstructed. A non-rigid registration algorithm previously proposed for lung imaging [37] was applied for the calculation of motion vectors. The gate comprising data recorded at end-expiration was selected as reference, since it is least affected by intra-gate motion under the current gating scheme. The resulting motion vector volumes were resampled to the PET image volume dimensions.

Attenuation Correction

Patient μ-maps were created by segmenting the fat and water images generated by the Dixon MRI sequence (4.2.3). The original μ-maps with four tissue classes [61] were then utilised for the reconstruction of images that formed the basis of the respiratory gating analysis. Instead of following this approach for the motion correction evaluation, all voxels in the μ-maps classified as fat were assigned the slightly higher attenuation coefficient of soft tissue. Additionally, morphological structures in the lungs at or close to the location of lesions were erased from μ-maps for each lesion individually by setting the values of all voxels in the VOIs drawn for the analysis of PET images to that of lung tissue (Figure 6.3). This measure was taken to isolate the outcomes of motion correction from adverse effects caused by mismatch of attenuation and emission data at tissue boundaries. Truncation of arms in μ-maps due to the limited FOV of the MR subsystem was compensated by the application of maximum-likelihood reconstruction of attenuation and activity [68]. For the reconstruction of attenuation-corrected PET images at end-inspiration, motion vector fields were additionally applied to deform the μ-maps from the reference to this state.

PET Image Reconstruction

Static, gated and motion-corrected PET images were reconstructed from all previously described sinograms and sets of sinograms using the corresponding original and modified μ-maps and following the clinical standard in the Department of Nuclear Medicine at Klinikum rechts der Isar of Technische Universität München. This requires an OSEM 3d algorithm with 3 iterations, 21 subsets, a 172×172 matrix and a 4.0 mm Gaussian post-reconstruction filter [24]. In addition to attenuation, data were also normalised and corrected for dead time, scatter, decay, frame length and randoms.

The gates were numbered in increasing order from end-expiration, that is, gate 1, to end-inpiration, that is, gate 5. For the analysis of both respiratory gating and motion correction, the gate at end-expiration was selected as the reference.

6.2.5. Analysis

Respiratory signals of all 20 study patients were evaluated. Of these 20 patients, only those with moving lesions that exhibited tracer uptake sufficient for unambiguous segmentation in all static, gated and motion-corrected images were included for subsequent image-based analysis of respiratory gating and motion correction, resulting in 14 patient data sets with a total number of 27 lesions. For the validation of respiratory gating, only one lesion was considered per patient to avoid bias.

Respiratory Signals

The processed respiratory traces were evaluated in terms of signal shape and breathing frequency spectra. The Pearson's correlation coefficients of resp_mr with all other methods were additionally calculated.

PET Image Quantification

The effects of respiratory gating and motion correction on reconstructed images were analysed in terms of apparent tracer uptake concentration in suspected tumour lesions and background tissue. Firstly, rectangular volumes were defined for each lesion. Their location and size were chosen such that the respective lesion was properly enclosed in all image volumes. Due to the inter-gate motion of lesions, different volume definitions had to be chosen for assessment of respiratory gating and motion correction in some cases. Secondly, an isocontour VOI was segmented for each lesion. For this purpose, the voxel with the highest activity concentration in the previously defined rectangular volume was identified and selected as seed point for a region-growing algorithm. In its current implementation, the algorithm iteratively creates the isocontour VOI by including the voxels that are adjacent to the isocontour

VOI as produced in the preceding iteration, if their values are higher than a specified threshold. The procedure stops, if no additional voxels are added to the isocontour VOI. In this study, an isocontour threshold of 50% was used. The procedure was applied to each lesion individually. Thirdly, apart from the already determined maximum activity concentration, the average activity concentration A in each isocontour VOI was calculated, as well as standard deviation σ, contrast C and signal-to-noise ratio SNR. The latter were defined in a similar way as in a previous study [46]:

$$C = \frac{A_{lesion} - A_{background}}{A_{background}} \tag{6.4}$$

$$SNR = \frac{A_{lesion} - A_{background}}{\sigma_{background}} \tag{6.5}$$

For the analysis of background tissue, one rectangular cuboidal VOI per patient was defined in the liver under the constraint that the VOI could not include edge voxels or focal tracer uptake. The thus maximum possible size was additionally restricted to $11 \times 11 \times 21$ voxels ($4.6 \times 4.6 \times 4.3$ cm^3). Image noise was then expressed as relative standard deviation of all voxel values in the background VOI.

Lesion Displacement and Volumes

The position of an isocontour VOI along the craniocaudal axis was computed as its centre of mass COM as previously published [7],

$$z_{COM} = \frac{\sum_i z_i \cdot a_i}{\sum_i a_i} \tag{6.6}$$

where z_i is the coordinate on the craniocaudal axis of the ith voxel in the VOI and a_i its activity concentration. Lesion displacement Δz was measured for the evaluation of respiratory gating as the absolute difference between the positions in gate 1 and gate 5. Lesion volume V was defined as the total volume of all voxels within the isocontour VOI in the reference gate.

Statistical Analysis

The two-sided paired Wilcoxon signed-rank test was performed to determine statistical significance of the results. Differences for which p-values of equal to or more than 0.05 were calculated were regarded as statistically insignificant.

6.3. Results

6.3.1. Respiratory Gating

Respiratory Signals

Motion-corrected Iterative PET Reconstruction

For all 20 patients, respiratory traces could be successfully generated (Figure 6.4). The positions of inhalation peaks and overall noise of resp_bellows and resp_mr were visually well comparable and consistent. This was reflected by the corresponding frequency spectra (Figure 6.5). However, due to the limited recorded range of signal heights as currently implemented on the PET/MR scanner, inhalation peaks in resp_bellows were frequently cut off. Therefore, resp_mr was chosen as the reference signal. The average coefficients of correlation between resp_bellows and resp_mr were 0.63 ± 0.19, ranging from 0.13 to 0.94, and between resp_sens and resp_mr 0.52 ± 0.26 taking values between 0.01 and 0.86. Dimensionality reduction techniques yielded average correlations between 0.25 ± 0.30 and 0.42 ± 0.34 (resp_mr with resp_le) and between 0.25 ± 0.30 and 0.58 ± 0.33 (resp_mr with resp_pca), depending on the level of mashing and radial compression. The preservation of the sensitivity profile in the processed data increased the maximum average correlation of resp_le+sens with resp_mr to 0.70 ± 0.19. The application of PCA to a sinogram space with 44 radial bins and three projections with the sensitivity profile preserved, which will be denoted with resp_pca443sens in the following, resulted in the highest average correlation of 0.74 ± 0.21 with a maximum correlation of 0.93 and a minimum of 0.06 between resp_mr and any PET-driven extraction method. If the PET-based extraction method that presented the highest correlation with resp_mr was selected for each patient individually, which will be referred to as resp_bestpet, an even higher correlation of 0.80 ± 0.13, yielding correlations between 0.40 and 0.93, was achieved on average for the entire patient population. The coefficient of correlation with resp_mr was higher than 0.8 for 15% (resp_bellows), 15% (resp_sens), 55% (resp_pca443sens) and 65% (resp_bestpet) of all 20 patients (Figure 6.6). Complete information with regard to all levels of compression can be obtained from (Table 6.1. Based on these results, gated and motion-corrected images, the analysis of which will be presented in the subsequent sections, were reconstructed from gated sinograms created according to resp_pca443sens and resp_bestpet, in addition to resp_bellows, resp_mr and resp_sens. The resulting coefficients of correlation with resp_mr for all studied patient samples are summarised in Table 6.2.

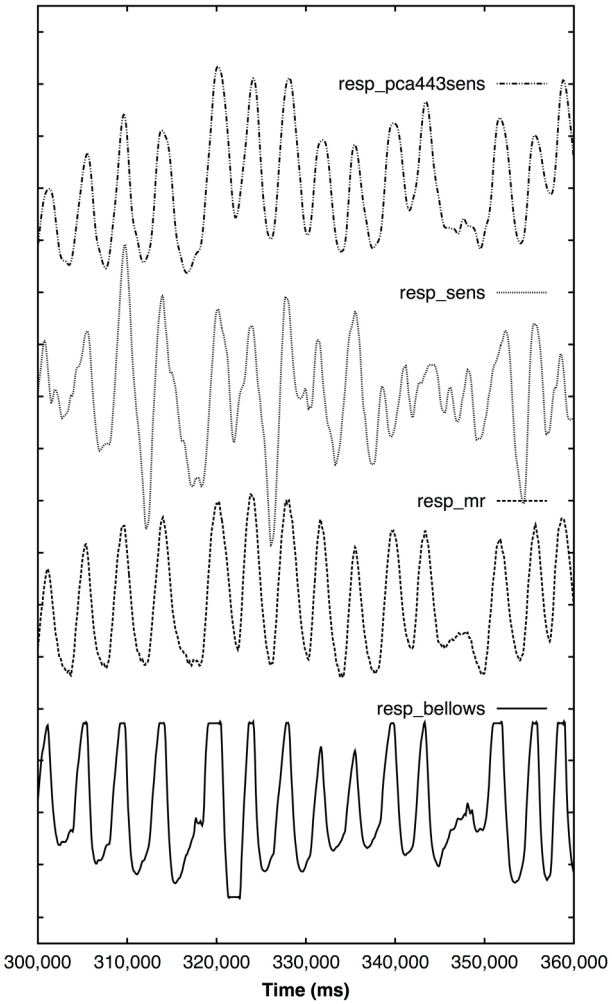

Figure 6.4.: Respiratory traces of patient 8 from a 60-s mid-scan window. Correlation coefficients with resp_mr as reference were 0.71 (resp_bellows), 0.79 (resp_sens) and 0.92 (resp_pca443sens). resp_bellows is cut-off above a certain signal height, whereas resp_sens appears noisiest. Visual impression confirms the high correlation between resp_mr and resp_pca443sens.

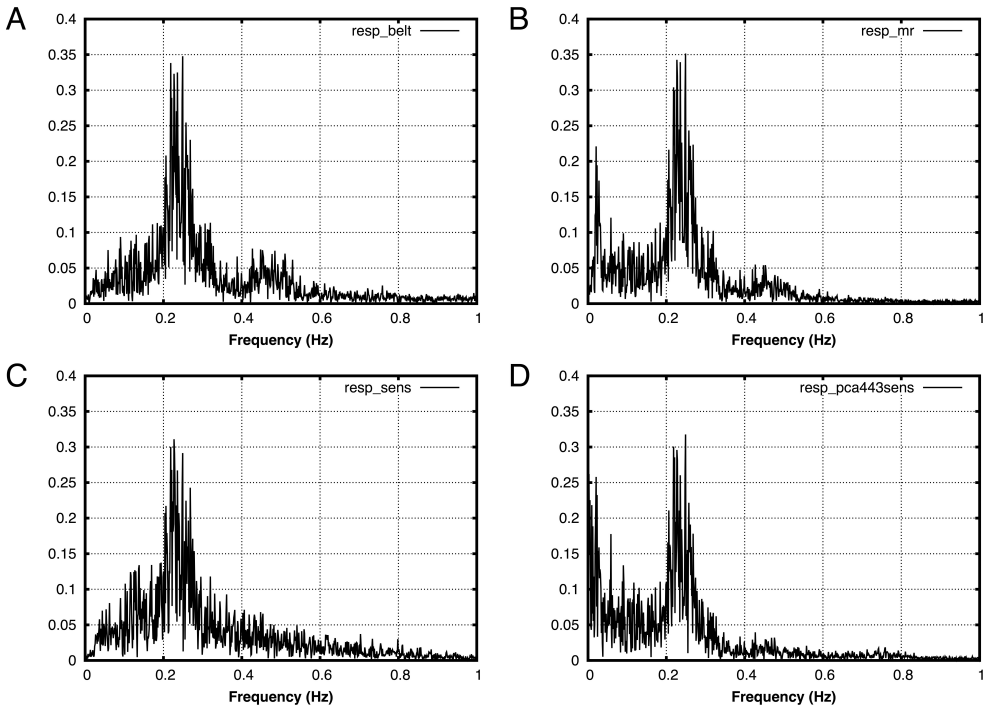

Figure 6.5.: Fourier breathing frequency spectra of patient 8, for (A) resp_bellows, (B) resp_mr, (C) resp_sens and (D) resp_pca443sens. The main peak is at the same position for all four signal sources and slightly broadened in (C). Another peak at approximately 0.45 Hz in (A) and (B) is flattened in (C) and (D) due to the use of median and moving-average filters. Correction of the signal baseline in the case of resp_bellows and resp_sens lead to the downward slope towards lower frequencies of the corresponding spectra (A, C) below 0.1 Hz.

Radial Bins	Projections	Correlation Coefficients			
		resp_le	resp_pca	resp_le+sens	resp_pca+sens
1	1	0.25 ± 0.30	0.25 ± 0.30	0.51 ± 0.29	0.52 ± 0.29
11	1	0.30 ± 0.32	0.33 ± 0.34	0.70 ± 0.19	0.73 ± 0.14
22	1	0.34 ± 0.34	0.40 ± 0.34	0.63 ± 0.25	0.71 ± 0.17
44	1	0.31 ± 0.32	0.36 ± 0.34	0.56 ± 0.30	0.67 ± 0.24
44	3	0.42 ± 0.34	0.56 ± 0.34	0.60 ± 0.24	0.74 ± 0.21
44	6	0.39 ± 0.32	0.58 ± 0.33	0.54 ± 0.25	0.71 ± 0.25
44	9	0.37 ± 0.30	0.56 ± 0.34	0.46 ± 0.29	0.69 ± 0.26

Table 6.1.: Coefficients of correlation between resp_mr and respiratory traces produced by applying dimensionality reduction techniques to different compressions of the sinogram space. Shown values are averaged over the entire patient population (mean ± standard deviation).

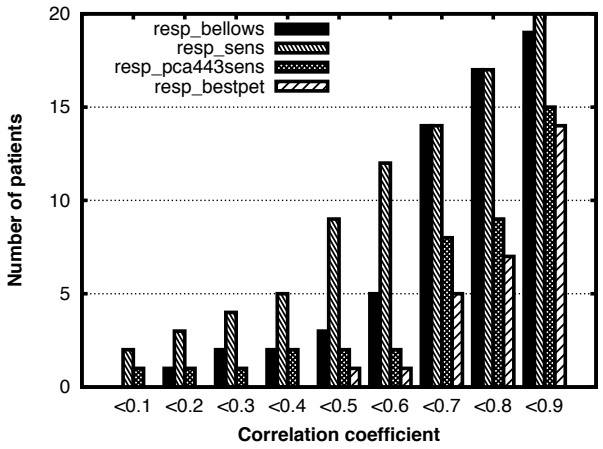

Figure 6.6.: Cumulative frequency histogram of the coefficients of correlation of resp_bellows, resp_sens, resp_pca443sens and resp_bestpet with resp_mr as reference. The correlation coefficient was higher than 0.6 for 75% (resp_bellows), 40% (resp_sens), 90% (resp_pca443sens) and 95% (resp_bestpet) of all 20 patients.

	Correlation Coefficients			
	resp_bellows	resp_sens	resp_pca443sens	resp_bestpet
All				
mean ± std.	0.63 ± 0.19	0.52 ± 0.26	0.74 ± 0.21	0.80 ± 0.13
max.	0.94	0.86	0.93	0.93
min.	0.13	0.01	0.06	0.40
Patients in image-based analysis				
mean ± std.	0.71 ± 0.11	0.55 ± 0.20	0.80 ± 0.10	0.81 ± 0.09
max.	0.94	0.81	0.93	0.93
min.	0.55	0.16	0.66	0.67

Table 6.2.: Coefficients of correlation between resp_mr and resp_bellows and the highest-quality PET-based gating methods for all study patients and those included in the image-based verification of respiratory signals and analysis of motion correction.

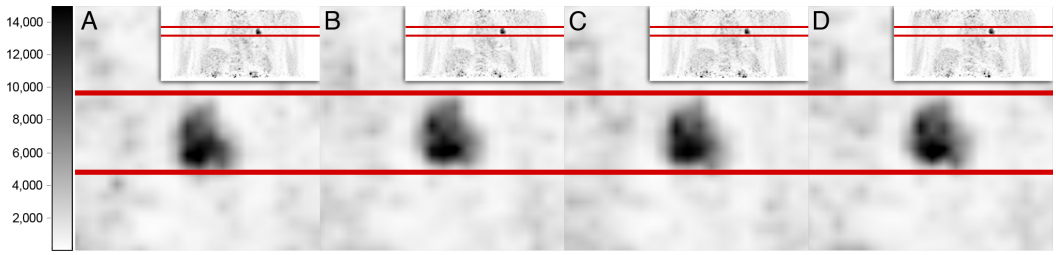

Figure 6.7.: Coronal slices through a lesion of patient 8, in images (gate 1) gated according to (A) resp_bellows, (B) resp_mr, (C) resp_sens and (D) resp_pca443sens. Visual differences in terms of lesion volume and location between (B), (C) or (D) are negligible. Compared to the other images, the lesion appears to be slightly shifted in (A), possibly indicating a higher degree of intra-gate motion.

Tracer Uptake in Lesions

The differences between all methods in terms of maximum and average tracer uptake in lesions were not significant, with p-values of $p \geq 0.103$ and $p \geq 0.209$ for maximum and mean uptake, respectively.

Lesion Displacement

The only significant differences in terms of lesion displacement were found between resp_bellows and resp_pca443sens ($p = 0.020$), between resp_sens and resp_mr ($p = 0.005$), resp_sens and resp_pca443sens ($p = 0.007$) and between resp_sens and resp_bestpet ($p = 0.017$). All other combinations yielded p-values $p \geq 0.052$.

Lesion Volumes

Significant differences regarding lesion volumes were observed when comparing resp_bellows and resp_bestpet and between resp_bellows and resp_pca443sens, for which p-values of $p = 0.043$ and $p = 0.045$ were calculated, respectively.

The quantitative analysis of gated images is summarised in Table Table 6.3, whereas an example is shown in (Figure 6.7).

6.3.2. Motion-corrected Iterative PET Reconstruction

Both methods of motion correction included in this study improved the visual impression of the reconstructed PET images (Figure 6.8). Size and location of morphological structures in gated and both of the motion-corrected images were consistent. In static images, the same structures appeared blurred and larger, the latter of which was most obvious in smaller volumes of focal tracer uptake. However, image noise was significantly lower in moco_mr and moco_pet than in gated images, whereas the noise patterns in static and

	resp_bellows	resp_mr	resp_sens	resp_bestpet
Max. activity concentration				
Static (kBq/mL)		21.7 ± 17.5		
Gate 1 (% static)	113.5 ± 11.6	116.9 ± 15.5	110.4 ± 9.1	117.1 ± 15.6
Mean activity concentration				
Static (kBq/mL)		14.4 ± 11.6		
Gate 1 (% static)	111.3 ± 10.1	114.8 ± 13.8	109.8 ± 7.9	114.3 ± 11.4
Volume				
Static (10^3 mm^3)		6.5 ± 8.9		
Gate 1 (% static)	80.1 ± 23.5	76.6 ± 24.6	81.3 ± 19.2	73.5 ± 30.3
Displacement				
Gate 1 - 5 (mm)	4.4 ± 2.6	5.2 ± 3.0	3.8 ± 3.3	5.4 ± 2.6

Table 6.3.: Complete results from the quantitative image-based analysis of respiratory gating methods. Maximum and mean tracer uptake in lesions, lesion volumes and displacements are presented for static and gated images. Results based on resp_pca443sens are not shown due to the similarly high quality of resp_pca443sens and resp_bestpet regarding the included patients.

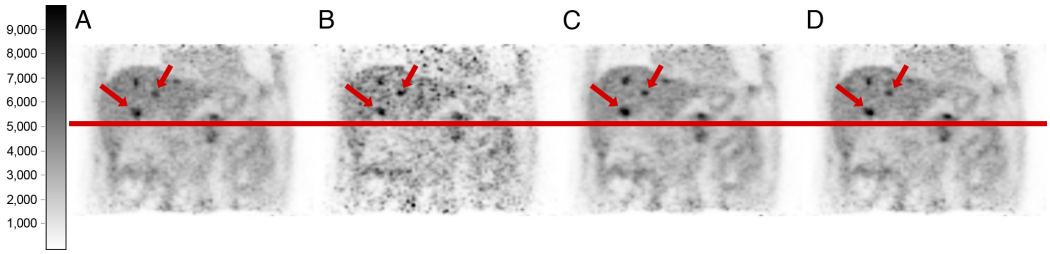

Figure 6.8.: Coronal slices through (A) static, (B) gated (gate 1), (C) moco_mr and (D) moco_pet images of patient 4. Gating was performed in all cases according to resp_pca446sens. Motion blurring of lesions (liver, arrows) was significantly reduced by gating and motion correction, leading to smaller volumes and higher apparent uptake. Whereas the reduced number of counts is obvious in (B), noise patterns in (A), (C) and (D) are consistent.

motion-corrected images were virtually indistinguishable. Complete quantitative results on motion correction can be found in Table Table 6.4.

Background

Static images exhibited a noise level of (14.7 ± 2.5)% on average. Depending on the respiratory-signal source, this level could be maintained at between (14.3 ± 2.4)% and (14.5 ± 2.6)% (moco_mr) and at between (14.8 ± 2.3)% and (15.0 ± 2.4)% (moco_pet) in motion-corrected images, but was between (29.2 ± 4.2)% and (29.9 ± 4.5)% in the gated images.

Tracer Uptake in Lesions

For resp_bestpet, neither of the observed differences in tracer uptake between gated and moco_mr (maximum uptake, $p = 0.140$; mean uptake, $p = 0.274$), between gated and moco_pet (maximum uptake, $p = 0.990$; mean uptake, $p = 0.572$) or between moco_mr and moco_pet images (maximum uptake, $p = 0.116$; mean uptake, $p = 0.153$) were significant.

Lesion Volumes

The differences in lesion volumes, with resp_bestpet as gating method, were not significant for gated and moco_mr ($p = 0.058$) and gated and moco_pet ($p = 0.909$) images. For moco_mr and moco_pet, a p-value of $p = 0.029$ was calculated.

Lesion Contrast and SNR

The differences between moco_mr and moco_pet in terms of contrast and SNR were not significant ($p \geq 0.167$) with resp_bestpet as gating method, whereas the application of any motion correction improved both figures significantly over gating ($p \leq 0.028$).

	resp_bellows	resp_mr	resp_sens	resp_bestpet
Lesions				
Max. activity concentration				
Static (kBq/mL)		18.6 ± 11.9		
Gate 1 (% static)	119.9 ± 16.8	119.3 ± 15.5	114.7 ± 15.0	116.4 ± 18.3
moco_mr (% static)	109.2 ± 9.4	112.2 ± 10.2	104.1 ± 5.9	111.1 ± 8.3
moco_pet (% static)	110.4 ± 15.6	114.1 ± 16.8	110.7 ± 15.6	116.8 ± 16.5
Mean activity concentration				
Static (kBq/mL)		12.5 ± 8.0		
Gate 1 (% static)	120.5 ± 17.8	119.6 ± 15.5	115.5 ± 17.0	116.5 ± 19.0
moco_mr (% static)	110.5 ± 10.3	113.6 ± 11.9	104.7 ± 6.3	112.7 ± 9.8
moco_pet (% static)	110.3 ± 15.6	115.3 ± 14.7	111.2 ± 13.7	117.7 ± 15.4
Volume				
Static (10^3 mm^3)		4.0 ± 6.5		
Gate 1 (% static)	69.5 ± 25.9	70.3 ± 25.1	74.1 ± 23.1	75.8 ± 30.6
moco_mr (% static)	83.7 ± 18.4	82.2 ± 18.5	91.7 ± 16.4	82.7 ± 18.4
moco_pet (% static)	84.7 ± 21.1	77.3 ± 19.5	82.6 ± 20.1	74.0 ± 21.7
Contrast				
Static (%)		47.3 ± 31.2		
Gate 1 (% static)	108.0 ± 92.2	97.6 ± 100.5	109.1 ± 53.6	113.3 ± 59.4
moco_mr (% static)	106.4 ± 43.7	107.5 ± 51.6	116.3 ± 52.6	110.2 ± 42.7
moco_pet (% static)	112.1 ± 31.9	112.1 ± 18.9	104.0 ± 9.2	114.8 ± 25.0
SNR				
Static (%)		1,300 ± 1,396		
Gate 1 (% static)	65.9 ± 61.7	60.3 ± 66.4	65.7 ± 41.0	71.3 ± 40.8
moco_mr (% static)	119.3 ± 60.8	125.6 ± 73.8	120.9 ± 52.3	126.7 ± 62.6
moco_pet (% static)	119.6 ± 35.2	125.9 ± 30.6	114.3 ± 21.1	132.8 ± 40.1

Table 6.4.: Summary of results from the analysis of motion correction methods. Image properties are shown for static, gated and motion-corrected images. Results based on resp_pca443sens are not shown due to the similarly high quality of resp_pca443sens and resp_bestpet regarding the included patients.

6.4. Discussion

The goal of this study was the assessment of different MR- and PET-data-driven respiratory gating and motion correction methods.

With regard to respiratory signals, the quality of resp_bellows was artificially reduced by the limited signal range supported in the current implementation on the PET/MR scanner and the resulting signal cut-off. Although this factor should not affect amplitude-based gated in most cases, the true correlation of resp_mr and resp_bellows is expected to be higher than the 0.63 ± 0.19 in this study.

The comparably low average correlation of 0.52 ± 0.26 of resp_sens with resp_mr as reference, combined with a higher standard deviation across the patient population reveals its lower reliability. Büther et al. [10] reported a correlation of 0.65 between their implementation of resp_sens and respiratory signals obtained with a video-based method. Whereas the injected activity doses were similar, patients included in the present study had more than 30% lower activity levels at the start of the scan because the average delay was 135 minutes instead of 60 minutes, which might explain the difference in correlation. Moreover, Büther et al. restricted their study to cardiac scans, for which an extended hot object, that is, the heart, is centred in the FOV, which could be an additional advantage for resp_sens. Support for this can be found in a publication by Thielemans et al. [95], who observed a correlation of approximately 0.50 between resp_sens and a video-based method, if one third of the acquired counts was deliberately rejected for the simulation of lower doses.

Of the more complex PET methods evaluated in this paper, resp_pca yielded better results than resp_le. The hypothesis could be confirmed that preservation of the sensitivity profile followed by the application of PCA or LE as proposed above increased quality and robustness of PET-driven respiratory signal extraction, especially towards lower activities in the patient's body or with less specific tracer uptake. In general, the higher the quality of resp_le or resp_pca was, the lower was the benefit of resp_le+sens or resp_pca+sens. However, integration of the sensitivity method facilitated higher levels of compression without sacrificing the resulting signal quality, which means that information lost because of compression could be compensated for. This leads to the possibility of extracting respiratory signals from PET list-mode data under more difficult conditions, for example, lower injected doses, and reduction of processing time or required computing power.

As shown with resp_bestpet, the signal quality could be increased with patient-specific compression parameters. This observation hints at a sensitivity of data-driven respiratory signal extraction to a combination of breathing patterns, activity levels and tracer distributions, which are very individual. Hence, there is no single level of sinogram compression that yields the best result for every patient examination. The comparably low minimum correlation

coefficient of 0.4 of resp_bestpet to resp_mr could be treated as an outlier. If this data point is excluded, the lowest correlation will be 0.67. Furthermore, 75% of resp_bestpet signals provide correlation coefficients higher than 0.70 and, in 30% of the cases, they are even higher than 0.90. Consequently, resp_bestpet was confirmed to be a feasible approach, if both MR and PET data are available for a common period of time.

The correlation with the video-based method of approximately 0.8 for both resp_pca and resp_le as reported by Thielemans et al. [94,95] could be achieved only with resp_le+sens and resp_pca+sens in the present study. Possible reasons for this discrepancy include the levels of sinogram compression that were used and the sampling rates of the respiratory signals, the latter of which were 5 times higher in this study. Moreover, because the studies were not performed on the same scanner models, the corresponding results might be subject to different scanners' sensitivities and scatter fractions. The longer scan duration of 10 minutes in the present study, compared with the 3 minutes of Thielemans et al. might also play a role.

Quantitative image analysis confirmed the correlation analysis. The only significant differences in lesion displacement were between resp_bellows and resp_pca443sens and between resp_sens and the other gating methods under investigation, and the only significant differences in lesion volume were between resp_bellows and resp_pca443sens or resp_bestpet. These findings support the notion that resp_bellows and resp_sens produce slightly inferior respiratory signals.

The results of motion correction had to be validated with both static and gated images. Gated images represent the reference for tracer uptake quantification and lesion volume. This should be achieved with motion correction, albeit at the noise levels of static images. As expected, both motion correction methods fully recovered the static noise level, whereas the noise exhibited by gated images was significantly higher, reducing SNR and hence lesion detectability.

The inferiority of motion correction driven by PET to that driven by MR could not be confirmed in this study. On the contrary, the only statistically significant difference between the two motion correction methods for any of the analysed image properties was found in lesion volumes, if sinograms were created using resp_bestpet. Moreover, moco_pet appears to perform marginally better than moco_mr in terms of tumour uptake and volume. This could be due to two reasons. First, the application of MR-derived motion fields to PET data constitutes an indirect approach, whereas optical flow allows the direct calculation of motion information from PET data. The result of the latter would be a better agreement of the motion-corrected images and the images of the reference gate. Subsequently, the quality of the motion-corrected image would increase with the image quality of the gated reference. Second, MR motion fields were created by image warping using trilinear interpolation. Otherwise, it would be difficult to connect information from multiple modalit-

ies. However, mass-preserved optical flow, which forms the basis of moco_pet, is superior to optical flow employing linear interpolation as shown by Dawood et al. [19].

As supposed, SNR increased significantly over gating after the application of either motion correction method. The case was similar for lesion contrast, for which only that in moco_pet images combined with resp_pca443sens did not change significantly. In general, these results highlight the consistency of both MR- and PET-driven motion correction methods.

Because of the limited number of real patient cases included in published studies, comparison is difficult. Würslin et al. evaluated an MR-based motion correction of reconstructed PET images with data of 5 patients [105]. Similar to the findings in this study, they observed increases of 28%, 25% and 27% in motion-corrected relative to static images for maximum activity concentration in lesions, contrast and SNR, respectively. They defined contrast as the ratio of maximum activity concentration in a lesion – instead of mean activity concentration here – over mean activity concentration in background tissue. Because of the corresponding behaviour of mean and maximum tracer uptake in the present study, this difference should not play an important role, however. When comparing motion-corrected and gated images, Würslin et al. found only SNR to improve significantly, whereas maximum tracer uptake, volume and contrast were significantly worse. This finding contrasts with the observation presented in this study and might hint at the advantages of motion correction incorporated into the reconstruction algorithm, where in the present study for both evaluated methods contrast and SNR were measured to be significantly better than in gated images, but tracer uptake and volume were not significantly different (resp_bestpet). Petibon et al. [72] reconstructed motion-corrected images of one liver case using MR-derived motion information. They reported comparable results, that is, an increase in target-to-background ratio, which was defined identically to contrast as used by Würslin et al., of between 22% and 45%, whereas apparent lesion volumes decreased by between 13% and 29%, depending on the lesion, if compared to static images. The results for PET-driven motion correction as published by Dawood et al. [19] relate to myocardial thickness and blood-pool activity in the LV in cardiac cases only and are therefore not comparable.

The consistency of MR- and PET-based motion correction methods as established in this study offers the operator of a PET/MR system a range of strategy choices tailored to a specific application. In oncological ^{18}F-FDG studies, there will be the highest flexibility with regard to motion correction and scan protocols as the user can fully rely on PET-driven gating and correction methods. In more specialised cases with lower applied activities or less common radiotracers, moco_pet might have its limitations. For such purposes, motion models could be acquired with, for example, radial MR sequences. During this span of a few minutes, MR- and PET-derived respiratory signals could be compared, and depending on the correlation, it could

be decided, if PET respiratory signal quality is sufficient. If not, the system could automatically fall back to resp_mr or resp_bellows or a different external sensor. If in another scenario the user is not concerned with scan time, because the planned MR protocol is not demanding or because the clinician would be satisfied with the anatomical quality of the MR images acquired with the self-gating pulse sequence for motion modelling, moco_mr could be utilised in combination with resp_mr.

In future work, the limitations of PET-driven gating and moco_pet with regard to count rate statistics should be thoroughly investigated. Moreover, the comparison of moco_mr and moco_pet should be extended to other more specialised applications, such as cardiac PET imaging. In addition, it would be desirable to develop an algorithm to automatically select the optimal combination of radial bins and projections for resp_pca, as well as subsequent quality assessment without additional MR information.

6.5. Conclusions

Respiratory traces extracted from PET data are comparable to MR-derived signals and those based on external sensors. With the proposed PET-driven gating method, a higher quality of respiratory traces was achieved and the overall stability improved. Improvements in image quality, tracer uptake quantification and lesion volume delineation achieved with MR- and PET-based respiratory motion correction methods were consistent in evaluated oncological standard examinations, allowing for more flexible PET/MR scan protocols that use solely PET-driven monitoring and correction. In lower-dose regimes, the results of motion correction could be enhanced by the addition of external sensors or motion models derived from MR sequences.

Part V.

Conclusions

This work represents a thorough and in-depth investigation of integrated whole-body PET/MR. For the first time, this novel technology was evaluated not only with regard to hardware, but also with respect to the consequences of this integration for either modality, focusing on aspects of PET quantification. In this context, two different methods for the improvement of PET images could finally be implemented and compared in a clinical setting.

The goals of this work were to evaluate the performance of a novel integrated whole-body PET/MR scanner, to assess both with and without contrast agent the MR-based attenuation maps used for PET attenuation correction on this system and consequences for cardiac PET imaging, to measure the effect of flexible radiofrequency coils and other additional hardware on PET quantification and scan duration and to investigate motion-correction strategies for PET/MR.

As presented in chapter 3, the results of the performance tests compare very well with current PET/CT scanners, indicating the successful integration of PET and MRI for whole-body imaging.

The segmentation-based method for attenuation-map generation utilising the Dixon sequence was found to reproducible and stable in the absence of contrast agents (chapter 4). The application of contrast agent, however, leads to a significant over-weighting of soft tissue in attenuation maps, leading to substantial artefacts in attenuation-corrected PET images, which could affect reading and diagnoses. The author therefore argues for the adjustment of imaging protocols and segmentation of attenuation maps that is optimised for contrast agents.

It was shown in chapter 5 that scan durations on the Biograph mMR would have to be increased compared to current PET/CTs due to the additional attenuation caused by coils and especially the patient table. Otherwise image noise was increased. Moreover, considerable quantitative inaccuracies were caused by the application of surface coils without including them in the process of attenuation correction, affecting comparability across PET/MR and PET/CT scanners and within patient populations. This means that any type of material in the field of view of a PET scanner should be accounted for in attenuation correction.

The methods for the extraction of respiratory signals from PET and MR data under investigation in chapter 6 were consistent. The proposed PET-driven gating method could achieve a higher quality of respiratory traces and improve the overall stability, especially at lower levels of activity. This and the comparability of PET- and MR-based respiratory motion correction methods allow for more flexible PET/MR scan protocols that employ solely PET-driven monitoring and correction. In lower-dose regimes, motion correction could benefit from the addition of external sensors or motion models derived from MR sequences.

The conclusion with this dissertation of the above research projects does not mark an end, but should rather be considered as a starting point. The aca-

demic findings presented in the previous chapters have to be translated into specific measures for the advancement of clinical PET/MR systems. For this purpose, manufacturers of such systems have to take special care to make the integration into the clinical routine seamless, without sacrificing patient comfort, throughput or system stability. At the same time, complexity of patient preparation, scan protocols and system operation should not be increased.

List of Publications

Peer-reviewed Journal Articles

1. Klutz K, Willhauck MJ, Dohmen C, Wunderlich N, Knoop K, Zach C, Senekowitsch-Schmidtke R, Gildehaus FJ, Ziegler SI, **Fürst S**, Göke B, Wagner E, Ogris M, Spitzweg C. Image-guided tumor-selective radioiodine therapy of liver cancer after systemic nonviral delivery of the sodium iodide symporter gene.
Human Gene Therapy. 2011;22:1563–1574.

2. Delso* G, **Fürst* S**, Jakoby BW, Ladebeck R, Ganter C, Nekolla SG, Schwaiger M, Ziegler SI. Performance measurements of the Siemens mMR integrated whole-body PET/MR scanner.
J Nucl Med. 2011;52:1914–1922.

3. Drzezga A, Souvatzoglou M, Eiber M, Beer AJ, **Fürst S**, Martinez-Möller A, Nekolla SG, Ziegler SI, Ganter C, Rummeny EJ, Schwaiger M. First clinical experience with integrated whole-body PET/MR: comparison to PET/CT in patients with oncologic diagnoses.
J Nucl Med. 2012;53:845–855.

4. **Fürst S**, Pulko J, Hohberg M, Mann AB, Ziegler SI. Effects of temperature and bias voltage on the properties of a PET detector module based on the individual readout of 1×1 mm^2 LYSO crystals by monolithic arrays of SiPMs.
JINST. 2012;7:P08002.

5. Gaertner FC, **Fürst S**, Schwaiger M. PET/MR: a paradigm shift.
Cancer Imaging. 2013;13:36–52.

6. Gaertner FC, Beer AJ, Souvatzoglou M, Eiber M, **Fürst S**, Ziegler SI, Brohl F, Schwaiger M, Scheidhauer K. Evaluation of feasibility and image quality of 68Ga-DOTATOC PET/MR in comparison with PET/CT in patients with neuroendocrine tumors.
Invest Radiol. 2013;48:263–272.

7. Souvatzoglou M, Eiber M, Martinez-Moeller A, **Fürst S**, Holzapfel K, Maurer T, Ziegler SI, Nekolla SG, Schwaiger M, Beer AJ. PET/MR in prostate cancer: technical aspects and potential diagnostic value.
Eur J Nucl Med Mol Imag. 2013;40:79–88.

8. Souvatzoglou M, Eiber M, Takei T, **Fürst S**, Maurer T, Gaertner F, Geinitz H, Drzezga A, Ziegler SI, Nekolla SG, Rummeny EJ, Schwaiger M, Beer AJ. Comparison of integrated whole-body 11Ccholine PET/MR with PET/CT in patients with prostate cancer.
Eur J Nucl Med Mol Imag. 2013;40:1486–1499.

9. **Fürst S**, Souvatzoglou M, Martinez-Möller A, Schwaiger M, Nekolla* SG, Ziegler* SI. Impact of flexible body surface coil and patient table on PET quantification and image quality in integrated PET/MR.
Nuklearmedizin Nuclear medicine. 2014;53:79–87.

10. Eiber* M, Takei* T, Souvatzoglou M, Mayerhoefer ME, **Fürst S**, Gaertner FC, Loeffelbein DJ, Rummeny EJ, Ziegler SI, Schwaiger M, Beer AJ. Performance of whole-body integrated 18F-FDG PET/MR in comparison to PET/CT for evaluation of malignant bone lesions.
J Nucl Med. 2014;55:191–197.

11. Rauscher* I, Eiber* M, **Fürst S**, Souvatzoglou M, Nekolla SG, Ziegler SI, Rummeny EJ, Schwaiger M, Beer AJ. PET/MR imaging in the detection and characterization of pulmonary lesions: technical and diagnostic evaluation in comparison to PET/CT.
J Nucl Med. 2014;55:724–729.

12. Hitz* S, Habekost* C, **Fürst S**, Delso G, Förster S, Ziegler SI, Nekolla SG, Souvatzoglou M, Beer AJ, Grimmer T, Eiber M, Schwaiger M, Drzezga A. Systematic comparison of the performance of integrated whole-body PET/MR imaging to conventional PET/CT for 18F-FDG brain imaging in patients examined for suspected dementia.
J Nucl Med. 2014;55:923–931.

13. Koivumaki T, Nekolla SG, **Fürst S**, Loher S, Vauhkonen M, Schwaiger M, Hakulinen MA. An integrated bioimpedance-ECG gating technique for respiratory and cardiac motion compensation in cardiac PET.
Phys Med Biol. 2014;59:6373–6385.

14. Izquierdo-Garcia D, Hansen AE, Förster S, Benoit D, Schachoff S, **Fürst S**, Chen KT, Chonde DB, Catana C. An SPM8-based approach for attenuation correction combining segmentation and nonrigid template formation: application to simultaneous PET/MR brain imaging.
J Nucl Med. 2014;55:1825–1830.

15. Grimm R, **Fürst S**, Souvatzoglou M, Forman C, Hutter J, Dregely I, Ziegler SI, Kiefer B, Hornegger J, Block KT, Nekolla SG. Self-gated MRI motion modeling for respiratory motion compensation in integrated PET/MRI.
Med Image Anal. 2015;19:110–120.

16. **Fürst S**, Grimm R, Hong I, Souvatzoglou M, Casey ME, Schwaiger M, Nekolla* SG, Ziegler* SI. Motion correction strategies for integrated PET/MR.
J Nucl Med. 2015;56:261–269.

*Both authors contributed equally.

Conference Proceedings

1. **Fürst S**, Delso G, Martinez-Möller A, Jakoby BW, Schoenahl F, Ganter C, Nekolla SG, Ziegler SI, Rummeny E, Schwaiger M. Initial performance evaluation of the Biograph mMR.
SNM Annual Meeting 2011.

2. **Fürst S**, Delso G, Jakoby BW, Ganter C, Nekolla SG, Schwaiger M, Ziegler SI. Comparative performance study of the Biograph mMR.
RSNA Annual Meeting 2011.

3. **Fürst S**, Souvatzoglou M, Martinez-Möller A, Nekolla S, Schwaiger M, Ziegler S. Impact of MRI surface coils on quantification in integrated PET/MR.
SNM Annual Meeting 2012.

4. **Fürst S**, Souvatzoglou M, Rischpler C, Ziegler SI, Schwaiger M, Nekolla SG. Effects of MR contrast agents on attenuation map generation and cardiac PET quantification in PET/MR.
ICNC 11, 2013.

5. **Fürst S**, Kruschke C, Ziegler SI, Nekolla SG. Effect of solid PET/CT and PET/MR hardware on clinical performance.
SNM Annual Meeting 2013.

6. **Fürst S**, Grimm R, Hong I, Souvatzoglou M, Casey M, Schwaiger M, Ziegler SI, Nekolla SG. MR- and PET-driven motion correction for integrated PET/MR abdominal/thoracic imaging.
SNM Annual Meeting 2014.

List of Abbreviations

1d/2d/3d	one-/two-/three-dimensional
AC	attenuation correction
ACR	American College of Radiology
APD	avalanche photodiode
CA	contrast agent
COM	centre of mass
CT	computed tomography
^{18}F-FDG	^{18}F-fluorodeoxyglucose
FBP	filtered backprojection
FOV	field of view
FWHM	full width at half maximum
FWTM	full width at tenth maximum
Gd	gadolinium
GRE	gradient echo
LE	Laplacian Eigenmaps
LOR	line of response
LSO	lutetium oxyorthosilicate
LV	left ventricle
MR(I)	magnetic resonance (imaging)
μ-map	attenuation map
NEC rate	noise-equivalent count rate
NEMA	National Electrical Manufacturers Association
OSEM	ordered-subset expectation maximisation
PCA	principal component analysis
PET	positron emission tomography
p. i.	post injection
PMT	photomultiplier tube
RF	radiofrequency
SNR	signal-to-noise ratio
SSRB	single-slice rebinning
SUV	standardised uptake value
$\mathbf{SUV_{mean}}$	mean SUV
$\mathbf{SUV_{max}}$	maximum SUV
$\mathbf{TE}_i$	echo time, time of the i*th* echo
TR	repetition time
VIBE	volumetric interpolated breath-hold examination

VOI volume of interest

List of Figures

List of Tables

Bibliography

[1] American College of Radiology (ACR). *Magnetic Resonance Imaging Quality Control Manual*. ACR, Reston, VA, 2004.

[2] G. Antoch, L. S. Freudenberg, T. Egelhof, J. Stattaus, W. Jentzen, J. F. Debatin, and A. Bockisch. Focal tracer uptake: a potential artifact in contrast-enhanced dual-modality PET/CT scans. *J Nucl Med*, 43(10):1339–1342, 2002.

[3] D. L. Bailey. Data acquisition and performance characterization in PET. In D. L. Bailey, D. W. Townsend, P. E. Valk, and M. N. Maisey, editors, *Positron Emission Tomography*, pages 41–62. Springer-Verlag London Limited, 2005.

[4] D. L. Bailey, J. S. Karp, and S. Surti. Physics and instrumentation in PET. In D. L. Bailey, D. W. Townsend, P. E. Valk, and M. N. Maisey, editors, *Positron Emission Tomography - Basic Science*, pages 13–40. Springer-Verlag London Limited, 2005.

[5] M.-F. Bellin. MR contrast agents, the old and the new. *Eur J Radiol*, 60(3):314–323, 2006.

[6] T. Beyer, D. W. Townsend, T. Brun, P. E. Kinahan, M. Charron, R. Roddy, J. Jerin, J. Young, L. Byars, and R. Nutt. A combined PET/CT scanner for clinical oncology. *J Nucl Med*, 41(8):1369–1379, 2000.

[7] R. A. Bundschuh, A. Martínez-Möller, M. Essler, M.-J. Martínez, S. G. Nekolla, S. I. Ziegler, and M. Schwaiger. Postacquisition detection of tumor motion in the lung and upper abdomen using list-mode PET data: a feasibility study. *J Nucl Med*, 48(5):758–763, 2007.

[8] R. A. Bundschuh, A. Martínez-Möller, M. Essler, S. G. Nekolla, S. I. Ziegler, and M. Schwaiger. Local motion correction for lung tumours in PET/CT—first results. *Eur J Nucl Med Mol Imag*, 35(11):1981–1988, 2008.

[9] I. A. Burger, D. M. Huser, C. Burger, G. K. von Schulthess, and A. Buck. Repeatability of FDG quantification in tumor imaging: averaged SUVs are superior to SUVmax. *Nucl Med Biol*, 39(5):666–670, 2012.

[10] F. Buther, M. Dawood, L. Stegger, F. Wubbeling, M. Schafers, O. Schober, and K. P. Schafers. List mode-driven cardiac and respiratory gating in PET. *J Nucl Med*, 50(5):674–681, 2009.

[11] R. E. Carson, M. E. Daube-Witherspoon, and M. V. Green. A method for postinjection PET transmission measurements with a rotating source. *J Nucl Med*, 29(9):1558–1567, 1988.

[12] C. Catana, Y. Wu, M. S. Judenhofer, J. Qi, B. J. Pichler, and S. R. Cherry. Simultaneous acquisition of multislice PET and MR images: Initial results with a MR-compatible PET scanner. *J Nucl Med*, 47(12):1968–1976, 2006.

[13] M. D. Cerqueira, N. J. Weissman, V. Dilsizian, A. K. Jacobs, S. Kaul, W. K. Laskey, D. J. Pennell, J. A. Rumberger, T. Ryan, and M. S. Verani. Standardized myocardial segmentation and nomenclature for tomographic imaging of the heart. *Circulation*, 105(4):539–542, 2002.

[14] H. Chandarana, T. K. Block, A. B. Rosenkrantz, R. P. Lim, D. Kim, D. J. Mossa, J. S. Babb, B. Kiefer, and V. S. Lee. Free-breathing radial 3D fat-suppressed T1-weighted gradient echo sequence. *Invest Radiol*, 46(10):648–653, 2011.

[15] S. R. Cherry, J. A. Sorensen, and M. E. Phelps. Tomographic Reconstruction in Nuclear Medicine. In *Physics in Nuclear Medicine*, pages 253–277. Elsevier, 4th edition, 2012.

[16] S. Y. Chun, T. G. Reese, J. Ouyang, B. Guérin, C. Catana, X. Zhu, N. M. Alpert, and G. El Fakhri. MRI-based nonrigid motion correction in simultaneous PET/MRI. *J Nucl Med*, 53(8):1284–1291, 2012.

[17] B. D. Coombs, J. Szumowski, and W. Coshow. Two-point Dixon technique for water-fat signal decomposition with B_0 inhomogeneity correction. *Magn Reson Med*, 38(6):884–889, 1997.

[18] M. Dawood, F. Buther, N. Lang, O. Schober, and K. P. Schäfers. Respiratory gating in positron emission tomography: a quantitative comparison of different gating schemes. *Med Phys*, 34(7):3067–3076, 2007.

[19] M. Dawood, F. Gigengack, X. Jiang, and K. P. Schäfers. A mass conservation-based optical flow method for cardiac motion correction in 3D-PET. *Med Phys*, 40(1):012505, 2013.

[20] G. Delso, A. Martínez-Möller, R. A. Bundschuh, R. Ladebeck, Y. Candidus, D. Faul, and S. I. Ziegler. Evaluation of the attenuation properties of MR equipment for its use in a whole-body PET/MR scanner. *Phys Med Biol*, 55(15):4361–4374, 2010.

[21] N. Dikaios and T. D. Fryer. Registration-weighted motion correction for PET. *Med Phys*, 39(3):1253–1264, 2012.

[22] N. Dikaios, D. Izquierdo-Garcia, M. J. Graves, V. Mani, Z. A. Fayad, and T. D. Fryer. MRI-based motion correction of thoracic PET: initial comparison of acquisition protocols and correction strategies suitable for simultaneous PET/MRI systems. *Eur Radiol*, 22(2):439–446, 2011.

[23] W. T. Dixon. Simple proton spectroscopic imaging. *Radiology*, 153(1):189–194, 1984.

[24] A. Drzezga, M. Souvatzoglou, M. Eiber, A. J. Beer, S. Fürst, A. Martínez-Möller, S. G. Nekolla, S. I. Ziegler, C. Ganter, E. J. Rummeny, and M. Schwaiger. First clinical experience with integrated whole-body PET/MR: comparison to PET/CT in patients with oncologic diagnoses. *J Nucl Med*, 53(6):845–855, 2012.

[25] C. Eberhardt and A. Horvath. Photomultiplier Tube. `http://commons.wikimedia.org/wiki/File:Photomultipliertube.svg`. Visited on January 25th 2015.

[26] R. L. Ehman and J. P. Felmlee. Adaptive technique for high-definition MR imaging of moving structures. *Radiology*, 173(1):255–263, 1989.

[27] M. J. Firbank, A. Coulthard, R. M. Harrison, and E. D. Williams. A comparison of two methods for measuring the signal to noise ratio on MR images. *Phys Med Biol*, 44(12):N261–N264, 1999.

[28] R. R. Fulton, S. R. Meikle, S. Eberl, J. Pfeiffer, C. J. Constable, and M. J. Fulham. Correction for head movements in positron emission tomography using an optical motion-tracking system. *IEEE Trans Nucl Sci*, 49(1):116–123, 2002.

[29] S. Fürst. Development and Evaluation of Novel Detectors for Combined PET/MR Imaging, Based on SiPMs and Fast Scintillation Crystals. Master's thesis, Technische Universität München, 2009.

[30] B. M. Gallagher, A. Ansari, H. Atkins, V. Casella, D. R. Christman, J. S. Fowler, T. Ido, R. R. MacGregor, P. Som, C. N. Wan, A. P. Wolf, D. E. Kuhl, and M. Reivich. Radiopharmaceuticals XXVII. 18F-labeled 2-deoxy-2-fluoro-d-glucose as a radiopharmaceutical for measuring regional myocardial glucose metabolism in vivo: tissue distribution and imaging studies in animals. *J Nucl Med*, 18(10):990–996, 1997.

[31] C. Ganter. Analytical solution to the transient phase of steady-state free precession sequences. *Magn Reson Med*, 62(1):149–164, 2009.

[32] C. Ganter, M. Settles, K. Scheffler, and O. Bieri. B1-mapping with the transient phase of SSFP. In *Proceedings of the Annual Meeting of the ISMRM*, page 19, 2011.

[33] K. M. Gilbert, T. J. Scholl, W. B. Handler, J. K. Alford, and B. A. Chronik. Evaluation of a positron emission tomography (PET)-compatible field-cycled MRI (FCMRI) scanner. *Magn Reson Med*, 62(4):1017–1025, 2009.

[34] R. Grimm, S. Fürst, M. Souvatzoglou, C. Forman, J. Hutter, I. Dregely, S. I. Ziegler, B. Kiefer, J. Hornegger, K. T. Block, and S. G. Nekolla. Self-gated MRI motion modeling for respiratory motion compensation in integrated PET/MRI. *Med Image Anal*, 19(1):110–120, 2015.

[35] B. Guérin, S. Cho, S. Y. Chun, X. Zhu, N. M. Alpert, G. El Fakhri, T. Reese, and C. Catana. Nonrigid PET motion compensation in the lower abdomen using simultaneous tagged-MRI and PET imaging. *Med Phys*, 38(6):3025–3038, 2011.

[36] J. He, G. J. O'Keefe, S. J. Gong, G. Jones, T. Saunder, A. M. Scott, and M. Geso. A novel method for respiratory motion gated with geometric sensitivity of the scanner in 3D PET. *IEEE Trans Nucl Sci*, 55(5):2557–2565, 2008.

[37] M. P. Heinrich, M. Jenkinson, S. M. Brady, and J. A. Schnabel. Globally optimal deformable registration on a minimum spanning tree using dense displacement sampling. In N. Ayache, H. Delingette, P. Golland, and K. Mori, editors, *Medical Image Computing and Computer-Assisted Intervention – MICCAI 2012*, pages 115–122. Springer, Berlin, Heidelberg, 2012.

[38] J. Hennig. K-space sampling strategies. *Eur Radiol*, 9(6):1020–1031, 1999.

[39] I. Hong, S. Fürst, J. Jones, and M. E. Casey. The strategy of elastic motion corrections. In *Proc IEEE Nucl Sci Symp Med Imaging Conf.*, 2013.

[40] S.-C. Huang, R. E. Carson, M. E. Phelps, E. J. Hoffman, H. A. Schelbert, and D. E. Kuhl. A boundary method for attenuation correction in positron computed tomography. *J Nucl Med*, 22(7):627–637, 1981.

[41] B. W. Jakoby, Y. Bercier, M. Conti, M. E. Casey, B. Bendriem, and D. W. Townsend. Physical and clinical performance of the mCT time-of-flight PET/CT scanner. *Phys Med Biol*, 56(8):2375–2389, 2011.

[42] B. W. Jakoby, Y. Bercier, C. C. Watson, B. Bendriem, and D. W. Townsend. Performance characteristics of a new LSO PET/CT scanner with extended axial field-of-view and PSF reconstruction. *IEEE Trans Nucl Sci*, 56(3):633–639, 2009.

[43] R. Kartmann, D. H. Paulus, H. Braun, B. Aklan, S. Ziegler, B. K. Navalpakkam, M. G. Lentschig, and H. H. Quick. Integrated PET/MR imaging: automatic attenuation correction of flexible RF coils. *Med Phys*, 40(8):082301–082301–14, 2013.

[44] V. Keereman, R. V. Holen, P. Mollet, and S. Vandenberghe. The effect of errors in segmented attenuation maps on PET quantification. *Med Phys*, 38(11):6010–6019, 2011.

[45] B. Kemp, J. Williams, R. Ruter, V. Lowe, and B. Mullan. Performance measurements of a whole body PET/CT system with time-of-flight capability. In *Society of Nuclear Medicine Annual Meeting Abstracts*, page 1546, 2009.

[46] P. E. Kinahan and J. S. Karp. Figures of merit for comparing reconstruction algorithms with a volume-imaging PET scanner. *Phys Med Biol*, 39(3):631–642, 1994.

[47] P. E. Kinahan, D. W. Townsend, T. Beyer, and D. Sashin. Attenuation correction for a combined 3D PET/CT scanner. *Med Phys*, 25(10):2046–2053, 1998.

[48] C. Klein, S. G. Nekolla, F. M. Bengel, M. Momose, A. Sammer, F. Haas, B. Schnackenburg, W. Delius, H. Mudra, D. Wolfram, and M. Schwaiger. Assessment of myocardial viability with contrast-enhanced Magn Reson Imag. *Circulation*, 105(2):162–167, 2002.

[49] G. F. Knoll. *Radiation Detection and Measurement* . Wiley, 2000.

[50] R. Kumar, V. A. Loving, A. Chauhan, H. Zhuang, S. Mitchell, and A. Alavi. Potential of dual-time-point imaging to improve breast cancer diagnosis with ^{18}F-FDG PET. *J Nucl Med*, 46(11):1819–1824, 2005.

[51] F. Lamare, M. J. L. Carbayo, T. Cresson, G. Kontaxakis, A. Santos, C. C. L. Rest, A. J. Reader, and D. Visvikis. List-mode-based reconstruction for respiratory motion correction in PET using non-rigid body transformations. *Phys Med Biol*, 52(17):5187–5204, 2007.

[52] J. Langner, P. Bühler, U. Just, C. Pötzsch, E. Will, and J. van den Hoff. Optimized list-mode acquisition and data processing procedures for ACS2 based PET systems. *Z Med Phys*, 16(1):75–82, 2006.

[53] P. C. Lauterbur. Image formation by induced local interactions: examples employing nuclear magnetic resonance. *Nature*, 242:190–191, 1973.

[54] X. A. Li, C. Stepaniak, and E. Gore. Technical and dosimetric aspects of respiratory gating using a pressure-sensor motion monitoring system. *Med Phys*, 33(1):145–154, 2006.

[55] C. Lois, I. Bezrukov, H. Schmidt, N. F. Schwenzer, M. K. Werner, J. Kupferschläger, and T. Beyer. Effect of MR contrast agents on quantitative accuracy of PET in combined whole-body PET/MR imaging. *Eur J Nucl Med Mol Imag*, 39(11):1756–1766, 2012.

[56] L. R. MacDonald, S. Kohlmyer, C. Liu, T. K. Lewellen, and P. E. Kinahan. Effects of MR surface coils on PET quantification. *Med Phys*, 38(6):2948–2956, 2011.

[57] P. Mansfield and P. K. Grannell. NMR 'diffraction' in solids? *J Phys C Solid State Phys*, 6(22):L422–L426, 1973.

[58] H. R. Marshall, F. S. Prato, L. Deans, J. Théberge, R. T. Thompson, and R. Z. Stodilka. Variable lung density consideration in attenuation correction of whole-body PET/MRI. *J Nucl Med*, 53(6):977–984, 2012.

[59] M.-J. Martínez, Y. Bercier, M. Schwaiger, and S. I. Ziegler. PET/CT Biograph sensation 16. Performance improvement using faster electronics. *Nuklearmedizin Nuclear medicine*, 45(3):126–133, 2006.

[60] A. Martínez-Möller, M. Eiber, S. G. Nekolla, M. Souvatzoglou, A. Drzezga, S. I. Ziegler, E. J. Rummeny, M. Schwaiger, and A. J. Beer. Workflow and scan protocol considerations for integrated whole-body PET/MRI in oncology. *J Nucl Med*, 53(9):1415–1426, 2012.

[61] A. Martínez-Möller, M. Souvatzoglou, G. Delso, R. A. Bundschuh, C. Chefd'hotel, S. I. Ziegler, N. Navab, M. Schwaiger, and S. G. Nekolla. Tissue classification as a potential approach for attenuation correction in whole-body PET/MRI: evaluation with PET/CT data. *J Nucl Med*, 50(4):520–526, 2009.

[62] A. Matthies, M. Hickeson, A. Cuchiara, and A. Alavi. Dual time point ^{18}F-FDG PET for the evaluation of pulmonary nodules. *J Nucl Med*, 43(7):871–875, 2002.

[63] J. R. McClelland, D. J. Hawkes, T. Schaeffter, and A. P. King. Respiratory motion models: a review. *Med Image Anal*, 17(1):19–42, 2013.

[64] S. R. Meikle and R. D. Badawi. Quantitative techniques in PET. In D. L. Bailey, D. W. Townsend, P. E. Valk, and M. N. Maisey, editors, *Positron Emission Tomography - Basic Science*, pages 93–126. Springer-Verlag London Limited, 2005.

[65] National Electrical Manufacturers Association. *NEMA Standards Publication NU 2-2007 - Performance Measurements of Positron Emission Tomographs*. National Electrical Manufacturers Association, 2007.

[66] S. A. Nehmeh, Y. E. Erdi, C. C. Ling, K. E. Rosenzweig, H. Schoder, S. M. Larson, H. A. Macapinlac, O. D. Squire, and J. L. Humm. Effect of respiratory gating on quantifying PET images of lung cancer. *J Nucl Med*, 43(7):876–881, 2002.

[67] S. G. Nekolla, C. Miethaner, N. Nguyen, S. I. Ziegler, and M. Schwaiger. Reproducibility of polar map generation and assessment of defect severity and extent assessment in myocardial perfusion imaging using positron emission tomography. *Eur J Nucl Med Mol Imag*, 25(9):1313–1321, 1998.

[68] J. Nuyts, P. Dupont, S. Stroobants, R. Benninck, L. Mortelmans, and P. Suetens. Simultaneous maximum a posteriori reconstruction of attenuation and activity distributions from emission sinograms. *IEEE Trans Med Imaging*, 18(5):393–403, 1999.

[69] S.-J. Park, D. Ionascu, J. Killoran, M. Mamede, V. H. Gerbaudo, L. Chin, and R. Berbeco. Evaluation of the combined effects of target size, respiratory motion and background activity on 3D and 4D PET/CT images. *Phys Med Biol*, 53(13):3661–3679, 2008.

[70] D. H. Paulus, H. Braun, B. Aklan, and H. H. Quick. Simultaneous PET/MR imaging: MR-based attenuation correction of local radiofrequency surface coils. *Med Phys*, 39(7):4306–4315, 2012.

[71] Y. Petibon, G. El Fakhri, R. Nezafat, N. Johnson, T. Brady, and J. Ouyang. Towards coronary plaque imaging using simultaneous PET-MR: a simulation study. *Phys Med Biol*, 59(5):1203–1222, 2014.

[72] Y. Petibon, C. Huang, J. Ouyang, T. G. Reese, Q. Li, A. Syrkina, Y.-L. Chen, and G. El Fakhri. Relative role of motion and PSF compensation in whole-body oncologic PET-MR imaging. *Med Phys*, 41(4):042503, 2014.

[73] M. E. Phelps, E. J. Hoffman, N. A. Mullani, and M. M. Ter-Pogossian. Application of annihilation coincidence detection to transaxial reconstruction tomography. *J Nucl Med*, 16(3):210–224, 1975.

[74] Y. Picard and C. J. Thompson. Motion correction of PET images using multiple acquisition frames. *IEEE Trans Med Imaging*, 16(2):137–144, 1997.

[75] B. J. Pichler, E. Lorenz, R. Mirzoyan, W. Pimpl, F. Roder, M. Schwaiger, and S. I. Ziegler. Performance test of a LSO-APD PET module in a 9.4 Tesla magnet. In *Proc IEEE Nucl Sci Symp Med Imaging Conf.*, pages 1237–1239, 1997.

[76] I. Polycarpou, C. Tsoumpas, A. P. King, and P. K. Marsden. Impact of respiratory motion correction and spatial resolution on lesion detection in PET: a simulation study based on real MR dynamic data. *Phys Med Biol*, 59(3):697–713, 2014.

[77] I. Polycarpou, C. Tsoumpas, and P. Marsden. Analysis and comparison of two methods for motion correction in PET imaging. *Med Phys*, 39(10):6474–6483, 2012.

[78] A. Rahmim, J. C. Cheng, K. Dinelle, M. Shilov, W. P. Segars, O. G. Rousset, B. M. W. Tsui, D. F. Wong, and V. Sossi. System matrix modeling of externally tracked motion. In *Proc IEEE Nucl Sci Symp Med Imaging Conf.*, pages 2137–2141. IEEE, 2006.

[79] O. Ratib, M. Becker, J.-P. Vallée, P. Loubeyre, M. Wissmeyer, J.-P. Willi, C. Steiner, O. Rager, V. Garibotto, and M. Viallon. Whole body PET-MRI scanner: First experience in oncology. In *Society of Nuclear Medicine Annual Meeting Abstracts*, page 165, 2010.

[80] R. R. Raylman, B. E. Hammer, and N. L. Christensen. Combined MRI-PET scanner: a Monte Carlo evaluation of the improvements in PET resolution due to the effects of a static homogeneous magnetic field. *IEEE Trans Nucl Sci*, 43(4):2406–2412, 1996.

[81] P. Razifar, J. Axelsson, H. Schneider, B. Langstrom, E. Bengtsson, and M. Bergstrom. Volume-wise application of principal component analysis on masked dynamic PET data in sinogram domain. *IEEE Trans Nucl Sci*, 53(5):2759–2768, 2006.

[82] A. J. Reader, R. Manavaki, S. Zhao, P. J. Julyan, D. L. Hastings, and J. Zweit. Acceleration of list-mode expectation maximisation-maximum likelihood. In *Proc IEEE Nucl Sci Symp Med Imaging Conf.*, pages 15/51–15/56. IEEE, 2000.

[83] C. Riddell, R. E. Carson, J. A. Carrasquillo, S. K. Libutti, D. N. Danforth, M. Whatley, and S. L. Bacharach. Noise reduction in oncology FDG PET images by iterative reconstruction: a quantitative assessment. *J Nucl Med*, 42(9):1316–1323, 2001.

[84] A. F. L. Schinkel, D. Poldermans, A. Elhendy, and J. J. Bax. Assessment of myocardial viability in patients with heart failure. *J Nucl Med*, 48(7):1135–1146, 2007.

[85] V. Schulz, T. Solf, B. Weissler, P. Gebhardt, P. Fischer, M. Ritzert, V. Mlotok, C. Piemonte, N. Zorzi, M. Melchiorri, S. Vandenberghe, V. Keereman, T. Schaeffter, and P. K. Marsden. A preclinical PET/MR insert for a human 3T MR scanner. In *Proc IEEE Nucl Sci Symp Med Imaging Conf.*, pages 2577–2579, 2009.

[86] J. Schwartz, J. L. Humm, M. Gonen, H. Kalaigian, H. Schoder, S. M. Larson, and S. A. Nehmeh. Repeatability of SUV measurements in serial PET. *Med Phys*, 38(5):2629–2638, 2011.

[87] Y. Shao, S. R. Cherry, K. Farahani, R. Slates, R. W. Silverman, K. Meadors, A. Bowery, S. Siegel, P. K. Marsden, and P. B. Garlick. Development of a PET detector system compatible with MRI/NMR systems. *IEEE Trans Nucl Sci*, 44(3):1167–1171, 1997.

[88] N. R. Shaw, R. E. Ansorge, and T. A. Carpenter. Commissioning and testing of split coil MRI system for combined PET-MR. *Proceedings of the Annual Meeting of the ISMRM*, 13:407, 2005.

[89] V. C. Spanoudaki. *Development and Performance Studies of a Small Animal Positron Emission Tomograph with Individual Crystal Readout and Depth of Interaction Information and Studies of Novel Detector Technologies in Medical Imaging.* PhD thesis, Technische Universität München, 2008.

[90] V. C. Spanoudaki, D. P. McElroy, I. Torres-Espallardo, and S. I. Ziegler. Effect of temperature on the performance of proportional APD-based modules for gamma ray detection in positron emission tomography. *IEEE Trans Nucl Sci*, 55(1):469–480, 2008.

[91] S. Surti, A. Kuhn, M. E. Werner, A. E. Perkins, J. Kolthammer, and J. S. Karp. Performance of Philips Gemini TF PET/CT scanner with special consideration for its time-of-flight imaging capabilities. *J Nucl Med*, 48(3):471–480, 2007.

[92] L. Tellmann, H. H. Quick, A. Bockisch, H. Herzog, and T. Beyer. The effect of MR surface coils on PET quantification in whole-body PET/MR: Results from a pseudo-PET/MR phantom study. *Med Phys*, 38(5):2795–2805, 2011.

[93] T. J. Tewson, M. J. Welch, and M. E. Raichle. [18F]-labeled 3-deoxy-3-fluoro-d-glucose: synthesis and preliminary biodistribution data. *J Nucl Med*, 19(12):1339–1345, 1978.

[94] K. Thielemans, S. Rathore, F. Engbrant, and P. Razifar. Device-less gating for PET/CT using PCA. In *Proc IEEE Nucl Sci Symp Med Imaging Conf.*, pages 3904–3910. IEEE, 2011.

[95] K. Thielemans, P. J. Schleyer, P. K. Marsden, R. M. Manjeshwar, S. D. Wollenweber, and A. Ganin. Comparison of different methods for data-driven respiratory gating of PET data. In *Proc IEEE Nucl Sci Symp Med Imaging Conf.*, pages 1–4, 2013.

[96] D. W. Townsend. Multimodality imaging of structure and function. *Phys Med Biol*, 53(4):R1–R39, 2008.

[97] R. Turner. Gradient coil design: a review of methods. *Magn Reson Imag*, 11(7):903–920, 1993.

[98] L. van der Maaten, E. O. Postma, and H. J. van den Herik. Dimensionality reduction: a comparative review. Technical Report TiCC-TR 2009-005, 2009.

[99] R. Wagman, E. Yorke, E. Ford, P. Giraud, G. Mageras, B. Minsky, and K. Rosenzweig. Respiratory gating for liver tumors: use in dose escalation. *Int J Radiat Oncol*, 55(3):659–668, 2003.

[100] R. L. Wahl, H. Jacene, Y. Kasamon, and M. A. Lodge. From RECIST to PERCIST: evolving considerations for PET response criteria in solid tumors. *J Nucl Med*, 50(Suppl 1):122S–150S, 2009.

[101] C. C. Watson. New, faster, image-based scatter correction for 3d PET. *IEEE Trans Nucl Sci*, 47(4):1587–1594, 2000.

[102] W. Weber, S. I. Ziegler, R. Thödtmann, A.-R. Hanauske, and M. Schwaiger. Reproducibility of metabolic measurements in malignant tumors using FDG PET. *J Nucl Med*, 40(11):1771–1777, 1999.

[103] M. N. Wernick and J. N. Aarsvold. *Emission Tomography: The Fundamentals of PET and SPECT*. Elsevier Academic Press, 2004.

[104] D. Wild, H. R. Mäcke, B. Waser, J. C. Reubi, M. Ginj, H. Rasch, J. Müller-Brand, and M. Hofmann. ^{68}Ga-DOTANOC: a first compound for PET imaging with high affinity for somatostatin receptor subtypes 2 and 5. *Eur J Nucl Med Mol Imag*, 32(6):724–724, 2004.

[105] C. Wurslin, H. Schmidt, P. Martirosian, C. Brendle, A. Boss, N. F. Schwenzer, and L. Stegger. Respiratory motion correction in oncologic PET using T1-weighted MR imaging on a simultaneous whole-body PET/MR system. *J Nucl Med*, 54(3):464–471, 2013.

[106] H. Zaidi and A. Alavi. Current trends in PET and combined (PET/CT and PET/MR) systems design. *PET Clin*, 2(2):109–123, 2007.

[107] H. Zaidi, O. Mawlawi, and C. G. Orton. Simultaneous PET/MR will replace PET/CT as the molecular multimodality imaging platform of choice. *Med Phys*, 34(5):1525, 2007.

[108] H. Zaidi, N. Ojha, M. Morich, J. Griesmer, Z. Hu, P. Maniawski, O. Ratib, D. Izquierdo-Garcia, Z. A. Fayad, and L. Shao. Design and performance evaluation of a whole-body Ingenuity TF PET–MRI system. *Phys Med Biol*, 56(10):3091–3106, 2011.

[109] B. Zhang, D. Pal, Z. Hu, N. Ojha, T. Guo, G. Muswick, C.-h. Tung, and J. Kaste. Attenuation correction for MR table and coils for a sequential PET/MR system. In *Proc IEEE Nucl Sci Symp Med Imaging Conf.*, pages 3303–3306, 2009.

Acknowledgements

I would like to thank Prof. Sibylle Ziegler for extending her trust beyond my 'Diplomarbeit' and for accepting me as a PhD student in her group. I cannot express how grateful I am for your continuing support of almost 10 years, the professional and personal advice, the excellent discussions and the overall mentoring.

I would also like to thank Dr. Stephan Nekolla for his additional supervision, mentoring and advice and for his support and expertise during my projects. I am very grateful for trusting me and sending me over to Knoxville and, of course, conference excursions to Chicago steak houses.

I am grateful to Prof. Haase for the external supervision and support of this work.

I cordially thank Giaime, Ian, Iina, Isabel, Jorge, Karl, Marie and Rupert for letting me be part of their office team, their friendship, the fun and distractions and cakes for almost any occasion. Moreover, I would like to thank Isabel and Jorge for the discussions, ideas and support for anything MR and image reconstruction.

I would also like to thank Dr. Michael Souvatzoglou for his invaluable medical expertise and overall support with patients, as well as Claudia Meisinger, Sylvia Schachoff and Anna Winter for their assistance regarding patient preparation and examination.

I very much enjoyed the excellent and fruitful collaboration with Robert Grimm, Drs. Matthias Fenchel, Björn Jakoby and Frederic Schoenahl, and appreciate the invaluable support by Jon Treffert for facilitating data processing. I am especially grateful to Inki Hong and Michael Casey for welcoming me and giving me the opportunity to learn and get to know Siemens in Knoxville.

I thank Petra Dorfner, Katharina Lang and Ursula Mühle for the organisation of seminars, research excursion and the warm support on behalf of the Graduate School.

I would also like to thank my parents, Maria and Jürgen, for always believing in me and supporting me in any possible way, and Julia for cheering me on.

The PET/MR system at the centre of this work was funded through the Deutsche Forschungsgemeinschaft (DFG) Grossgeräteinitiative 2010. This research was supported by the Graduate School of Information Science in Health (GSISH) and the TUM Graduate School. It was supported in part by SFB824

and has received funding from the European Union Seventh Framework Program (FP7) under Grant Agreement No. 294582 ERC Grant MUMI.